

Quadrupole Induced Resonant Particle Transport in a Pure Electron Plasma

by

Erik Peter Gilson

B.S. (Massachusetts Institute of Technology) 1993

M.A. (University of California at Berkeley) 1999

A dissertation submitted in partial satisfaction of the
requirements for the degree of
Doctor of Philosophy

in

Physics

in the

GRADUATE DIVISION

of the

UNIVERSITY of CALIFORNIA at BERKELEY

Committee in charge:

Professor Joel Fajans, Chair

Professor Jonathan Wurtele

Professor Allan Lichtenberg

Fall 2001

The dissertation of Erik Peter Gilson is approved:

Chair

Date

Date

Date

University of California at Berkeley

Fall 2001

**Quadrupole Induced Resonant Particle Transport in a Pure
Electron Plasma**

Copyright Fall 2001

by

Erik Peter Gilson

Abstract

Quadrupole Induced Resonant Particle Transport in a Pure Electron Plasma

by

Erik Peter Gilson

Doctor of Philosophy in Physics

University of California at Berkeley

Professor Joel Fajans, Chair

We performed experiments that explore the effects of a quadrupole magnetic field on a pure electron plasma confined in a Malmberg-Penning trap. Our simple model describes the shape of the plasma and shows that a certain class of resonant electrons follows trajectories that take them on large radial excursions, leading to enhanced transport. The quadrupole field destroys the cylindrical symmetry of the system, but our model predicts that if the electrons are not resonant with the quadrupole field, then diffusion will not be greatly enhanced. Our experimental results show that the plasma's shape agrees with our model, but that the diffusion does not. The plasma has the shape of a flux tube if the bulk rotation of the plasma is slower than the axial bounce motion. The plasma is cylindrical if the bulk rotation is faster than the axial bouncing. The measured diffusion scales as the square of the quadrupole field strength as expected. Some predictions of our model prove to be only approximate. The location of the resonance in parameter space scales roughly inversely with the length and proportional to the temperature of the plasma. Further, the temperature we use in fitting the data differs from an independently measured temperature by a factor of four. In addition to being an example of resonant particle transport, this effect is important for experiments that plan to use magnetic quadrupole neutral atom traps to confine antihydrogen created in double-well positron/antiproton Malmberg-Penning traps.

Professor Joel Fajans
Dissertation Committee Chair

To my wife,
Sandy.

Contents

List of Figures	iv
List of Tables	vi
1 Introduction	1
1.1 Antihydrogen	1
1.2 Resonant Particle Transport	2
1.2.1 Nonneutral Plasmas	2
1.2.2 Tandem Mirror Machines	4
1.3 Results	5
1.4 Outline	6
2 Experimental Apparatus	8
2.1 Malmberg-Penning Trap	8
2.2 Diagnostics	14
2.2.1 The Wall	15
2.2.2 The Phosphor	15
2.3 Measuring Plasma Parameters	19
2.3.1 Total Charge	21
2.3.2 Density	24
2.3.3 Length	25
2.3.4 Temperature	25
2.4 Modifications	26
2.4.1 Filament	26
2.4.2 Gates	26
2.4.3 Imaging System	28
2.4.4 Quadrupole Magnets	29
2.5 Automation	34
3 Plasma Shape	37
3.1 Introduction	37
3.1.1 Guiding Center Motion	37
3.1.2 Qualitative Discussion	38
3.1.3 ϵ and θ_p from Images	41

3.1.4	ϵ and θ_p from Wall Sectors	43
3.2	Experiment, Data and Analysis	44
3.2.1	ϵ and θ_p from Images	44
3.2.2	ϵ and θ_p from Wall Sectors	46
3.3	Summary	48
4	Transport	50
4.1	Theory	50
4.1.1	Qualitative Discussion	50
4.1.2	Quantitative Discussion	52
4.2	Experiment	60
4.2.1	Measuring Diffusion	60
4.2.2	Optimal \vec{B}_\perp , β and θ_o	61
4.3	Data and Analysis	63
4.3.1	Diffusion Measurement Example	64
4.3.2	Background Diffusion Processes	67
4.3.3	β Dependence	69
4.3.4	ω and B_z Dependencies	69
4.3.5	L Dependence	71
4.3.6	kT Dependence and Theory Fit	75
4.3.7	r Dependence	77
4.3.8	Dipole Diffusion	77
4.3.9	Flux	77
4.4	Summary	83
5	Conclusions	84
5.1	Summary	84
5.2	The Future	85
A	Imaging System	88
A.1	First Camera System	88
A.2	Second Camera System	88
A.3	Current Camera System	89
B	LabVIEW Programs	96
B.1	Hardware Control	96
B.1.1	AT-AO-6	96
B.1.2	RS-232	97
B.1.3	USB GPIB	97
B.1.4	Image Acquisition	98
B.2	General Experiment Operation	98
B.3	Analysis	99
B.4	Transport Experiment	100
	Bibliography	102

List of Figures

1.1	Bounce resonant electron	3
1.2	Tandem mirror configuration	5
2.1	Schematic drawing of the machine	9
2.2	Inject, hold and dump cycle	10
2.3	Background image	16
2.4	Background subtraction	17
2.5	Numerical solution of phosphor potential	19
2.6	Radial image compression	20
2.7	Voltage divider	21
2.8	Capacitance measurement	22
2.9	Filament distortion	27
2.10	Four-sectored gate schematic	27
2.11	Gate arrangement	28
2.12	Quadrupole field lines	31
2.13	Hexagonal coils	32
2.14	Box coils	33
2.15	Total magnetic field	35
3.1	Slowly rotating plasma	39
3.2	Quickly rotating plasma	39
3.3	Poincaré sections of electrons leaving a circular filament	40
3.4	Typical plasma image with $\beta \neq 0$	41
3.5	Quadrupole signal detection	44
3.6	ϵ and θ_p vs. B_z	45
3.7	Sector tuning circuit	46
3.8	ϵ vs. L	47
3.9	ϵ vs. θ_o	48
3.10	ϵ vs. z	49
4.1	Trajectory of resonant electron	51
4.2	Resonant and nonresonant electrons	54
4.3	D vs. ω	55
4.4	Poincaré sections	58

4.5	Radial trajectory	59
4.6	Q vs. B_x and B_y	62
4.7	B_{\perp} vs. B_z	63
4.8	Typical radial profile	65
4.9	N vs. t	66
4.10	D vs. β_1 and β_2	68
4.11	D vs. β	69
4.12	DB_z^2 vs. ω	70
4.13	Log-log plot of DB_z^2 vs. ω	71
4.14	DB_z^2 vs. ω for several L	72
4.15	ω_{res} vs. L	73
4.16	D_{max} vs. L	74
4.17	DB_z^2 vs. ω for several kT	75
4.18	DB_z^2 vs. ω plus theory curve	76
4.19	DB_z^2 vs. ω for a dipole	78
4.20	Γ vs. ω , $L = 31.0$ cm	79
4.21	Γ vs. ω , $L = 24.8$ cm	80
4.22	Γ vs. ω , $L = 17.1$ cm	81
4.23	Γ vs. ω , $L = 11.9$ cm	82
5.1	Magnetic field diffusion	86
5.2	Possible trap design	87
A.1	Phosphor response	90
A.2	Interface circuit for OMEGA PID controller	92
A.3	CCD camera timing diagram	94

List of Tables

2.1	Typical machine parameters	14
2.2	Magnetic potentials in polar and cartesian coordinates	30
A.1	PP-25 settings	91
A.2	WinView settings	95

Acknowledgements

I think everyone spends some time when they're young imagining what their lives are going to be like when they grow up. I know I did. Even though I thought I'd be a scientist, I never could have guessed all the specifics of my life today. This is not where I thought I'd be, but I'm glad to be here and I've enjoyed the ride. It's time to thank everyone who helped out along the way.

Thanks to Joel for taking me on as a student when he didn't have to. I've learned a great deal from him and I'm grateful. Thanks to Charlie, Anita, and Ramesh for helping me to transition into experimental physics. Thanks to the guys in the Machine Shop and the Electronics Shop for their expertise, advice, and good humor. Thanks to Donna and Anne for always lending an ear and helping me to navigate the big, cold, nameless, faceless, monolithic bureaucracy that is the University of California.

Thanks to Dan and Carl. Their friendship and support means more to me than I think I've ever really expressed to them. Thanks to Steve and Laraine who dragged me out of the lab and into the big city and onto the beautiful Bay. Thanks to Tushar for his constant companionship; I feel as though we went through graduate school together and I value the deep bond we've formed. I've been dazed and confused for so long it's not true. But I feel better now.

Thanks to Nancy for so kindly welcoming me into her family. Thanks to Dan and Deb for their encouragement and for supporting the habit of a Disney/Las Vegas freak.

Thanks to Mom, Dad, and Ethan. What else can you say about your family — they pretty much define who you are — and that's a good thing. Thanks to Ashley for not caring about Calabi-Yau manifolds, antihydrogen, or where I get a job. Thanks for just living in the moment.

And thanks to Sandy. Her love knows no beginning, and it knows no end. It surrounds me and makes me happy. This is not where I thought I'd be, but I'm glad she came along with me.

Chapter 1

Introduction

We have applied an axially invariant, transverse, quadrupole magnetic field to a pure electron plasma confined in a Malmberg-Penning trap in order to study the effect of the quadrupole field on the shape of the plasma and on transport in the plasma. The shape of the plasma follows the surface of a magnetic flux tube if the bulk rotation of the plasma is slow compared to the axial bounce time of the electrons. The plasma is a cylinder when the rotation is fast compared to the bounce time. Measurements of the radial transport show a resonant behavior that is not in complete agreement with our model of the effect, but it is consistent with many of the predicted scalings.

There are two primary motivations for this work: antihydrogen research and resonant particle transport. The work I present in this thesis is relevant to antihydrogen experiments by the ATHENA and ATRAP collaborations at CERN because it helps them to understand whether the quadrupole field will have a deleterious effect on their experiment. This work is also broadly relevant to long timescale confinement issues in nonneutral plasma physics; resonant particle transport is a possible explanation of the finite lifetimes of plasmas in Malmberg-Penning traps at low base pressures.

1.1 Antihydrogen

Antihydrogen experiments at CERN by the ATHENA [1] and ATRAP [2] collaborations may be complicated by the effects of a quadrupole magnetic field on a Malmberg-Penning trap. To create antihydrogen atoms, both collaborations intend to accumulate and cool antiprotons and positrons in Malmberg-Penning traps [3]. The antiprotons come from

the CERN accelerator and the positrons come from radioactive decays. These particles will then be allowed to mix in a recombination region to make antihydrogen. The neutral antihydrogen atoms will not be confined by the Malmberg-Penning trap; magnetic fields with gradients are needed to confine neutral atoms. Neutral atoms with nonzero magnetic moments experience a force in a magnetic field with a gradient, $\vec{F} = (\vec{\mu} \cdot \vec{\nabla})\vec{B}$.

The question addressed in this thesis is whether the quadrupole fields used to confine antihydrogen will ruin the confinement properties of the Malmberg-Penning traps.

If so, then the constituent antiprotons and positrons may not live long enough to reach the recombination stage of the experiment; the experiment will be over before it begins. Both collaborations have trapped antiprotons and positrons, and perhaps at the same time [4], but have not observed recombination.

Important tests of physical theories can be made with antimatter. Antihydrogen atoms have been seen in the PS210 experiment at CERN [5] traveling near the speed of light, making them difficult to study. Energetic antiprotons from the main accelerator pass through a chamber where electrons and positrons are created from the vacuum by pair production. A small number of positrons are captured by the antiprotons to form antihydrogen.

There is great interest in antimatter measurements. If one could trap antihydrogen atoms at rest in the lab, detailed spectroscopic measurements could be made. A comparison of the hydrogen spectrum and the antihydrogen spectrum is an excellent test of the CPT (Charge conjugation, Parity, Time reversal) symmetry of the Standard Model [6, 7]. QED calculations of the hydrogen spectrum are among the most precise calculations in physics and in excellent agreement with observations. In addition to being a test of CPT invariance, antihydrogen could be used to test the WEP (Weak Equivalence Principle) in General Relativity [8]. The WEP is often simply stated as the equivalence of inertial and gravitational mass.

1.2 Resonant Particle Transport

1.2.1 Nonneutral Plasmas

The excellent confinement properties of Malmberg-Penning traps may be understood, via Noether's theorem, as a result of the cylindrical symmetry of the system, which

implies that the canonical angular momentum is conserved. For a strongly magnetized plasma, the canonical angular momentum is proportional to the mean square radius of the plasma [9]. Thus, for a single electron to reach the wall, the other electrons have to move significantly closer to the axis. A trap asymmetry ruins the conservation of canonical angular momentum, allowing radial transport and leading to plasma loss [10]. If an electron is resonant with such an asymmetry, the transport could be greatly enhanced.

The two relevant motions of the electrons' guiding centers for discussing resonant particle transport are the axial bouncing motion and the $\vec{E} \times \vec{B}$ rotation of the plasma about the axis of the trap. The time it takes the electron to travel the length of the trap is t_b and the $\vec{E} \times \vec{B}$ angular rotation frequency is ω_E . If the bounce and rotation motions are commensurate with a spatially localized trap asymmetry that causes radial transport, as in Figure 1.1, then an electron will repeatedly experience this radial transport; the electron

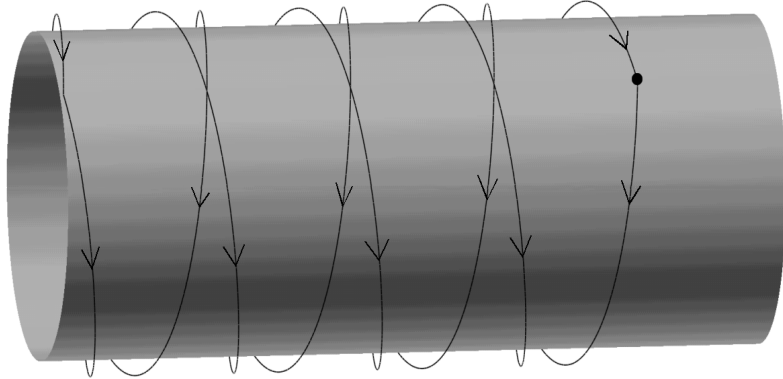


Figure 1.1: This Figure shows a simple illustration of a resonance between a spatially localized perturbation (black dot), ω_E and t_b . $\omega_E t_b$ is such that the electron returns to the perturbation. The effect of the perturbation is enhanced.

is resonant with the perturbation and is quickly lost to the wall of the trap. If the electron is not resonant with the perturbation, then the effect of the perturbation tends to average out and it does not greatly enhance transport.

Resonant particle transport has been suggested as a reason that the plasmas in Malmberg-Penning traps do not last indefinitely. Trap asymmetries certainly have been shown to affect transport [11, 12, 13], but no one has identified a specific mechanism for resonant particle transport that completely agrees with experimental observations.

Much work has been done on the topic of resonant particle transport in Malmberg-Penning traps [14, 15, 16, 17, 18]. Eggleston and O'Neil [18] describe a theory for the effects

of scalar field perturbation, $\phi(\vec{r}, t)$, in a Malmberg-Penning trap. However, the results are not in agreement with observations made by Kriesel and Driscoll [12, 13]. Kriesel and Driscoll's work shows transport caused by the perturbation, but the transport does not scale with the perturbation strength as predicted by Eggleston and O'Neil. Kriesel and Driscoll report transport that scales like $\mathcal{V}(\omega_{Et_b})^2$ for $\pi/10 < \omega_{Et_b} < \pi$, where \mathcal{V} is a measure of the strength of the perturbation. The transport scales like \mathcal{V}^2 , independent of ω_{Et_b} , for $\pi/140 < \omega_{Et_b} < \pi/10$. Eggleston and O'Neil do not predict the \mathcal{V} scaling. Moreover, the data show no direct evidence of resonant particle transport in the sense that there is no evidence that the transport decreases again for $\omega_{Et_b} > \pi$. There is no resonant peak shown in their data. For the $m_\theta = 1$ asymmetry they applied, one naively expects the resonance to be at $\omega_{Et_b} = \pi$.

Experiments by Cluggish, Danielson and Driscoll [19] demonstrate the existence of bounce resonant effects in nonneutral plasmas in the context of plasma heating. The plasma is heated greatly when the heating signal's frequency approaches $2\pi/t_b$ from below. This experiment deals with neither the $\vec{E} \times \vec{B}$ motion of the electrons nor transport, but only axial bounce motion.

1.2.2 Tandem Mirror Machines

Outside of the nonneutral plasma community, the subject of quadrupole field induced transport appears in studies of tandem mirrors machines. Cohen, Ryutov, and Stupakov developed models of transport based on kinetic theory [20, 21, 22, 23]. Chirikov developed a model based on discrete mappings [24]. Figure 1.2 shows the magnet coil and flux tube configuration for a tandem mirror machine. There is a long, central, region where the axial field is uniform. There are mirror fields at the ends. To plug the loss cone, baseball coils on the ends contain high density plasmas that provide electrostatic confinement for the ions in the central region. The central region may be made long enough so that energy needed to maintain the end plasmas is small compared to the expected amount of energy to be generated in the central region.

There are several similarities between the tandem mirror system and our system. Both systems have particles that bounce axially. In the tandem mirror, ions that are outside of the loss cone bounce between the mirror field. Ions that are inside the loss cone bounce between the electrostatic barriers created by the endcap plasmas. In our system, electrons

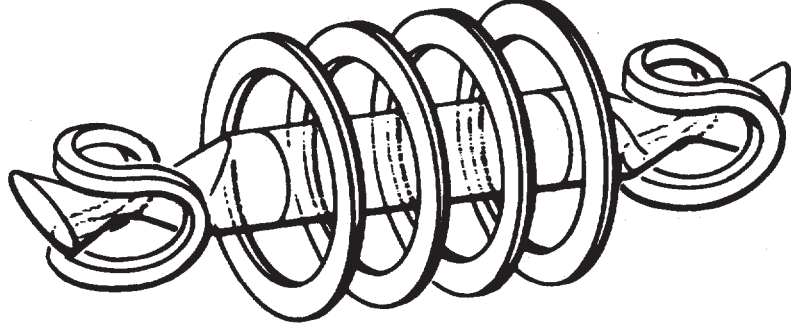


Figure 1.2: In the tandem mirror configuration, two baseball coil magnetic well traps cap the ends of a standard magnetic mirror machine. A high density plasma in the endcaps provides axial confinement for ions in the central mirror.

bounce between the electrostatic potentials of the confinement gates of the trap. Both systems have a bulk azimuthal rotation. In the tandem mirror, ambipolar radial transport creates a radial electric field. In our system, the nonneutral plasma has a radial self electric field.

The tandem mirror system has important differences from ours. Both electrons and ions are present in the tandem mirror machine, while we have only electrons. The quadrupole field exists only at the ends of the tandem mirror machine and the two quadrupole fields that the ions see are rotated by 90° with respect to one another. In our experiment, the quadrupole field is axially invariant, covering the entire machine. In principle then, our system ought to be simpler to study and analyze.

1.3 Results

Our results show that both the shape of the plasma and the transport depend on whether ω_{Et_b} is greater than or less than 1. The shape of the plasma is as we predict. For $\omega_{Et_b} \ll 1$, the electrons follow the magnetic field lines and the plasma has an elliptical shape sometimes called a “twisted bowtie”; the plasma cross section is circular at the axial midpoint, $z = 0$, and is elliptical at the ends, but with the ellipses rotated by 90° . For $\omega_{Et_b} \gg 1$, the plasma smears into a cylinder. As for transport, the quadrupole field increases transport resonantly, not monotonically. The measured properties of the transport agree with some, but not all, of the predictions of a simple model of the effect. The location of the resonance in parameter space moves accordingly as we change the length

and temperature of the plasma. The strength of the transport scales like the square of the perturbation strength. The simple model does not accurately predict the absolute location of the resonance in parameter space and the scaling of the maximum diffusion with temperature is in the wrong direction. We need a better theory of quadrupole induced transport to completely describe the experimental observations.

We believe the data provide a conclusive demonstration of resonant particle transport in a Malmberg-Penning trap. Quadrupole fields are not the sole cause of plasma loss in these traps, but the fields' simplicity offers a relatively simple system in which to study resonant particle transport. Quadrupole field effects are likely present in all Malmberg-Penning traps because of imperfections in the magnet coils. Thus, the results I present in this dissertation are relevant to all who use Malmberg-Penning traps. We see evidence of field errors in our trap as we can actually reduce transport with the application of suitable quadrupole fields.

The implications for antihydrogen research are important. The planned operating parameters of the ATHENA and ATRAP collaborations are in a portion of parameter space where transport is enhanced. Thus, the antihydrogen experiments will face serious problems confining antiprotons and positrons because of transport due to quadrupole fields. Even if the parameters are such that they are off resonance, transport may still lead to excessive plasma loss. In our work, we only need to apply relatively weak quadrupole fields of 20 mG/cm to see a large effect on transport. At the edge of the plasma, the quadrupole field strength is about 20 mG which is much smaller than the typical axial field of 100 G we use. And still, diffusion is two times greater than the background diffusion. In antihydrogen experiments, quadrupole fields with strengths comparable to axial field strengths will be used.

1.4 Outline

Chapter 2. I describe the Malmberg-Penning trap, diagnostics and modifications made to the machine for this experiment.

Chapter 3. I present the results of measurements of the shape of the plasma and compare the results to our expectations.

Chapter 4. I study transport caused within the plasma by the application of the quadru-

pole field.

Chapter 5. I summarize the work presented in this thesis and describe future directions of research.

Appendix A. I describe the CCD camera system.

Appendix B. I present the LabVIEW programs we wrote to control the experiment.

Chapter 2

Experimental Apparatus

2.1 Malmberg-Penning Trap

We performed the quadrupole magnetic field experiments in a Malmberg-Penning trap at U.C. Berkeley, a trap designed to create and trap pure electron plasmas. This chapter describes the trap used for this research; I discuss typical parameters, diagnostic techniques and modifications made to the machine specifically for this research. The generic Malmberg-Penning trap is designed to confine charged particles with one sign of charge. Note that it may be possible to confine particles of both signs simultaneously [25, 26], as is relevant to the antihydrogen experiments [2, 27].

Basic Concept

A Malmberg-Penning trap consists of a series of three or more collimated, cylindrical, conducting rings immersed in a strong axial magnetic field, B_z . Figure 2.1 shows a schematic of a trap with three rings. We apply a large negative voltage, $-V_o$, to the two rings on the ends, while we ground the central ring. In the case of more than three rings, we may apply $-V_o$ to any two nonadjacent rings and ground the rest. With a strong enough applied voltage and a sufficiently strong magnetic field, we trap a column of electrons in this device in the region spanned by the grounded ring(s). The axial magnetic field provides radial confinement while the electric field of the end rings provides axial confinement.

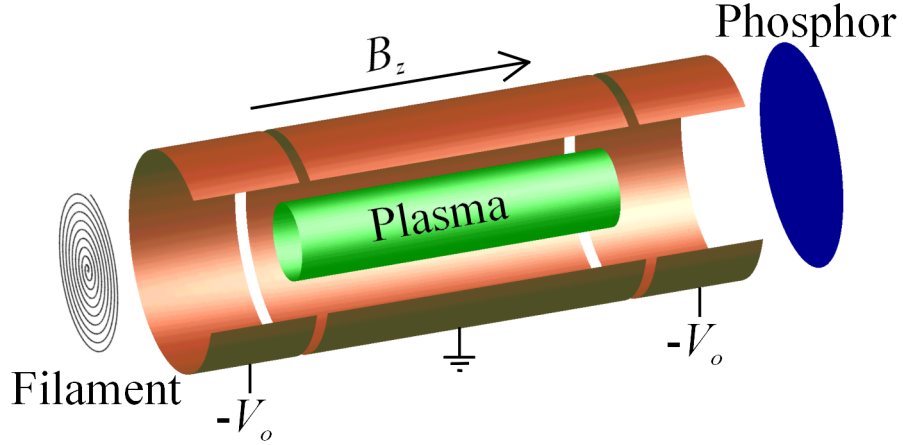


Figure 2.1: A schematic drawing of the machine showing the confinement gates (with a portion cut away to reveal the interior), the filament, the axial field, the plasma, and the phosphor screen. These are the essential components necessary to create, trap, manipulate, and diagnose a pure electron plasma.

Inject Hold Dump Cycle

The source of electrons is thermionic emission from a spiral wound tungsten filament. To control the creation, manipulation, and destruction of a plasma, we set the voltages on the end rings to ground to allow the axial passage of electrons, or we restore the voltages to $-V_o$ to prevent the axial passage of electrons. Therefore, we also call the rings gates. We call the confinement gate closest to the filament the inject gate and we call the confinement gate furthest from the filament the dump gate.

Figure 2.2 shows the typical sequence of events for the creation, manipulation, and destruction of a plasma. When the trap is empty and the inject and dump gates are closed, there are only electrons near the filament. To begin injection, we set the inject gate to ground and electrons fill the trap. Restoring the inject gate to $-V_o$ pinches off the electron column, leaving a trapped plasma. We can now perform any manipulations of the plasma we like. Setting the dump gate to ground allows the plasma to leave the trap and strike the phosphor screen.

Since a spiral filament emits the electrons, we may think of the plasma as having a spiral cross section. However, we prefer plasmas with smooth radial profiles. We hold the inject gate open for at least $(10 + t_{\text{inject}})$ milliseconds to allow instabilities and other transport to fill in the initial spiral shaped plasma, leading to a smooth radial profile. Then,

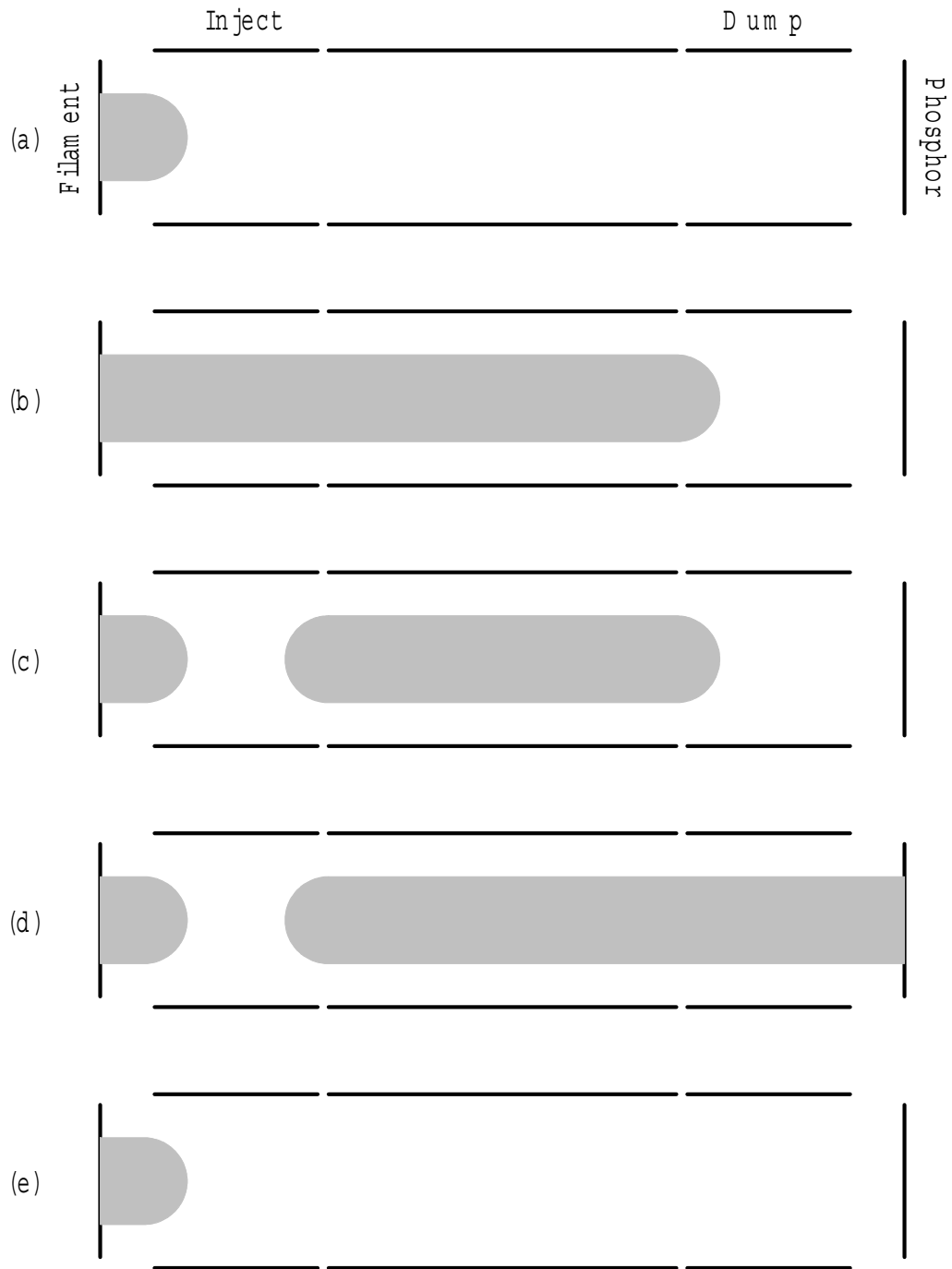


Figure 2.2: (a) An empty trap with $-V_o$ applied to the inject and dump gates. (b) The voltage on the inject gate set to ground, allowing electrons into the trap. (c) The voltage on the inject gate is restored to $-V_o$ to trap the plasma. (d) The voltage on the dump gate is set to zero to dump the plasma onto the phosphor screen. (e) We are left again with an empty trap, ready to repeat the cycle.

we ramp the voltage on the inject gate slowly to $-V_o$. The parameters t_{inject} and t_{ramp} are proportional to the axial magnetic field because the time scales of the relevant dynamics to fill in the spiral shaped plasma scale with the axial field.

We would like t_{inject} and t_{ramp} to be as short as possible while still giving well behaved plasmas. If t_{inject} is too long, we simply waste time. If t_{ramp} is too long, we miss the early evolution of the plasma. We find that if either parameter is too short, different types of maladies arise. The plasma may have spiral structure inherited from the filament. Sometimes dense cores form with diffuse halos. And often, a substantial $\ell = 1$ diocotron mode is created. An $\ell = 1$ diocotron mode is the result of an off axis plasma interacting with its image charge. The image charge produces an electric field that is almost completely radial and this radial field creates an azimuthal drift of the plasma about the trap axis. Lengthening t_{inject} and t_{ramp} solves all of these problems.

The injection, holding, and dumping of a plasma is a process that is reproducible to better than 1%. Therefore, in addition to *in situ* real time measurements, we can measure the time evolution of plasma parameters by simply holding different plasmas for different times. The reproducibility implies that measurements from different plasmas held for different times are roughly equivalent to measurements in one plasma at different times. This is important for measurements that are destructive, requiring that we dump the plasma.

Guiding Center Drifts

There are two motions of the electrons' guiding centers that are important for this research. The first is the motion of the electrons along the axial magnetic field lines. We refer to this as the bounce motion. For a plasma of length L , we make the definition, $t_b = L/v_z$. For a thermal electron, $v_z = \sqrt{kT/m}$.

The second motion is the $\vec{E} \times \vec{B}$ rotation of the electron column about the symmetry axis. The plasma has a net charge and thus a nonzero electric field directed radially inwards. The guiding centers therefore have a drift in the $-\hat{r} \times \hat{z} = \hat{\theta}$ direction. For strongly magnetized plasmas, the guiding center drift velocity is approximately $(\vec{E} \times \vec{B})/B^2$ [28]. One may think of this rotation as giving the plasma the correct velocity so that the $\vec{v} \times \vec{B}$ force can balance the radial electric force. This rotation has the rotation frequency, $\omega \approx \omega_E = E/Br$. For a plasma with constant density, $E = ner/2\pi\epsilon_o$ and so $\omega_E = ne/2\pi\epsilon_o B$. For a plasma finite temperature plasma, ω has contributions from both the $\vec{E} \times \vec{B}$ drift and

the diamagnetic drift. The diamagnetic drift is a fluid drift and not a guiding center drift, so it is not important for the work in this thesis and we ignore it.

There are several ways to vary ω_E and t_b ; vary B_z , L , n , or kT . In practice, the simplest parameter to vary is B_z . Varying L is straightforward as well; we choose various gates to be the inject and dump gates. We can decrease the density by waiting because the density naturally decreases as a function of time. It is more difficult to increase the initial density because the filament is already set to provide the maximum density. We could achieve further density increases by stacking techniques [29]. We can increase the temperature by applying a noise signal to the wall of the trap, but we are more interested in cooling the plasma and this is difficult to do without adding a background gas against which the plasma can cool. These plasma parameters are not independent, and so after setting machine parameters, we measure all parameters and calculate ω_E and t_b .

Vacuum System, Main Magnet & Steering Coils

The experiment sits inside of an ultra high vacuum chamber where we maintain the pressure at approximately 4×10^{-10} Torr. The exterior of the vacuum chamber has the copper wires of the large solenoidal magnet wound directly on it. There are no direct measurements of the axial field, and so we model the magnet coils as a collection of finite length solenoids of assorted radii. This model shows that we get a magnetic field of 7.9 G/A. With our power supply delivering 200 A, the magnet produces 1580 G. The magnetic field in the region over which the experiment itself sits is uniform to within 0.1%. There are two pair of Helmholtz-like coils to correct for the possible misalignment of the trap with respect to the main magnet, and to account for the transverse component of the Earth's magnetic field. I discuss these coils in more detail below when I discuss quadrupole magnetic fields.

The copper wires of the main magnet are hollow so that we may cool them with water from a cooling tower on the roof of the building. The temperature of this water varies diurnally, seasonally and with the weather. A typical variation from morning until midafternoon is 10 °F. For $B_z < 400$ G, the magnet does not heat the water significantly. But at $B_z = 1500$ G, the magnet heats the water by 20 °F. The temperature of the system is determined by both the temperature of the inflowing water and the heat generated by the main magnet. This temperature variation can cause thermal expansion and can be important for correctly tuning machine parameters. We therefore strive to minimize this

temperature variation either by minimizing the duration of experiments or by retuning the system on a shorter timescale than the temperature variations.

Filament

A tungsten filament¹ wound into a planar spiral with 12 turns and a diameter of 0.970" produces electrons by thermionic emission. The filament wire is 0.014" in diameter. Approximately 6 Amperes and 13.84 Volts drive the filament and it glows white hot. Optical pyrometer measurements indicate the filament temperature is ~ 1600 °C. As I describe below, we must attempt to minimize this light pollution. Testing of the filament shows that increasing the current beyond 6 A only increases the light output and does not lead to denser plasmas because the filament emission becomes space charge limited.

The filament sits inside a grounded copper ring of its own at the end of the series of collimated copper rings used for confining the plasma. We hold the filament in place by crimping its ends into hollow stainless steel posts. Behind the filament is a stainless steel disk that is welded to the center stainless steel post. Since the current is set to flow through the filament from the outer edge down to the center, this disk is at a lower potential than the body of the filament. Therefore, the disk serves to reflect electrons back into the trap that would otherwise head in the wrong direction.

We place a bias voltage on the center post of the filament to enable or suppress the electrons from leaving the region near the filament and entering the trap. We apply a positive voltage of +10 V to suppress injection. The enabling voltage ranges from 0 to -40 V. A bias voltage less than the voltage across the filament allows us to inject plasmas that have a smaller radius than the filament's radius. However, the voltage mismatch that occurs between the filament and the natural space charge of the injected plasma heats these plasmas.

Parameters Values

Table 2.1 shows fixed values, typical values, and value ranges for the various machine parameters.

¹Manufactured by R.D. Mathis Co., Long Beach, CA.

Parameter	Value
r_{wall}	1.905 cm
p	4×10^{-10} Torr
L	2 – 34 cm
B_z	40 – 1500 G
Ω	$0.7 - 2.6 \times 10^9$ rad s ⁻¹
$\omega_{p \text{ max}}$	2×10^8 rad s ⁻¹
ω_E	$0.4 - 4.0 \times 10^6$ rad s ⁻¹
r_L	1 mm
t_{hold}	$4\mu\text{s} - 10$ s
t_b	$0.7 \mu\text{s}$
ν_{ee}^{-1}	3 ms
n_{max}	2×10^7 cm ⁻³
kT	1 eV
λ_D	0.5 mm

Table 2.1: This table shows typical parameters and parameter ranges accessible in the U.C. Berkeley Malmberg-Penning trap.

2.2 Diagnostics

Diagnostics fall into two categories, destructive and nondestructive. In a destructive measurement, we must destroy the plasma by dumping it in order to make the measurement. In a nondestructive measurement, we make the measurement without disturbing the plasma. The wall of the trap itself is one diagnostic and may be used either destructively or nondestructively. We detect the image charge on the wall that the plasma induces. A phosphor coated glass substrate is the second diagnostic. Dumping the plasma onto the phosphor produces an image whose brightness is proportional to the z integrated plasma density. A CCD camera that looks through a viewport into the vacuum chamber images this light.

2.2.1 The Wall

The electrons induce image charges on the walls and since the copper gates have a finite capacitance to ground, there is a corresponding voltage proportional to this image charge. We read this voltage directly if the gate is not grounded.

We divided two of the gates in the machine into electrically isolated azimuthal sectors for measuring the angular dependence of the image charge. The sectored gates are useful in the nondestructive mode for measuring the frequencies of various azimuthal modes of the plasma. Note that the wall of the trap may also be used to drive plasma modes in addition to detecting them [30, 31, 32].

Alternatively, we can use the wall as a Gauss' Law probe, a destructive technique that gives the total charge that resides within the gate being measured. When we dump the plasma, the image charge on the wall returns to ground and we measure the corresponding voltage. We use this technique with the sectored gate to measure the shape of the plasma.

2.2.2 The Phosphor

We have a glass substrate² coated with indium tin oxide for electrical conductivity, phosphor (P-43) for light emission, and finally aluminum for blocking unwanted light. We use the phosphor screen in two modes of operation, as a charge collection plate and as an imaging device. When we use the phosphor as a charge collection plate, we simply dump the plasma and read the voltage produced on the phosphor due to its capacitance to ground. When we use the phosphor as an imaging device, we accelerate the electrons with a high voltage into the phosphor coated screen, as in a television or in an oscilloscope. We apply 16 kV to the phosphor screen to accelerate electrons out of the trap and form an image that is a z integrated, pancaked, version of the plasma. The CCD camera records an image of this light.

Background Subtraction

Because of the bright light emitted from the filament, we take an image with no plasma present to subtract from subsequent images when there is a plasma present. Figure 2.3 shows a typical background image. By subtracting the background image, we measure only light that comes from electrons striking the phosphor screen. Figure 2.4 shows a

²Manufactured by Grant Scientific, Gilbert, SC.

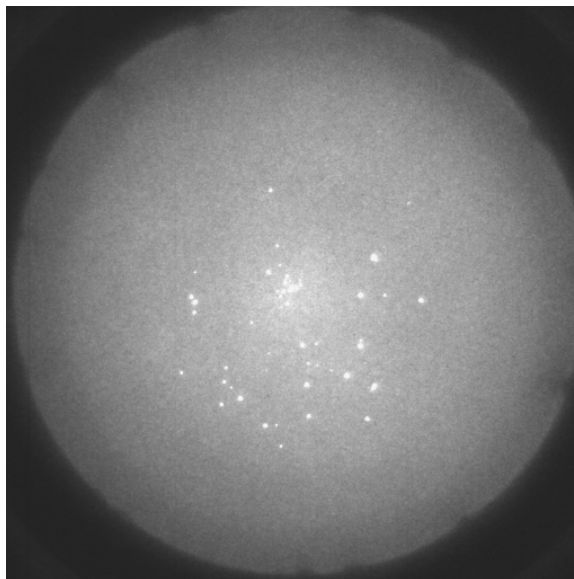


Figure 2.3: An image of the background light, with no plasma present. We subtract this image from other images so that we have only the light from the plasma striking the phosphor. Note the pinholes that are places where the aluminum has been lost. The image analysis software replaces these bright spots with an average of their nearest neighbors.

background image, an image of a plasma before subtracting the background, and the final image after background subtraction. Note the pinhole defects in the phosphor in Figures 2.3 and 2.4. These are spots where the aluminum layer has been reduced. Figure 2.4 shows that background subtraction is effective at removing these defects from the plasma images. To ensure that the pinholes do not affect the data analysis, we replace the values of the pinhole pixels with an average of their nearest neighbors.

We take several steps to minimize the background light before acquiring the background image. The phosphor screen, which sits between the filament and the camera, has a coating of aluminum. This coating blocks most of the light coming from the filament, reducing the white hot glow to a gentle orange glow. We outfitted the camera lens with a 22 nm passband optical filter that is tuned to the 545 nm emission wavelength of the phosphor. We set the electronic shutter on the CCD camera to be as short as possible to minimize the signal from the constant glow of the filament while still capturing all of the light from electrons striking the phosphor screen.

Even with all of the measures we take to reduce the background light, the plasma produces a light signal that is at most only a factor of 10 greater than the background at

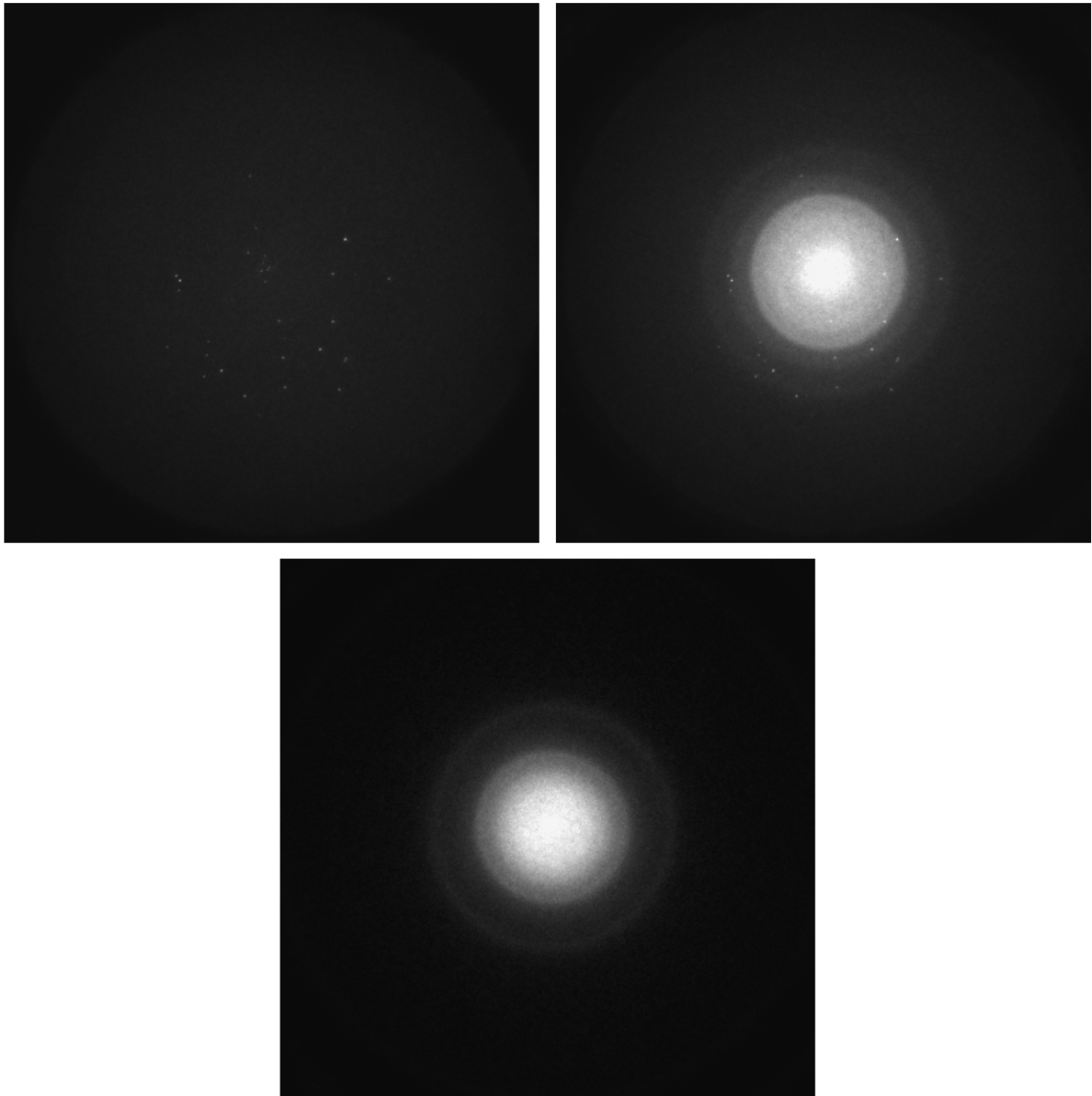


Figure 2.4: The image in the upper left is the same background image from Figure 2.3 but with the brightness reduced so as to be on the same scale as the other images in this Figure. The image in the upper right is an image of a plasma before background subtraction. The bottom image is the final image of the plasma after subtracting the background image.

any given pixel. The total brightness of a plasma image is only 40% brighter than an image of the background, however. Testing the background subtraction by subtracting the saved background image from successive images of no plasma in order to obtain a “null” image shows that the cancelation is good to the level of 1%.

Over the course of an hour or so, random mechanical vibrations in the laboratory from sources such as passing trucks outside or slamming doors in the building cause the camera alignment to change and the background image appear to be offset. There are fluctuations in the temperature of the room and thermal expansion may change the mechanical alignment of the camera. And, even though the camera is mostly isolated from changes in the room temperature by being in a temperature regulated box (see Appendix A), thermal fluctuations can still change the brightness of the images. For these reasons, we acquire a new background image periodically, waiting no more than one hour between background images.

Clipping and Threshold

After subtracting the background image, we can make two further image manipulations. We clip the image by setting all pixels to zero beyond the radius where we know the wall of the trap to be. This eliminates some portion of the scattered light that does not represent where electrons strike the phosphor screen. Next, we sometimes enforce a threshold pixel value. At first, we set to zero all pixels with negative values. Ultimately, however, we found it better to skip the threshold procedure. Because image noise is both positive and negative, quantities such as the RMS plasma radius behave better if we keep the negative pixel values.

Image Faithfulness

Ideally, the accelerating electric field would be purely axial in order to not distort the image. But there are difficulties in enforcing the boundary conditions necessary to create axial electric field lines. The radial component of the imaging electric field causes a radial compression of the image and the $\vec{E} \times \vec{B}$ drift causes a rotation of the image. Figure 2.5 shows the result a numerical solution for the electric potential created by the phosphor, $\phi(r, z)_{\text{phos}}$.

The radial compression amounts to a mapping $r \rightarrow m(B_z)r$ where $m(B_z)$ is a

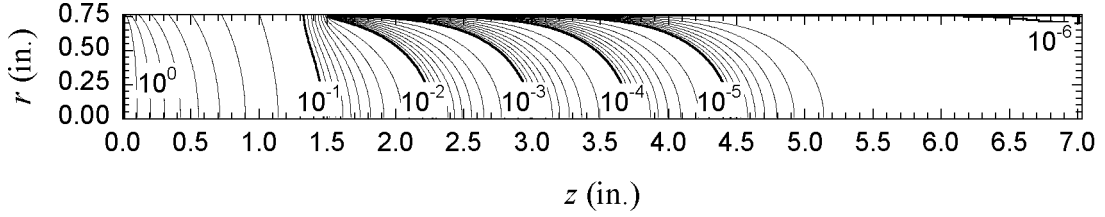


Figure 2.5: Making simplifying assumptions about the geometry of the system, we solve for the potential created by the phosphor screen. The phosphor screen and the trap walls have a radius of 0.75". The vacuum chamber has a wall radius of 3.50" and is not shown here. The phosphor sits at $z = 0$ in this Figure, 1.50" away from the last confinement gate. The phosphor is at $\phi = 1$ while the confinement gates and vacuum chamber walls are at $\phi = 10^{-6}$. The contours are logarithmically spaced and show that there is a significant radial component of the electric field.

magnification factor dependent on B_z . We take images of the electrons streaming off of the filament and measure the radial compression as a function of B_z . Figure 2.6 shows that the result is $m \approx [200/B_z(G)]^{0.28}$ for $B_z \leq 200$ G. The compression is less for smaller phosphor voltages, but using voltages of less than 16 kV results in plasma images that are not sufficiently bright.

Averaging

The reproducibility of the system allows us to average multiple camera images. We find that averaging five images is sufficient to reduce the pixel noise. Averaging more than five images only marginally improves the statistics but it increases the duration of the experiment. Many of our data runs take several hours and so a difference of 20% is quite significant. It is important that the background image have little noise because we subtract it from every subsequent image. Therefore, the background image is an average of twenty images.

2.3 Measuring Plasma Parameters

We use the walls of the trap and the phosphor screen to measure the total charge in the plasma, Q , the transverse profile of the plasma density, $n(r, \theta)$, and the on axis axial temperature of the plasma kT_{\parallel} . We measure the length of the plasma, L , by using an

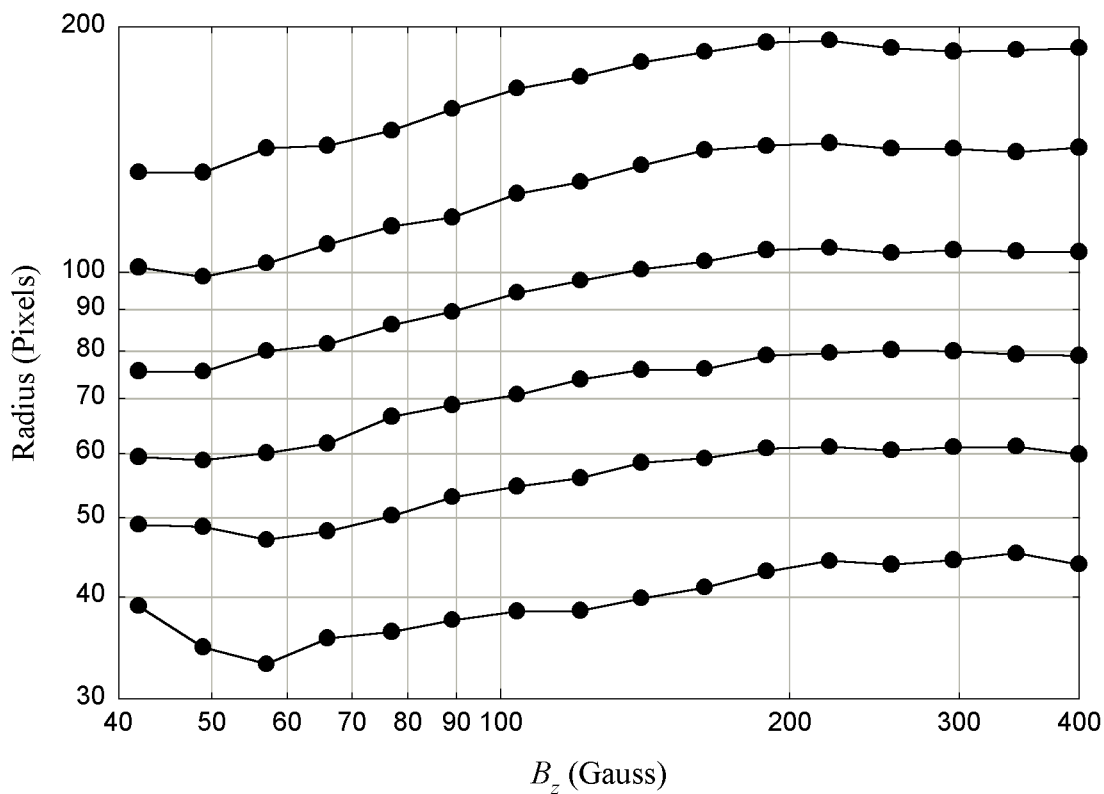


Figure 2.6: We measure the radial compression of an image as a function of B_z by imaging the filament and measuring where each turn of the spiral appears to be. Above 200 G, the curves are flat and there is no noticeable compression of the image. Below 200 G, the compression scales like $B_z^{0.28}$. Each line in this Figure is a different turn of the filament.

iterative r - z Poisson solver that finds a self consistent solution that corresponds to an image of the plasma.

2.3.1 Total Charge

Phosphor

When we dump the plasma, all of the electrons end up on the phosphor. We find the total charge, Q , from $Q = C_{\text{phos}}V_{\text{phos}}$. We measure the phosphor capacitance C_{phos} by including it as one leg in a capacitive voltage divider (see Figure 2.7) while using

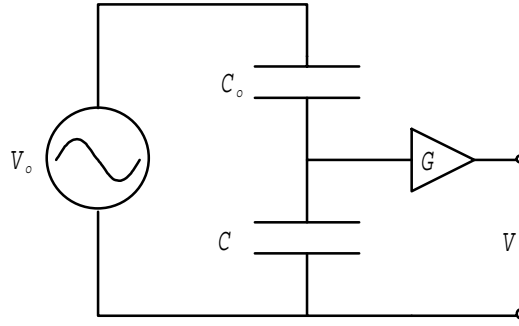


Figure 2.7: We use a simple capacitive voltage divider to measure the capacitance of the phosphor screen or a gate. A series of known capacitances, C_o , forms one leg of the voltage divider while the unknown capacitance C forms the other. We measure the output voltage, V , as a function of V_o , C and the frequency of the oscillator.

various capacitors of known values, C_o , as the other leg. A function generator drives the voltage divider with sine waves and we measure the amplitude of the output as a function of frequency. For a known capacitance, C_o , and drive voltage, V_o , the measured signal is $V = GV_o C_o / (C + C_o)$, where G is the gain of any amplification stages. By using $C_o \gg C$, which we verify *a posteriori*, $V \approx GV_o$ and we measure GV_o . Then we solve for C ,

$$C = C_o \left(\frac{GV_o - V}{V} \right). \quad (2.1)$$

The slope of the graph of C_o versus $V/(GV_o - V)$ shown in Figure 2.8 yields C_{phos} . The result is that $C_{\text{phos}} \approx 300$ pF. Severe noise pickup from the leads connecting the phosphor to the outside of the vacuum chamber greatly hampers this method of measuring Q . Also, there appears to be a tenuous electrical connection to the phosphor. This results in the charging up of the phosphor and gives shot to shot variations. These problems make measuring Q from the phosphor dubious at best. Instead, we rely on Gauss' Law probes.

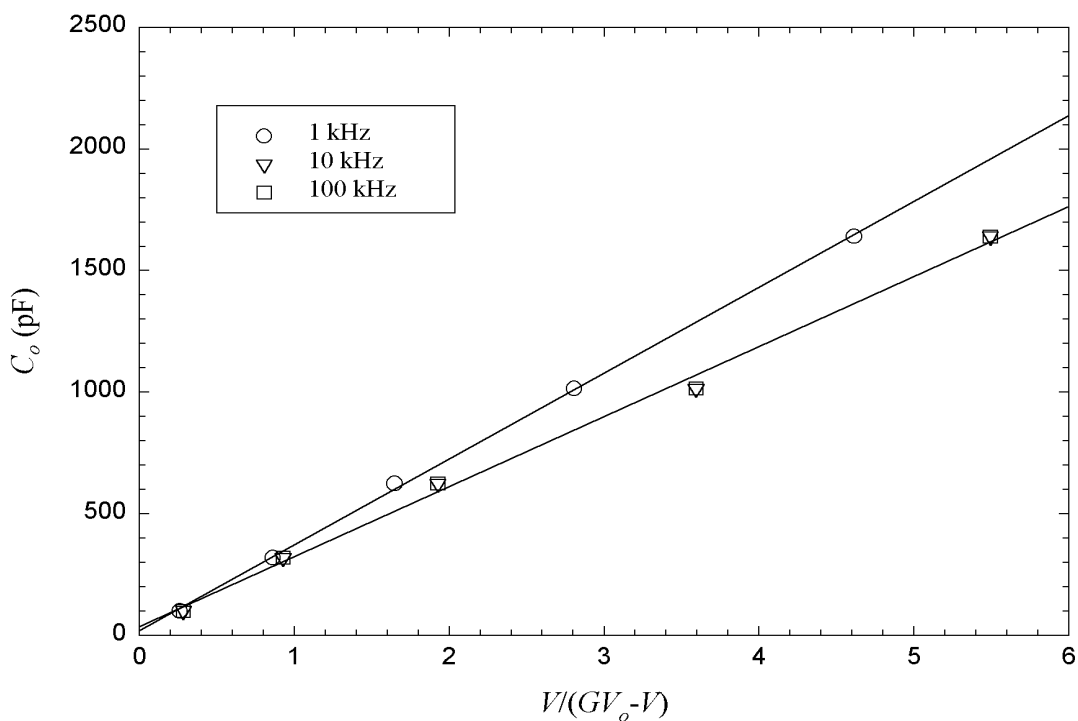


Figure 2.8: We measure the output voltage V of a voltage divider with the phosphor screen as one leg, and a known capacitance C_o as the other leg. The slope of each line gives the capacitance of the phosphor screen or gate for each of several frequencies. Above 10 kHz, the slope is 300 pF.

Gauss' Law Probe

When we hold a plasma in the trap, there is an image charge induced on the grounded hold gates equal in magnitude to the plasma charge within the axial extent of those gates. When we dump the plasma out of the trap, this image charge runs to ground. This allows us to measure $Q_{\text{gate}} = C_{\text{gate}}V_{\text{gate}}$. If we assume that the plasma is axially uniform over the extent of the gate, then we are measuring the number of electrons per unit length, λ . If we assume that L is simply the distance between the two confinement gates (a good assumption for long plasmas), then $Q = Q_{\text{gate}}L/L_{\text{gate}} = C_{\text{gate}}V_{\text{gate}}L/L_{\text{gate}}$. Note that λ is a more robust measurement than Q here because λ does not depend on the length of the plasma, L , which is difficult to measure accurately.

$\ell = 1$ Diocotron Frequency

If we measure the frequency of the $\ell = 1$ diocotron mode, we can deduce λ . If a plasma with λ electrons per unit length is off axis by an amount D , then it induces an image plasma on the wall. The image is equivalent to a plasma with $-\lambda$ at $r = r_{\text{wall}}^2/D$. The electric field from this image causes an $\vec{E} \times \vec{B}$ drift in the azimuthal direction. The linear frequency of the $\ell = 1$ diocotron mode is $\omega_o = \lambda e/2\pi\epsilon_o B_z r_{\text{wall}}^2$. The nonlinear frequency for finite mode amplitude is $\omega_D = \omega_o(1 - D^2/r_{\text{wall}}^2)^{-1}$. Fine and Driscoll [33] have derived a formula that further corrects for finite length and temperature effects. Their result is,

$$\frac{\omega}{\omega_D} = 1 + \left[\frac{j_{01}}{2} \left(F + \frac{4\pi\epsilon_o kT}{\lambda e^2} \right) - 0.671 \right] \left(\frac{r_{\text{wall}}}{L} \right), \quad (2.2)$$

where j_{01} is the first zero of the zeroth order Bessel function J_0 . The quantity F is the electrostatic energy per unit length for a flat topped plasma with unit λ : $F = 1/4 + \ln(r_{\text{wall}}/r_p)$. Since we have rather Gaussian plasmas, we use

$$\begin{aligned} F &= \int_0^{r_{\text{wall}}} \frac{1}{2} \epsilon_o E^2 2\pi r dr \\ &= \int_0^{r_{\text{wall}}} \frac{1}{2} \epsilon_o \left[\frac{e}{2\pi\epsilon_o r} \int_0^r n(r') 2\pi r' dr' \right]^2 2\pi r dr \end{aligned} \quad (2.3)$$

and we choose $n(r)$ to be a Gaussian normalized to unity. We calculate F numerically. Knowledge of kT and L , and a measurement of ω is therefore sufficient to calculate λ . These techniques agree with each other to within a few percent for determining λ and so we use the Gauss' Law probe method because of its simplicity.

CCD Image

We can convert the brightness of a CCD camera image to plasma density and thus deduce Q . If the phosphor is spatially uniform and linear, and if the CCD camera system is uniform and linear, then the total brightness of a camera image, T (in units of pixel brightness, or “cams” for “camera units”), is proportional to the total amount of charge, Q . Moreover, the brightness of any pixel is proportional to the z integrated density at the location of the pixel. To calibrate the camera images, we first use the Gauss’ Law probe technique to measure $\lambda = C_{\text{gate}}V_{\text{gate}}/eL_{\text{gate}}$. By assuming L , we write $Q = \lambda L$ and the conversion factor from cams to number of electrons is

$$\frac{\text{cam}}{e^-} = \frac{TeL_{\text{gate}}}{C_{\text{gate}}VL} \quad (2.4)$$

This value should be constant and we measure it to be 0.31 cam/ e^- for 16 kV of phosphor voltage and a camera gain of 150.

2.3.2 Density

We can further calculate what electron density each pixel corresponds to. We need the factor cam/ e^- just calculated and the “size” of the pixels. We observe that the camera’s field of view includes screws that hold the phosphor screen in place and we know how far apart these screws are. We calculate that 126.10 pixels corresponds to 1 centimeter. Therefore, the “size” of a pixel is $(126.10)^{-2} \text{ cm}^2$. So for a particular pixel the z averaged number density of electrons is

$$\begin{aligned} n &= \text{PixelValue} \left(\frac{e^-}{\text{cam}} \right) \left(\frac{1}{\text{Volume}} \right) \\ &= \text{PixelValue} \left(\frac{C_{\text{gate}}VL}{TeL_{\text{gate}}} \right) \left(\frac{126.10^2}{L} \right) \\ &= \text{PixelValue} \left(\frac{C_{\text{gate}}V}{TeL_{\text{gate}}} \right) (126.10)^2. \end{aligned} \quad (2.5)$$

This is independent of L and only requires that the plasma have some well defined and uniform L . Therefore, even if we are relatively uncertain about the precise value of L , this calibration of density is more accurate than the calibration of cam/ e^- . For a 28 cm long plasma, 16 kV of phosphor voltage, and a gain of 150, the calibration is $1724 \text{ cm}^{-3}/\text{PixelValue}$.

2.3.3 Length

So far, the length of the plasma is a poorly defined quantity. Because of the thermal spread in electron energies, the radial dependencies of the plasma itself and the confinement potentials, and the strength of the confinement potentials, the plasma length is a function of r , kT , and V_o . Ignoring these effects, one might say that the length of the plasma is simply the distance between the confinement gates. The larger this distance, the better this assumption is. However, even for the longest plasma that we can trap, using confinement gates separated by 34.02 cm, we find that a better estimate of the plasma length is 28 cm.

We use an iterative r - z Poisson solver method [34, 35] in which we take an image of the plasma to be the z integrated density profile of a plasma, $n(r)$, held between the confinement gates. We find the potential that corresponds to this density distribution, compute $n_o \exp(e\phi/kT)$, and use this as the source term in Poisson's equation. We repeat this process using the new solution for $\phi(r, z)$, at each iteration we require that the z integrated density equals $n(r)$. We stop after reaching sufficient convergence. This technique assumes that the plasma is in global thermal equilibrium and that we know the temperature. Knowing $\phi(r, z)$ allows us to calculate L as the turning points of an electron with axial velocity v_{th} .

2.3.4 Temperature

We measure the axial temperature of the plasma using the technique described by Eggleston *et. al.* [36]. We slowly raise the voltage on the dump gate from $-V_o$ to ground. Because the charged plasma column has a space charge potential and a finite temperature, hot electrons that are on axis will be able to leak out the trap first. By collecting these first electrons, we do not greatly disturb the plasma and we measure the tail of the Maxwellian distribution. From this, we extract kT .

$$\frac{d \ln Q_{esc}}{d e\phi} = \frac{-1.05}{kT}. \quad (2.6)$$

The amount of charge that has escaped is Q_{esc} . Typical temperatures are about 1 eV.

2.4 Modifications

Since the experiments performed by Notte [29], Peurrung [37], Hansen [38] and Reimann [39] with the U.C. Berkeley Malmberg-Penning trap, we made several modifications. These include changing the filament, rearranging the gates, installing a new imaging system, and adding quadrupole magnets.

2.4.1 Filament

The previous filament was a spiral, divided into eight segments of equal arclength. Each segment was electrically isolated, mounted separately, and driven by a separate power supply. The purpose of this design was to allow finer control of the injected plasmas.

However, the correct alignment of these segments was torturously difficult. Often, adjacent segments would touch one another, shorting out the flow of electricity, making for uneven electron emission. In practical use, this restricted the number of usable segments and thus the maximum plasma radius allowed. Moreover, the 16 quarter inch diameter, 75 cm long copper rods used to deliver power to the filament were unwieldy during machine maintenance.

A single, continuous, filament replaces the segmented filament. This solves the shorting problems, and now we need only two copper rods to deliver power to the filament. There are still alignment problems however; the filament is not exactly centered in the trap and a slight torque has made the spiral nonuniform. See Figure 2.9.

2.4.2 Gates

To better serve the goals of our experiment, we changed the ordering of the gates inside the machine. We placed as many gates of similar length next to one another as possible. We added a gate to the end of the machine to allow for longer plasmas. Lastly, we replaced a two-sectored gate with a four-sectored gate to allow the measurement of quadrupole signals. Figure 2.10 shows the design of the four-sectored gate and Figure 2.11 shows the arrangements of the gates within the machine.

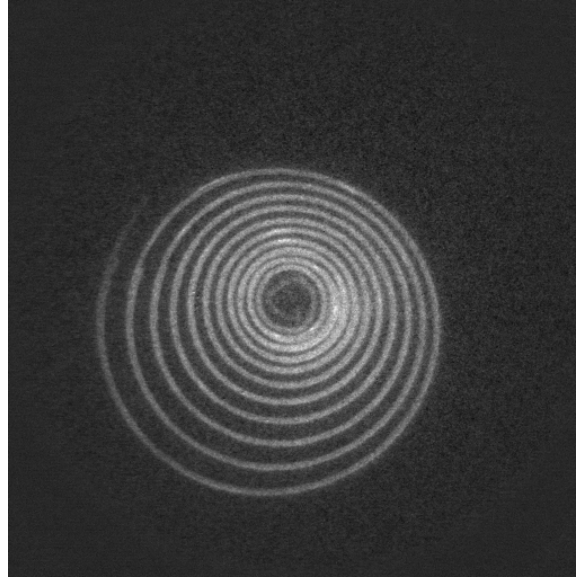


Figure 2.9: This image of the filament is actually an image of free streaming electrons, (not a trapped plasma), coming directly from the filament. This is not light emitted from the filament. An accidental slight twist during installation gives the filament its asymmetric appearance. By setting t_{inject} and t_{ramp} properly, we still create a symmetric plasma.

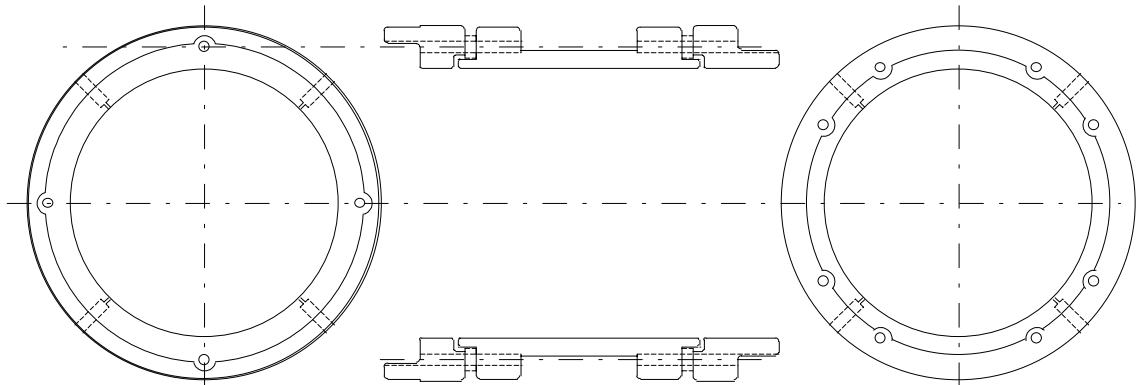


Figure 2.10: We installed a new four-sectored gate in order to measure quadrupole signals. The entire wall area is part of one sector or another, i.e. there is no “body”. Electrically isolated end rings hold the sectors together. Small ceramic washers act as standoffs to electrically isolate the pieces and ceramic pins hold the pieces together.

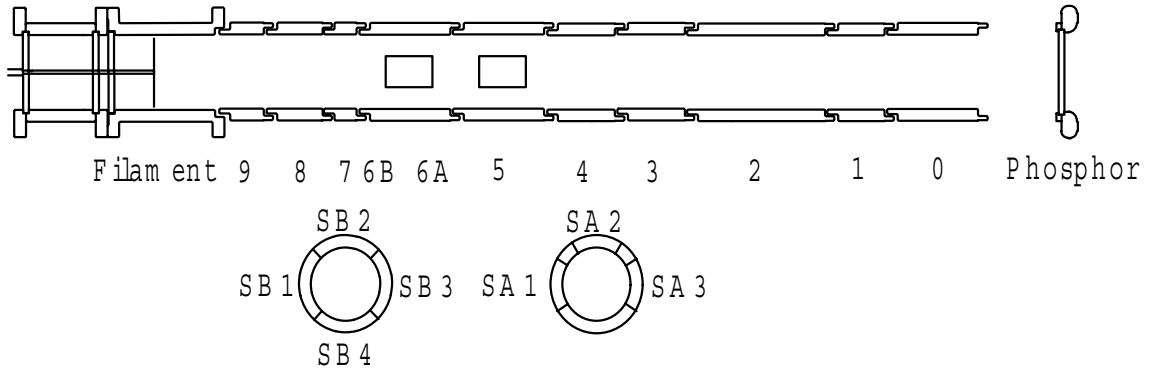


Figure 2.11: This scale drawing shows the arrangements of the gates inside the machine. The first two gates on the far left support and house the filament. Gates 0 through 9 are used to inject, hold, analyze and dump the plasma. The phosphor screen sits to the far right. End views of gates 5 and 6 show the sectors. Gate 5 has three sectors 90° apart and 50° in extent. Gate 6 has four sectors 90° in extent.

2.4.3 Imaging System

In order to create an image of the plasma that is a faithful z integrated version of the plasma, the accelerating electric fields should be purely axial. In a parallel plate configuration, the potential is constant in any transverse plane, and varies linearly with distance. In the previous machine configuration, a grid and acceleration rings were put in place to enforce the correct boundary conditions. The phosphor is an equipotential surface at 16 kV. A stack of 20 copper rings, separated by $1\text{ M}\Omega$ resistors, was placed between the phosphor and the last confinement gate. The phosphor and the first ring were at 16 kV. The last ring was grounded. Thus, the potential decreased linearly in the z direction. Finally, a fine grid of tungsten wire was woven across the face of a ring and placed next to the last gate. This grounded grid represents an approximate equipotential surface while still allowing electrons to be dumped from the trap.

There were two problems with this design. The support structure for this assembly was inadequate and the grid itself interfered with plasma imaging.

The stack of rings was held together by brittle Macor rods. Vacuum compatible, electrically insulating supports needed to be used, but the geometry of the system required that the Macor rods be very thin. The rods were 3.700" long and 0.086" in diameter and had 0.035" of 2-56 threading on each end. During machine maintenance, these rods often broke. Over time, the screw holes on the large Macor disk that holds the phosphor in place

began to crumble, reducing the tolerance. With these two problems, the alignment of this acceleration stage became difficult and we isolated the acceleration rings from the last gate by inserting Teflon spacers. Unfortunately, these spacers charged up and created soft glows in the camera images.

At high phosphor voltages necessary for bright images, the grid altered the trajectories of the electrons, resulting in striping in the images. We finally decided to remove the grid and acceleration rings altogether. We are left with the configuration described above.

2.4.4 Quadrupole Magnets

To apply a transverse, axially invariant, quadrupole magnetic field, we use two different sets of coils. One set of coils are planar hexagons and the other set is an elongated box.

Quadrupole Fields

In the absence of currents and time dependent electric fields, $\vec{\nabla} \cdot \vec{B} = 0$ and $\vec{\nabla} \times \vec{B} = 0$. The possible axially invariant magnetic fields in cylindrical coordinates are of the form $\vec{B}_n = \vec{\nabla} \psi_n$, where $\psi_n(r, \theta) = \beta r^n / n \exp[in(\theta - \theta_o)]$. These ψ_n are the two dimensional simplifications of the three dimensional potential, $\Psi_n(r, \theta, z) = \beta' J_n(kr) / n \exp[in(\theta - \theta_o) \pm kz]$ in the limit $k \rightarrow 0$. The constants β and β' are arbitrary coefficients. It is useful to enumerate the first several ψ_n in both polar and cartesian coordinates to identify the corrections to the desired quadrupole field when we Taylor expand the field produced by the coils in the lab.

The $n = 1$ field is the dipole field

$$\vec{B} = B_x \hat{x} + B_y \hat{y}. \quad (2.7)$$

The $n = 2$ field is the quadrupole field

$$\begin{aligned} \vec{B} &= \beta_1(x\hat{x} - y\hat{y}) + \beta_2(y\hat{x} + x\hat{y}) \\ &= \beta r \left(\cos[2(\theta - \theta_o)]\hat{r} - \sin[2(\theta - \theta_o)]\hat{\theta} \right), \end{aligned} \quad (2.8)$$

where $\beta^2 = \beta_1^2 + \beta_2^2$ and $\tan(2\theta_o) = \beta_1/\beta_2$. We may use either β and θ_o or β_1 and β_2 to describe the quadrupole field. Figure 2.12 shows the field lines for the magnetic field in equation 2.8. We can simply approximate the quadrupole field with $\theta_o = 0$ in the laboratory

Polar $n\psi_n$	Cartesian $n\psi_n$
$r \cos(\theta)$	x
$r \sin(\theta)$	y
$r^2 \cos(2\theta)$	$x^2 - y^2$
$r^2 \sin(2\theta)$	$2xy$
$r^3 \cos(3\theta)$	$x^3 - 3xy^2$
$r^3 \sin(3\theta)$	$-y^3 + 3x^2y$
$r^4 \cos(4\theta)$	$x^4 - 6x^2y^2 + y^4$
$r^4 \sin(4\theta)$	$4x^3y - 4xy^3$
$r^5 \cos(5\theta)$	$x^5 - 10x^3y^2 + 5xy^4$
$r^5 \sin(5\theta)$	$y^5 - 10x^2y^3 + 5x^4y$
$r^6 \cos(6\theta)$	$x^6 - 15x^4y^2 + 15x^2y^4 - y^6$
$r^6 \sin(6\theta)$	$6x^5y - 20x^3y^3 + 6xy^5$

Table 2.2: The scalar magnetic potentials for axially invariant, cylindrically symmetric geometry in both polar and cartesian coordinates.

by four infinitely long straight current carrying wires arranged at the corners of a square, and with alternating directions. The current density distribution is

$$\vec{J} = I\hat{z}\left[\delta(x-d, y-d) + \delta(x+d, y+d) - \delta(x-d, y+d) - \delta(x+d, y-d)\right]. \quad (2.9)$$

The magnetic scalar potential produced is

$$\psi = \frac{\mu_o I}{\pi} \left(\psi_2(r/d, \theta) - \frac{1}{4}\psi_6(r/d, \theta) + \dots \right) \quad (2.10)$$

The next highest order correction to the quadrupole field from this current distribution is the $n = 6$ dodecapole field. Since $r/d \sim 0.15$ in our experiments, this correction is 10^4 times smaller than the quadrupole term. To allow for quadrupole fields with arbitrary θ_o , we constructed two sets of quadrupole field coils that are rotated by 45° with respect to one another, the hexagonal coils for $\theta_o = 0$ (the β_1 direction) and the box coils for $\theta_o = 45^\circ$ (the β_2 direction). As discussed below, the largest field errors in the coils used in the experiment come from the specific geometry of the coils and not the $n = 6$ correction just described.

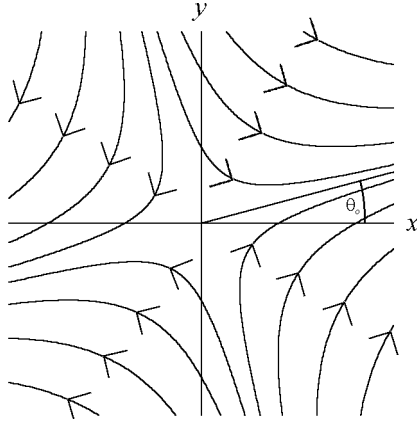


Figure 2.12: The magnetic field lines for the $n = 2$ quadrupole field at an angle θ_o . The field lines have a four-fold symmetry.

Hexagonal Coils

We performed initial experiments with quadrupole coils wound on preexisting frames that we use for creating dipole fields. The frames are hexagonal to optimize their performance as dipole magnets. Truly axially invariant coils would be straight, but there must be end pieces that allow the current to be continuous and these end pieces create perpendicular fields themselves. To compensate for this extra dipole field, the original designers of the machine bent the centers of the frames outwards to reduce their effect. The result is a hexagonal frame shown in Figure 2.13. One pair of hexagonal coils is for B_x and one pair is for B_y .

We use these frames to create quadrupole fields by winding 36 extra turns of wire around the hexagonal forms. If the current in the coils in a pair runs in opposite directions as in the third picture in Figure 2.13, then we get a quadrupole field. The bowing out and the end pieces of the hexagonal coils are problematic, however. A single pair of hexagonal coils produces a field that is mostly a quadrupole, but “stretched” in the x or y direction. There is also a significant axial dependence. The first two pictures in Figure 2.13 show that the two pairs are different sizes. We found that by keeping the ratio of currents in the two pair of coils fixed at 1.391, we minimize the transverse asymmetry and the strong axial dependence.

Using the law of Biot-Savart, we simulate the fields produced by these coils. We hope to understand the results of the simulation as the sum of the basic fields represented

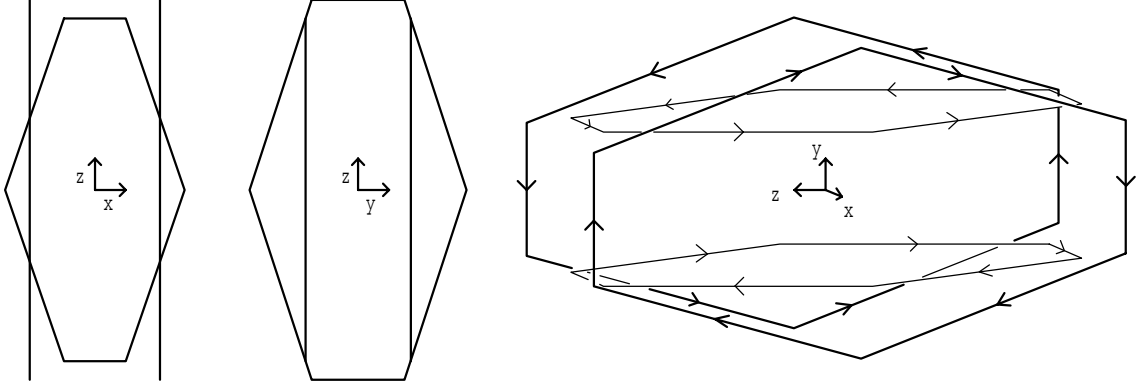


Figure 2.13: The first picture shows the $x - z$ plane while the middle picture shows the $y - z$ plane. These hexagonal coils were originally designed to create dipole fields. But by changing the polarity of the currents so that the currents flow as in the picture on the right, they also serve to produce quadrupole fields.

by Ψ_n and ψ_n . A single pair of hexagonal coils has a significant magnetic cusp component, Ψ_0 . However, when we add the fields of the two pairs of hexagonal coils, these cusp fields mostly cancel, leaving a field that we cannot easily represent by Ψ_n and ψ_n . So instead, we model the resulting cusp field as a polynomial of the form $B_z = a_1z + a_3z^3 + a_5z^5 + a_7z^7$. We assume that $B_r \ll B_z$ and write $B_r = -\frac{r}{2} \partial B_z / \partial z$. After we account for this field, an axially dependent quadrupole field Ψ_2 and an axially invariant quadrupole field ψ_2 remain.

$$\begin{aligned}
 \vec{B}_{\text{Hex}} &= (x\hat{x} - y\hat{y}) \\
 &\quad - 0.457 \left[\cos(k_1z)(x\hat{x} - y\hat{y}) - \frac{k_1r^2}{2} \sin(k_1z) \cos(2\theta)\hat{z} \right] \\
 &\quad + \left(-6 \times 10^{-5}z - 0.04z^3 + 0.3z^5 - 0.2z^7 \right) \hat{z} \\
 &\quad + \frac{r}{2} \left(6 \times 10^{-5} + 0.12z^2 - 1.7z^4 + 1.4z^6 \right) \hat{r}, \tag{2.11}
 \end{aligned}$$

where $k_1 = 3.628 \text{ m}^{-1}$, and x , y and z are in meters. This fit to the numerically calculated field is best at the origin. At $r = r_{\text{wall}}, z = 0$, the fit is only 0.1% off. At $r = 0, z = \pm 0.25 \text{ m}$, the fit is 0.5% off. At $r = r_{\text{wall}}, z = \pm 0.25 \text{ m}$, the fit is 3.6% off. Because of the axial dependence of the magnetic field, the transverse quadrupole field is approximately 12% stronger at $z = \pm 0.15 \text{ m}$ than it is at $z = 0$.

Box Coils

We designed the box shaped coils to provide a quadrupole field at $\theta_o = 45^\circ$. Using these coils in conjunction with the hexagonal coils, we produce quadrupole fields at arbitrary θ_o .

These coils are closer to the current distribution of equation 2.10 than the hexagonal coils. We constructed the coils from hollow quarter inch copper rods so that cooling water can flow through them. The box coils can have straight edges because the contribu-

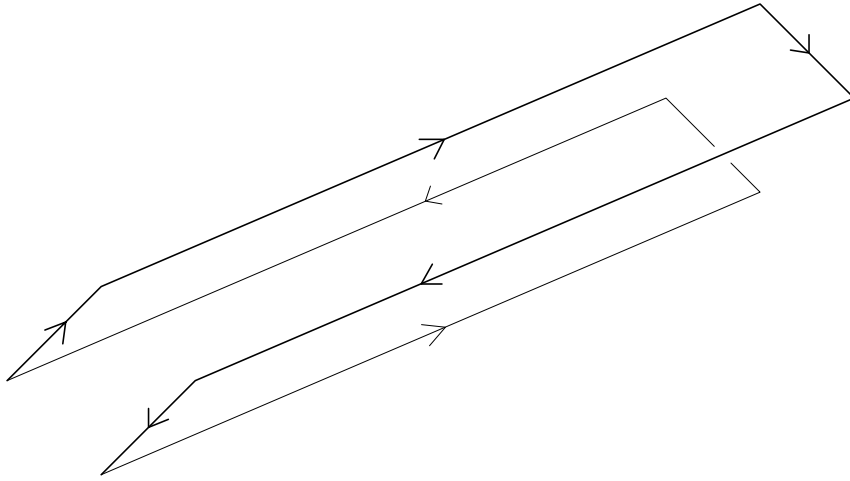


Figure 2.14: The box coils produce quadrupole fields by carrying currents as indicated by the arrows.

tions of the end pieces tend to cancel each other in the quadrupole case as opposed to the dipole field case where they add. Figure 2.14 shows the box shaped coils. In the actual system, there are four turns. The simulations show that the field produced is well represented by ψ_0 , Ψ_0 , and ψ_2 . There is a constant axial field, a magnetic mirror term, and an axially invariant quadrupole field.

$$\begin{aligned} \vec{B}_{\text{Box}} = & (y\hat{x} + x\hat{y}) \\ & + 1.32 \times 10^{-3} \hat{z} \\ & + 4.43 \times 10^{-4} [-\sinh(k_2 z)J_1(k_2 r)\hat{r} + \cosh(k_2 z)J_0(k_2 r)\hat{z}], \end{aligned} \quad (2.12)$$

where $k_2 = 9.378 \text{ m}^{-1}$, and x , and y are in meters. At $r = r_{\text{wall}}, z = 0$, the error in this fit as compared to the numerically calculated field is less than 0.1%. At $r = 0, z = \pm 0.25 \text{ m}$, the fit is 2.2% off. At $r = r_{\text{wall}}, z = \pm 0.25 \text{ m}$, the fit is 0.2% off in the transverse direction

and 2.4% off in the axial direction. Because of the small axial variation, the transverse quadrupole field varies no more than 1% from $z = 0$ to $z = \pm 0.15$ m.

Quadrupole Magnet Limits

The maximum current outputs of the power supplies limit us to a quadrupole field of 2 G/cm. Without bipolar power supplies, $0 \leq \theta_o \leq 45^\circ$. A transistor driven relay connected to one of the power supplies allows us to span the range $-45^\circ \leq \theta_o \leq 45^\circ$ to better test any dependencies on θ_o . The current rating of the relay contacts limits us to fields less than 0.1 G/cm. This is sufficient for most experiments.

Aside from the consequences of the geometry of the coils, the largest error we expect in the quadrupole field is if the quadrupole coils are offset in the transverse plane by some distance d . Since, for example, $\vec{B} = \beta(x\hat{x} - y\hat{y})$, the offset coils produce the desired quadrupole field plus a dipole field of strength βd . We account for this effect by tuning the dipole magnets while the quadrupole magnet is on. We find that there is no measurable effect down to a level equivalent to an offset of 0.3 cm. In subsequent chapters, we include only the ideal, two dimensional, quadrupole field and ignore the corrections from the shape of the coils.

Total Magnetic Field

The large axial field and the weak perturbation field combine to give the total magnetic field,

$$\vec{B} = B_z \hat{z} + \beta r (\cos[2(\theta - \theta_o)]\hat{r} - \sin[2(\theta - \theta_o)]\hat{\theta}). \quad (2.13)$$

For $\theta_o = 0$, the equations for the magnetic field lines are

$$\vec{r}(s) = x_o e^{\beta s} \hat{x} + y_o e^{-\beta s} \hat{y} + B_z s \hat{z}, \quad (2.14)$$

where s is an arbitrary parameter and $\vec{B} = d\vec{r}/ds$. Figure 2.15 shows this field pattern. A flux tube that is circular at $z = 0$ is elliptical at either end, but with the ellipses rotated by 90° with respect to one another.

2.5 Automation

To facilitate the acquisition of large time consuming data sets, we automated the experimental apparatus. The automation consists of both hardware and software compo-

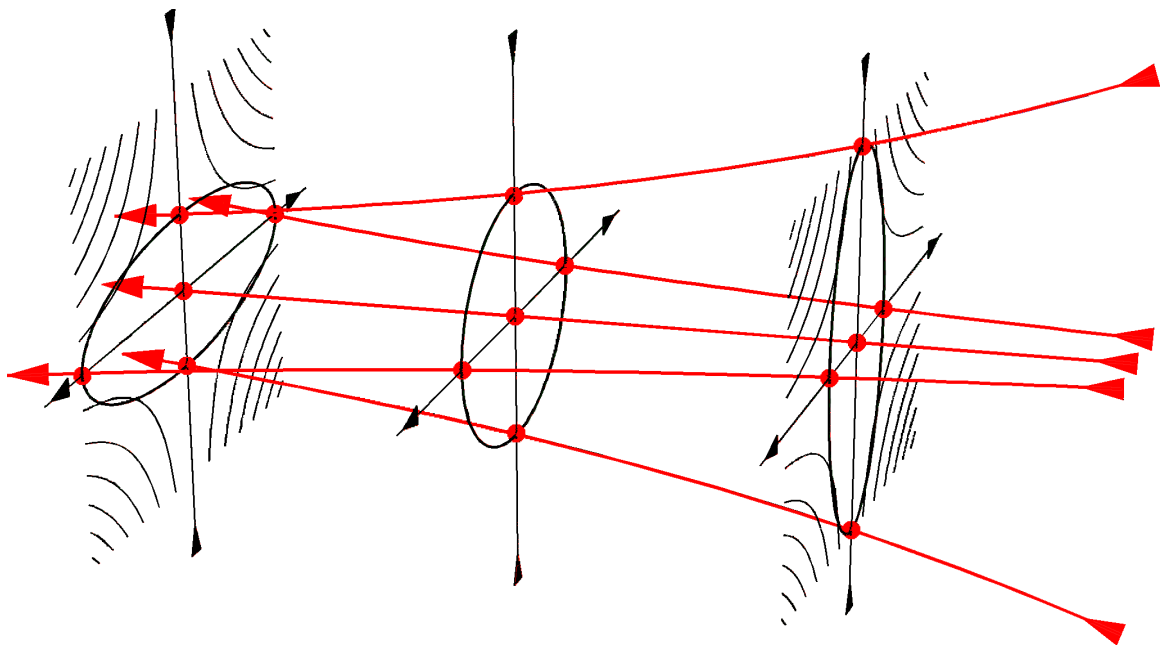


Figure 2.15: The lines with arrows show the field lines produced by adding a small, transverse, quadrupole field to a strong axial field. A flux tube that is circular at $z = 0$ is elliptical as you move away from $z = 0$. The transverse cross sections show the field lines for the transverse quadrupole field alone.

nents. The hardware includes a PC in control of magnet power supplies, a digital sequencer, arbitrary function generators, a CCD camera system and other electronics. The software is an elaborate set of LabVIEW routines.

The PC contains a National Instruments AT-AO-6 DAQ board that generates the analog and TTL signals that control the hardware. Analog signals control the voltage programmed current mode power supplies that drive the magnets. A TTL signal enables the filament bias driver. A TTL pulse from the AT-AO-6 drives the relay that selects the polarity of one of the quadrupole magnets. A series of op-amps (in a unit named PP-24) buffer the AT-AO-6 board from the power supplies, preventing dangerous ground loops that have damaged the AT-AO-6 in the past.

A digital delay (SRS-DG535) triggers the CCD camera. A 32 channel sequencer (Rohatgi Electronics SN100) that generates all of the various timing pulses for our experiments triggers the DG-535. A small, dedicated, PC controls the SN100 and our primary PC controls this PC through the RS-232 interface. A USB GPIB interface connects several devices to the PC, including the function generator used to shape the inject pulse. The length of the plasma, L , is not automated. Someone must be present to connect the right BNC cable to the right jack to choose L .

The set of LabVIEW programs exists to coordinate the automated parts of the experiment and also to analyze the data. See Appendix B for details.

Chapter 3

Plasma Shape

The quadrupole field has both radial and azimuthal components, bending the unperturbed field lines. Therefore, these quadrupole fields change the trajectories of the electrons and change the shape of the plasma. Even though the main focus of this research is the transport caused by the quadrupole magnetic field, we can make some simple predictions and perform some simple experiments on the shape of the plasma. And so before considering transport, we explore the shape of the plasma.

3.1 Introduction

3.1.1 Guiding Center Motion

In the guiding center approximation, an electron's guiding center moves freely along the magnetic field lines while drifting across them. The $\vec{\nabla}B$ and curvature drifts are in the azimuthal direction and are unimportant in our system compared to the $\vec{E} \times \vec{B}$ drift and the axial bounce motion.

$\vec{\nabla}B$ Drift

The quadrupole field strength is equal to βr so that the $\vec{\nabla}B$ drift is

$$\vec{v}_{\nabla B} = -\frac{1}{2}v_{\perp}rL\frac{\vec{B} \times \beta\hat{r}}{B_z^2}. \quad (3.1)$$

For a 1 eV electron, an axial field of 40 G and $\beta = 0.1$ G/cm, $\vec{v}_{\nabla B} = 3100$ cm/s. This is small compared to the other velocities in the system.

Curvature Drift

The curvature drift is

$$\vec{v}_{R_c} = \frac{mv_{\parallel}^2}{e} \frac{\vec{R}_c \times \vec{B}}{R_c^2 B^2}. \quad (3.2)$$

The radius of curvature is $R_c = |\vec{r}'(s) \times \vec{r}''(s)|/|\vec{r}'(s)|^3$, where $' = d/ds$. It points mostly in the radial direction although there can be a small axial component. Using equation 2.14, we find

$$R_c = \frac{\beta}{B_z} \frac{[r^2 + (B_z/\beta)^2]^{3/2}}{[r^2 + (\beta r^2/B_z \sin(2\theta))^2]^{1/2}}. \quad (3.3)$$

For a 1 eV electron at $r = 1$ cm, $B_z = 40$ G and $\beta = 0.1$ G/cm, $\vec{v}_{\text{curv}} = 16$ cm/s. This is small compared to the other velocities in the system.

3.1.2 Qualitative Discussion

With transport present, the plasma's density and shape change with time. If the characteristic transport time is greater than the other time scales in the system, then we can imagine that the plasma exists in a quasi-equilibrium state at any instant in time. It is the shape of the quasi-equilibrium plasma that we are interested in. The relevant parameter is the product of the $\vec{E} \times \vec{B}$ rotation frequency, ω_E , and the bounce time, $t_b = L/v_z$.

The quadrupole field has four-fold symmetry and so if $\omega_E t_b = \pi/2$, that is if an electron rotates 90° about the trap axis as it travels the length of the trap, then the electron is in resonance with the quadrupole field. If $\omega_E t_b \gg \pi/2$, the electron is above resonance. If $\omega_E t_b \ll \pi/2$, the electron is below resonance. The importance of the resonant electrons becomes clearer when I discuss transport in Chapter 4.

The value of $\omega_E t_b$ is not the same for all electrons, however. In general, the density of the plasma is not constant and so ω_E is a function of r . Also, there is a distribution of bounce times because of the thermal spread in velocities. The net result is that there is some spread in the values of $\omega_E t_b$ about some mean value $\overline{\omega_E t_b}$. If $\overline{\omega_E t_b} \ll 1$ (below resonance), then the plasma is spinning slowly; the electrons follow the magnetic field lines and the plasma has the shape shown in Figure 3.1. The plasma's cross section is circular in the center and elliptical at each end, but with the ellipses rotated by 90° with respect to one another. At any z , the major and minor axes of the elliptical cross section are oriented along the \hat{x} and \hat{y} directions. If $\overline{\omega_E t_b} \gg 1$ (above resonance), then the plasma is spinning relatively quickly and assumes the shape of a cylinder, as shown in Figure 3.2. The

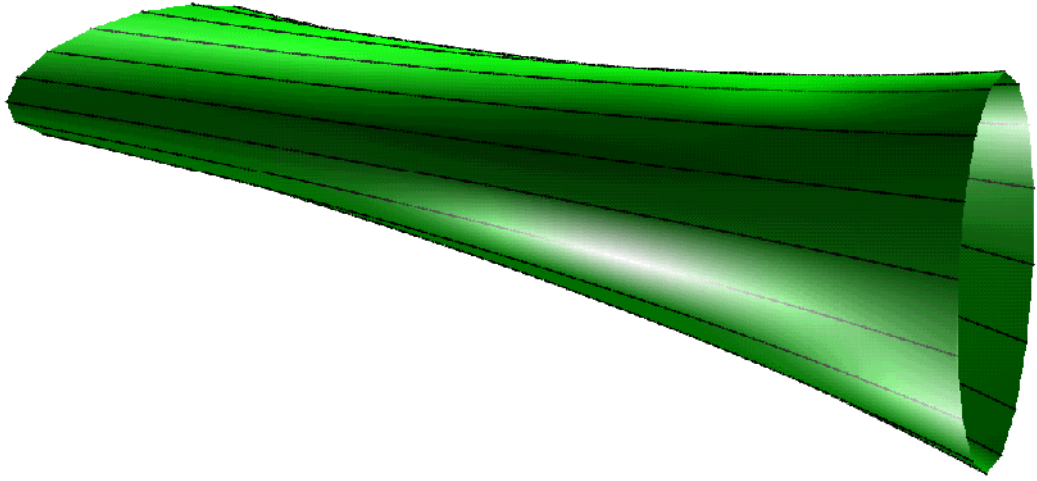


Figure 3.1: A slowly rotating plasma is elliptical.

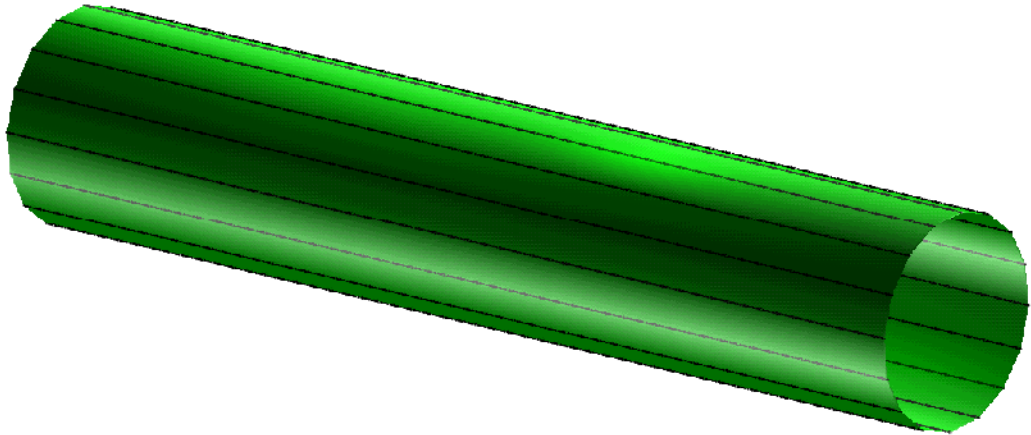


Figure 3.2: A quickly rotating plasma is cylindrical.

rapid rotation smears out any structure in the plasma. The electrons continue to follow the magnetic field lines, but the radial oscillations average out. Equations 4.16 and the resulting Poincaré section in Figure 4.4 confirm these expectations for $\omega_{Et_b} \ll 1$ and $\omega_{Et_b} \gg 1$.

A circular filament produces an elliptical plasma because individual electrons follow elliptical trajectories. Consider individual electrons that leave the filament. A Poincaré section in the x - y plane would show that an electron that leaves the filament from a point on the circumference at 12:00 o'clock or 6:00 o'clock traces out a small ellipse shown in Figure 3.3. An electron that leaves the filament from a point on the circumference at 3:00 o'clock

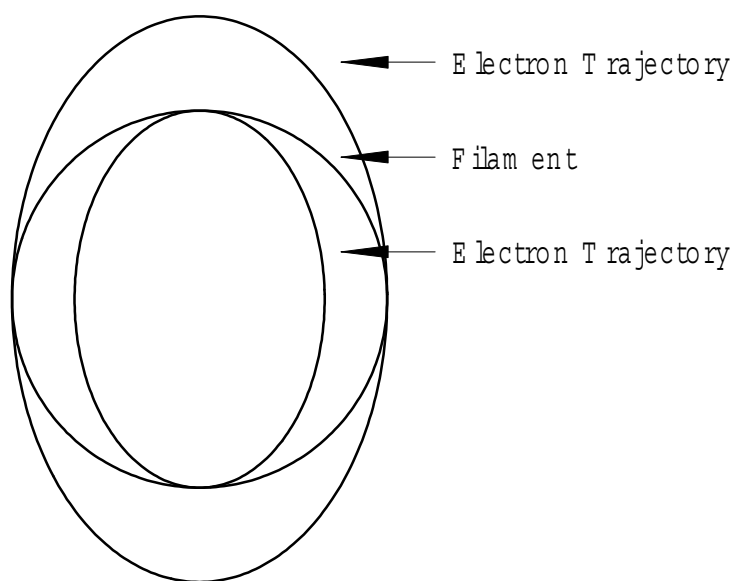


Figure 3.3: Even though a circular filament emits electrons, each electron follows an elliptical trajectory. The plasma therefore has an elliptical shape.

or 9:00 o'clock traces out a large ellipse as in Figure 3.3. Since the overall shape of the plasma is determined by the net motion of all electrons, the plasma has an elliptical shape at its ends.

There are two observations we make about the below resonance plasma that we can measure directly in experiments. First, the stronger the quadrupole field, the more elliptical the ends of the plasma are. Second, if we consider a fixed quadrupole field but successively longer plasmas, the plasma is more elliptical at the ends.

3.1.3 ϵ and θ_p from Images

Quantitative measures of the plasma's shape are the ellipticity, ϵ , and angle of an image of the plasma, θ_p . Ellipticity is the RMS length of the plasma cross section divided by the RMS width and is always greater than or equal to 1 by convention. The angle, θ_p , is the angle that the major axis of the ellipse makes with the x axis. For a plasma of uniform density whose perimeter is described by $(x/a)^2 + (y/b)^2 = 1$, the ellipticity is a/b and $\theta_p = 0$.

Even though the plasma may have a nontrivial three dimensional shape, when we image it the electrons follow the field lines on their way out of the trap. The image we record corresponds to the shape of the plasma at the end of the trap nearest to the phosphor. We confirm this by comparing the image of a long plasma with the image of the same plasma but in which only the end is dumped. The images are the same.

We measure the ellipticity and angle by calculating various moments of a plasma image. An image measures the two dimensional density distribution $n(x, y)$. Figure 3.4 shows a typical plasma image with an applied quadrupole field. We calculate the moments,

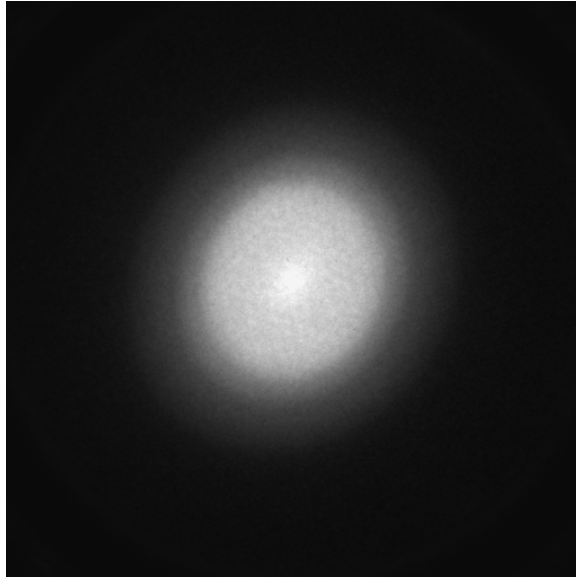


Figure 3.4: For the plasma in this image, $B_z = 400$ G , $\beta = 1$ G/cm, $\theta_p \approx \theta_o = 45^\circ$.

$$M_{xx} = \int x^2 n d^2\vec{x}$$

$$M_{yy} = \int y^2 n d^2\vec{x}$$

$$M_{xy} = \int xy n d^2 \vec{x}. \quad (3.4)$$

As the image is recorded on a CCD array on which the pixels are arranged in a cartesian grid, the moments in equation 3.4 are the natural moments to compute. However, we also define,

$$\begin{aligned} M_s &= \int r^2 \sin(2\theta) n d^2 \vec{x} \\ M_c &= \int r^2 \cos(2\theta) n d^2 \vec{x} \\ M_r &= \int r^2 n d^2 \vec{x}. \end{aligned} \quad (3.5)$$

These polar and cartesian moments are related by,

$$\begin{aligned} M_r &= M_{xx} + M_{yy} \\ M_s &= 2M_{xy} \\ M_c &= M_{xx} - M_{yy}. \end{aligned} \quad (3.6)$$

We first use these equations to find the orientation of the ellipse, θ_p . Suppose the distribution, $n(x, y)$, describes an ellipse with its major axis pointing along the x' axis which makes an angle, θ_p , with the x axis. Then $M_{s'} = 0$ by definition. So we write,

$$M_{s'} = \int r^2 \sin(2\theta - 2\theta_p) n d^2 \vec{x} = 0. \quad (3.7)$$

Simplifying the sin function gives,

$$-\sin(2\theta_p)M_c + \cos(2\theta_p)M_s = 0. \quad (3.8)$$

We now solve for the orientation angle of the ellipse in terms of the measured moments of the imaged distribution.

$$\tan(2\theta_p) = \frac{2M_{xy}}{M_{xx} - M_{yy}} \quad (3.9)$$

Note that we can express equation 3.9 in the following alternate forms that are useful below,

$$\begin{aligned} \cos(2\theta_p) &= \frac{M_{xx} - M_{yy}}{\sqrt{(M_{xx} - M_{yy})^2 + 4M_{xy}^2}} \\ \sin(2\theta_p) &= \frac{2M_{xy}}{\sqrt{(M_{xx} - M_{yy})^2 + 4M_{xy}^2}}. \end{aligned} \quad (3.10)$$

Now we proceed to compute the ellipticity, ϵ . Since ϵ is the ratio of the RMS major axis to the RMS minor axis,

$$\epsilon = \sqrt{\frac{M_{x'x'}}{M_{y'y'}}} = \sqrt{\frac{M_{r'} + M_{c'}}{M_{r'} - M_{c'}}}. \quad (3.11)$$

To write this in terms of the directly measured moments, M_{xx} , M_{yy} and M_{xy} , we first note that $M_{r'} = M_r$. Then, we reexpress $M_{c'}$ in terms of the other moments.

$$\begin{aligned} M_{c'} &= \cos(2\theta_p)M_c + \sin(2\theta_p)M_s \\ &= \cos(2\theta_p)(M_{xx} - M_{yy}) + \sin(2\theta_p)2M_{xy} \\ &= \frac{(M_{xx} - M_{yy})^2}{\sqrt{(M_{xx} - M_{yy})^2 + 4M_{xy}^2}} + \frac{4M_{xy}^2}{\sqrt{(M_{xx} - M_{yy})^2 + 4M_{xy}^2}} \\ &= \sqrt{(M_{xx} - M_{yy})^2 + 4M_{xy}^2}, \end{aligned} \quad (3.12)$$

where we have used equation 3.10. We finally write ϵ as,

$$\epsilon = \sqrt{\frac{M_{xx} + M_{yy} + \sqrt{(M_{xx} - M_{yy})^2 + 4M_{xy}^2}}{M_{xx} + M_{yy} - \sqrt{(M_{xx} - M_{yy})^2 + 4M_{xy}^2}}}. \quad (3.13)$$

This is the formula that we use to calculate ϵ from the images.

3.1.4 ϵ and θ_p from Wall Sectors

Our second measure of the shape of the plasma is the signal induced on the wall of the trap as measured by four sectors of 90° azimuthal extent each as in Figure 3.5. Since we are only interested in elliptical distortions of the plasma, we want a signal that is insensitive to $\ell = 1$ modes. The signal that we use to measure the quadrupole moment is the combination $V_Q = (V_1 + V_3) - (V_2 + V_4)$, where V_i are the voltages induced on the wall sectors. If the elliptical plasma is oriented along the x axis or the y axis, we measure a signal of one sign or the other. An elliptical plasma with $\theta_p = 45^\circ$ creates no signal. A circular plasma creates no signal. For small ellipticities, where $\epsilon \approx 1 + \delta$, V_Q is proportional to δ .

The signal V_Q measures the z averaged shape of the plasma at the axial location of the 5.14 cm long four-sectored gate. By choosing different gates as the inject gate and dump gate, we place this four-sectored gate at various axial locations in the plasma and we learn about the z dependence of the plasma shape. This technique is most useful once

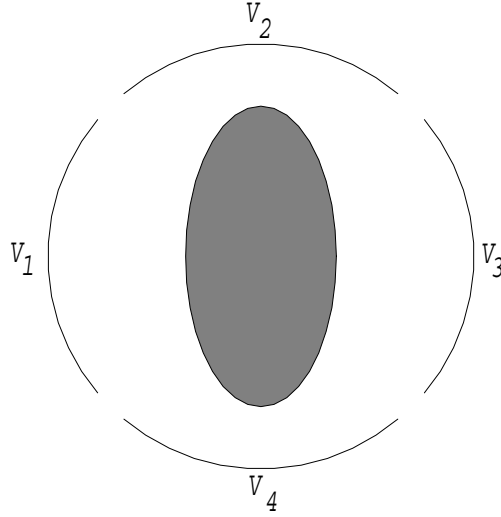


Figure 3.5: By measuring the signal $V_Q = (V_1 + V_3) - (V_2 + V_4)$, we can determine the shape of the plasma. An elliptical plasma oriented in the \hat{x} or \hat{y} direction produces a signal of one sign or the other. A plasma oriented at 45° or a circular plasma produces no signal.

images of the plasma establish that the plasma is oriented along the \hat{x} or \hat{y} directions, and not at some intermediate angle. At present, there is no good calibration between the wall signal V_Q and the CCD camera image measurement of ϵ .

3.2 Experiment, Data and Analysis

The experiments performed to measure the shape of the plasma are: imaging the plasma to measure ϵ and θ_p as functions of $\overline{\omega_{Etb}}$, using the wall sector technique to measure the ellipticity of the plasma at three axial locations within the plasma $z = \{-5 \text{ cm}, 0 \text{ cm}, 5 \text{ cm}\}$ as a function of β , and measuring the ellipticity at the end of a plasma as the length of the trapped plasma, L , increases at fixed β .

3.2.1 ϵ and θ_p from Images

There are two subtleties we must address before presenting the data. First, the plasma continues to rotate as it leaves the trap, and this means that the image may not correspond exactly to the trapped plasma's shape. The image may appear over-rotated. Second, the electric fields used to accelerate the electrons for imaging may cause distortion of the image. Note that this rotation is more severe at low B_z , where we expect the plasma

to be cylindrical. Therefore, this effect should not be too important. The radial compression does not affect the measurement of ϵ or θ_p . The extra rotation of the image may confuse the interpretation of the θ_p data however. In fact, we have no reliable way to separate the image rotation from the imaging fields from any actual rotation of the plasma.

The results shown in Figure 3.6 are for a 28 cm long plasma. We hold the plasma for 80 ms at 1000 G and scale the hold time as B_z^2 . The plasma changes from elliptical at small $\overline{\omega_E t_b}$ (large B_z) to cylindrical at large $\overline{\omega_E t_b}$ (small B_z). The angle of orientation θ_p changes from θ_o at large $\overline{\omega_E t_b}$ to $\theta_o + 90^\circ$ at low $\overline{\omega_E t_b}$. This rotation is likely due to the effects of the radial component of the imaging field. However, at large B_z , the rotation from the imaging fields is small and $\theta_p = -45^\circ$, the same as the angle of the applied quadrupole field here. The value of $\epsilon - 1$ at a given B_z is proportional to the perturbation strength, β , as expected.

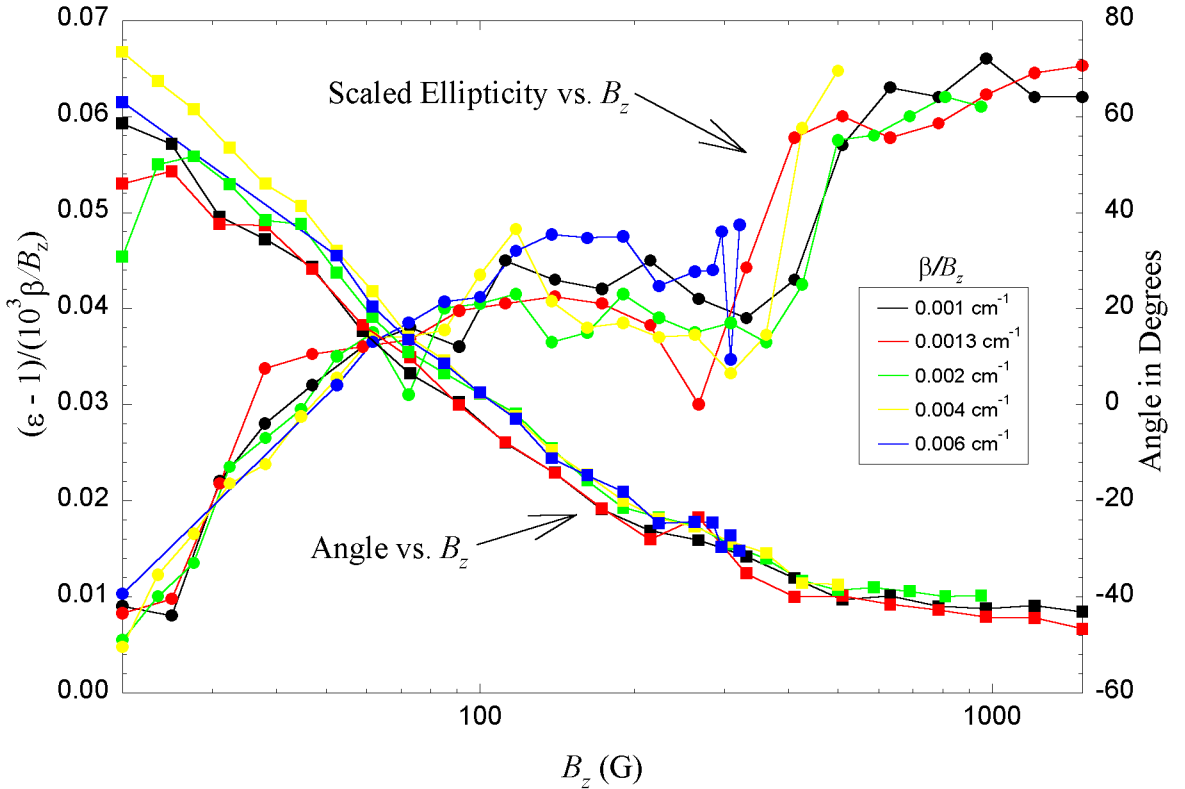


Figure 3.6: Varying B_z changes $\overline{\omega_E t_b}$. $\epsilon(B_z)$ shows the expected behavior; the plasma is circular at low B_z and elliptical at high B_z and $\epsilon - 1$ is proportional to β . The change in $\theta_p(B_z)$ is likely due to imaging fields. At large B_z , $\theta_p \approx \theta_o$.

3.2.2 ϵ and θ_p from Wall Sectors

To measure ϵ and θ_p from the wall sectors, we first fine tune the capacitance to ground and resistance to ground of the wall sectors. Even though the four sectors are identical as far as the plasma is concerned, each sector has its own connecting wires and thus its own capacitance and resistance to ground. We add variable capacitors and resistors and adjust their values so that a symmetric test signal gives no output signal, V_Q . The test signal is capacitively coupled so that it mimics the presence of a plasma in the trap. Figure 3.7 shows the circuit we use to tune the capacitance and resistance.

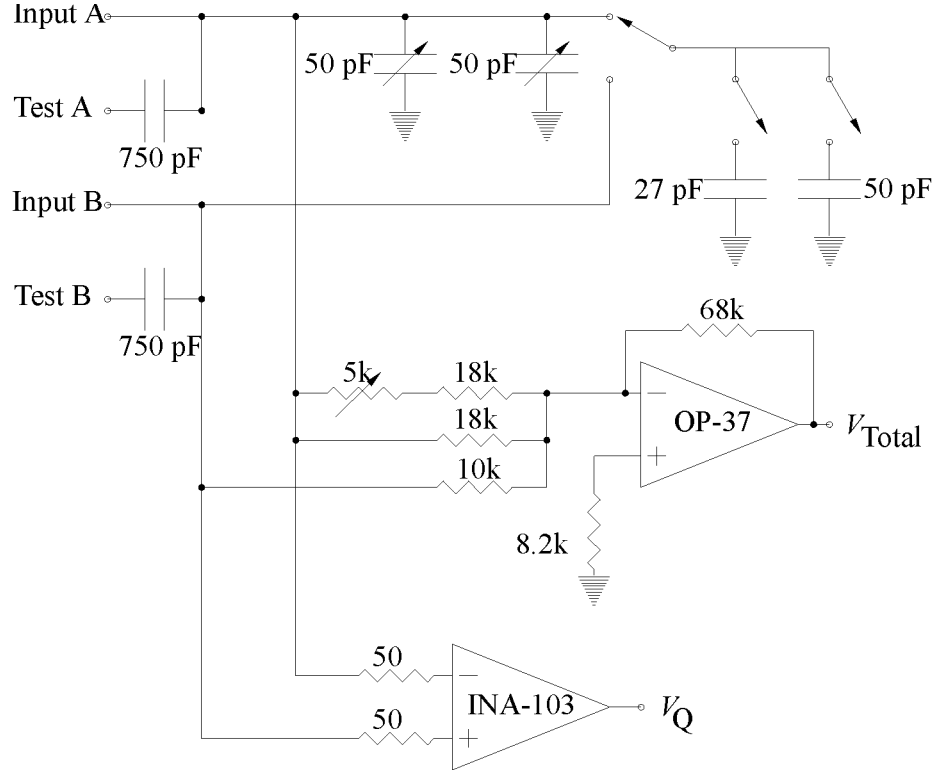


Figure 3.7: We connect the top and bottom sectors to Input A and the left and right sectors to Input B. We adjust the capacitance and the resistance until a test signal applied to both Test A and Test B simultaneously gives no output signal $V_Q = (V_1 + V_3) - (V_2 + V_4)$. We use an INA-103 instrumentation amplifier to generate the signal V_Q and an OP-37 to generate the total signal $V_{Total} = V_1 + V_2 + V_3 + V_4$.

If we choose the four-sectored gate to be the first gate after the inject gate, then we are measuring ϵ at the end of the plasma. Given the arrangement of the gates inside the machine, possible plasma lengths are approximately 19, 11, 7 and 3 cm when the

four-sectored gate is at the end. Figure 3.8 shows that $\epsilon - 1$ at the end of the plasma is

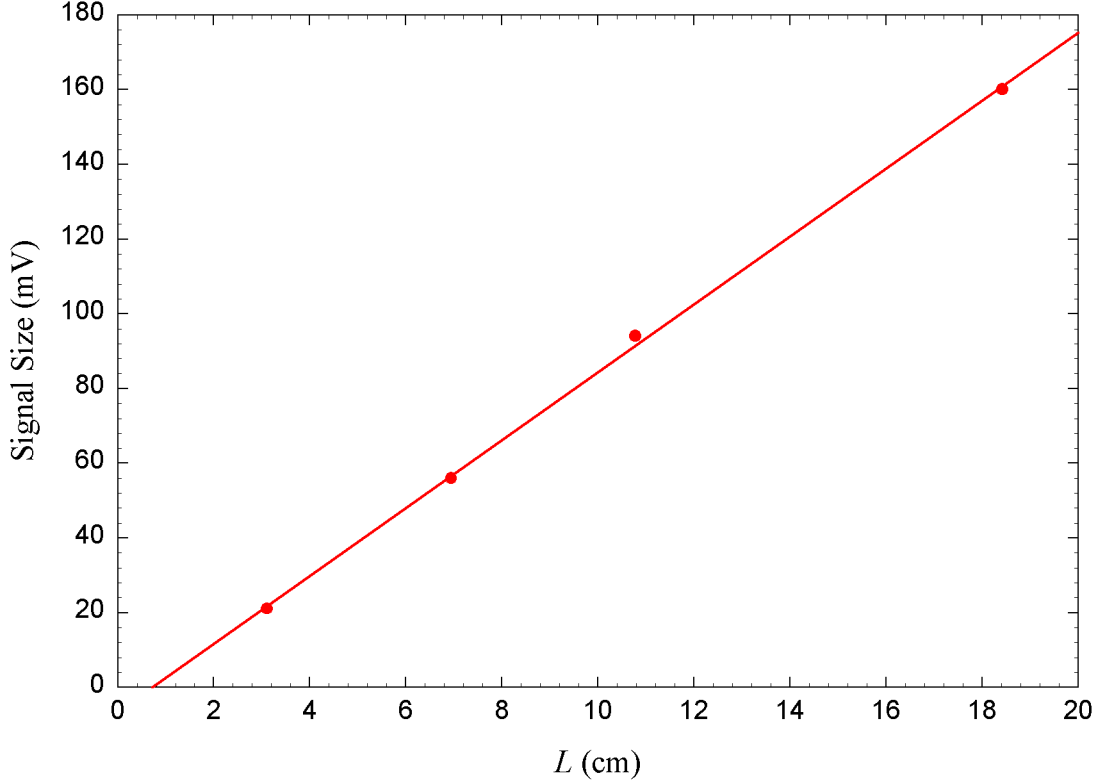


Figure 3.8: The ellipticity at the end of a plasma measured by V_Q is proportional to the length of the trapped plasma.

proportional to L when β is fixed. Because of the short length of some of the plasmas used in this measurement, they are below resonance plasmas. For the shorter lengths used, above resonance plasmas are not accessible in the machine and so we make no measurement. We would expect a regime where $\epsilon \approx 1$, independent of L .

By varying the angle, θ_o , of the applied quadrupole, the signal should change sinusoidally. The data in Figure 3.9 confirm this. Camera images also show that θ_p follows the angle of the applied quadrupole.

As described above, we choose different inject and dump gates so that the four-sectored gate is at the z location we want. One drawback of this method is that we cannot do this for full length plasmas. And it is only for full length plasmas that we can have above resonance plasmas. Therefore, we cannot test the axial invariance of the above resonance plasma's shape. Thus, we only measure ϵ versus z in the below resonance regime. Note

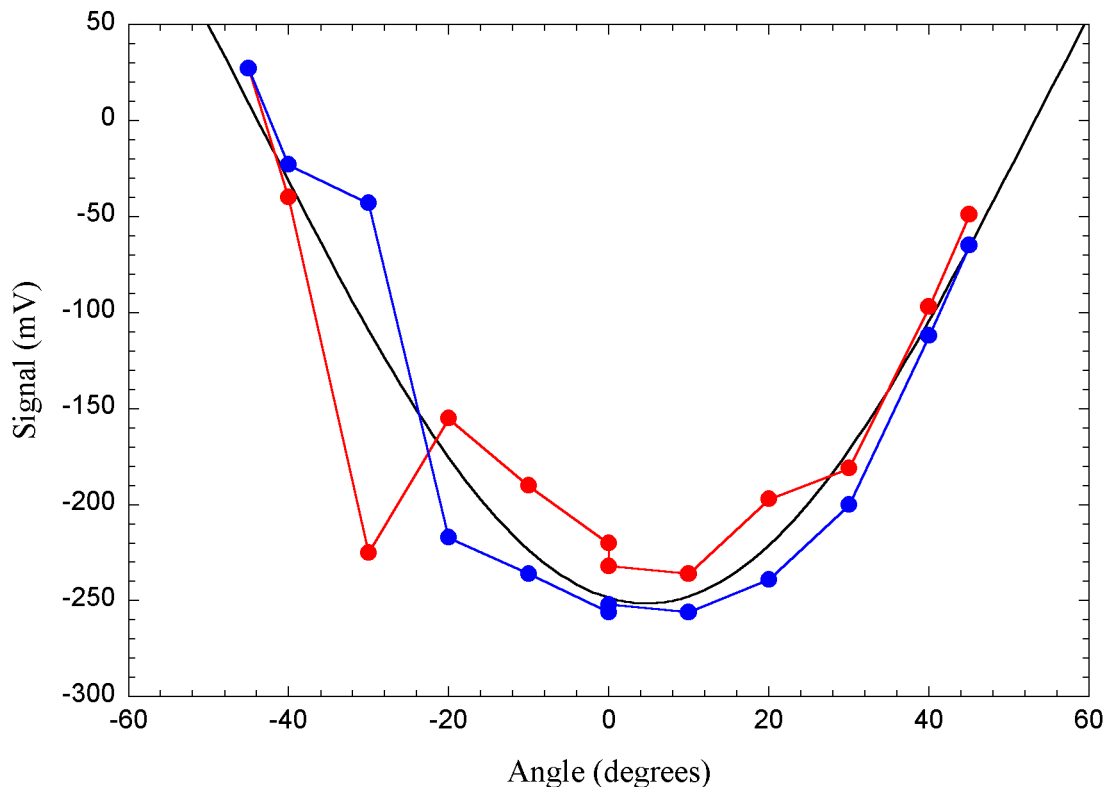


Figure 3.9: Varying the angle of the applied quadrupole field rotates the plasma and reduces the measured signal on the four-sectored gate. The two data sets refer to two separate features of the oscilloscope trace used to measure the effect. The solid line is a least squares fit to $a \cos[2\pi(\theta - \theta_o)/b]$ giving $a = -251$ mV, $\theta_o = 4.6^\circ$, and $b = 194^\circ$. These compare favorably with the expected values of $\theta_o = 0$ and $b = 180^\circ$.

that the $z = 0$ measurement is made on a longer plasma (15.4 cm) than the measurements made at the ends of the plasma (± 10.3 cm). This is by necessity of the gate arrangement. Figure 3.10 shows that, as expected, $\epsilon - 1$ is equal and opposite at $\pm z_o$, is 0 at $z = 0$ and proportional to β .

3.3 Summary

These experiments give us an understanding of the most obvious effects of the quadrupole field, the effect of the quadrupole field on the shape of the plasma. The previously uniform axial field, $B_z \hat{z}$, now has the shape described by equation 2.13 when we apply the quadrupole field. The flux tubes become twisted bowties.

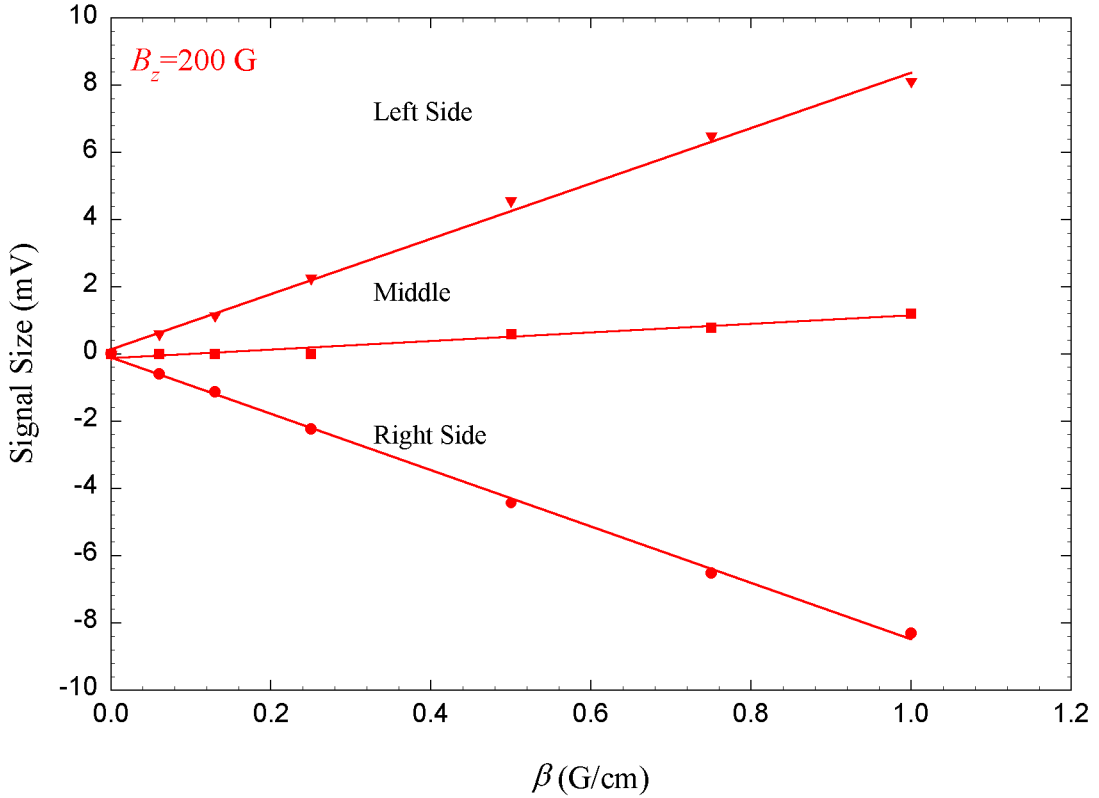


Figure 3.10: Placing the pickup gate at different axial positions allows us to measure the relative ellipticity at the left, middle, and right of the plasma. We see that $V_Q = 0$ in the center of the plasma, while V_Q is equal and opposite at the ends of the plasma.

Measurements with both the CCD camera and the wall sectors show that when $\overline{\omega_{Etb}} \gg 1$ (above resonance), the rotation of the plasma column is fast compared to the bounce motion and the plasma is cylindrical. The radial oscillations of the electrons average out. When $\overline{\omega_{Etb}} \ll 1$ (below resonance), the plasma rotates slowly and assumes the shape of the magnetic field lines.

The below resonance plasma has all the properties we expect of a plasma that has the same shape as a magnetic flux tube. At the center of the plasma, the plasma's cross section is circular. The ellipticity is equal and opposite at each end of the plasma and this ellipticity is proportional to the length of the plasma and to the quadrupole field strength. The angle of orientation of the plasma is the same as the angle of the applied quadrupole field. We attribute the rotation of the plasma images at low B_z to the effects of the imaging electric field.

Chapter 4

Transport

4.1 Theory

The addition of the quadrupole field causes the trajectories of individual electrons' guiding centers to have radial components. Within a simplified model, we can find these trajectories analytically. Small collisions, however, can knock electrons from one trajectory to another. Therefore, we envision the effect of the quadrupole field to be a diffusion process. We use the analytical trajectories to find an estimate of the step size, λ , we postulate a collision frequency, ν , and form a diffusion coefficient, $D = \lambda^2 \nu f$, where f is the fraction of electrons participating in the diffusion.

4.1.1 Qualitative Discussion

We can guess what the trajectories look like by considering a few examples of specific electrons. Consider the resonant electron in Figure 4.1 that starts at 45° below the x axis and that rotates about the trap axis by 90° during the time it takes to travel the length of the trap. This electron is on field lines with radial components directed radially outwards and thus the electron moves to a larger radial position than it started at. Now consider the return trip back across the length of the trap. Again, the electron is on field lines with radial components directed outwards. This particular electron, with its certain initial angle, and its certain value of $\omega_E t_b$, is on a trajectory that takes it ever outwards. If the resonant electron with $\omega_E t_b = \pi/2$ begins at 45° above the x axis instead of 45° below, the same argument shows that the electron moves ever inwards. If this electron begins at

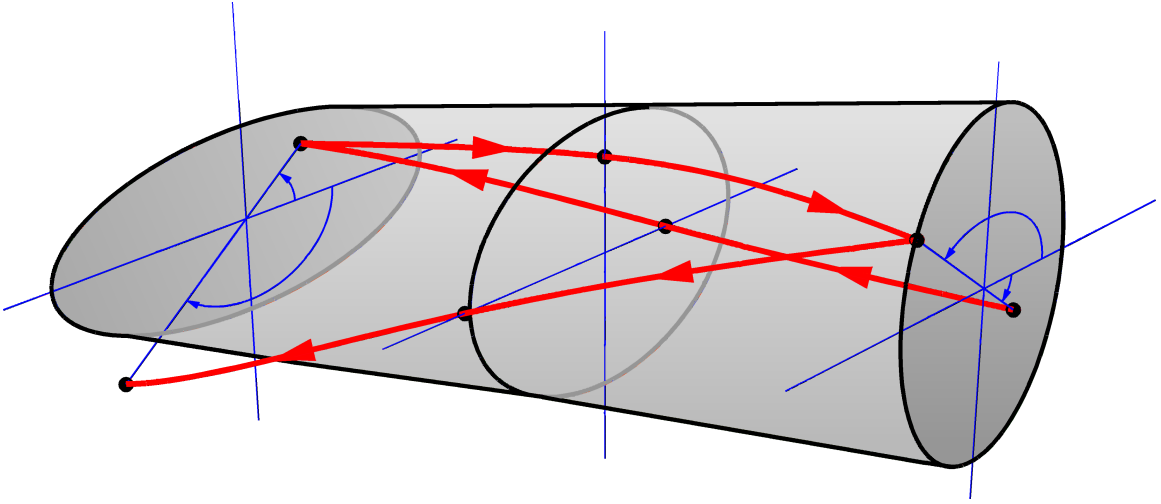


Figure 4.1: An electron that begins 45° below the x axis and rotates by 90° as it travels the length of the trap is resonant and moves ever outwards.

$\theta = 0$, then as it travels across the length of the trap, it moves outwards during the first half of the traversal and inwards during the second half. The result is that there is no net radial displacement. Depending on the initial angle, the resonant electron may move either outwards or inwards.

If the electron does not exactly meet the resonance condition $\omega_E t_b = \pi/2$, then as it travels across the length of the trap it will always see field lines with radial components directed both outwards and inwards. The result of this motion is a reduction in the radial excursion as compared to the resonant electron. If off resonance, the electron experiences radial oscillations. If the electron is too far above resonance, then in one traversal of the trap the radial excursions average out over θ . If the electron is too far below resonance, it simply bounces back and forth along a field line. And even though this field line may take the electron from a small radius at one end to a large radius on the other end, the radial excursion averages out over z .

There are higher order resonances as well. If the electron has $\omega_E t_b = N\pi/2$, where N is an odd integer, then the electron that begins 45° below the x axis sees field lines with a net radial component as it travels across the length of the trap. If N is even, the outwards motion and inwards motion cancel out. As with the primary resonance, these higher order resonances cause the electrons to move either outwards or inwards depending on the initial angle of the electrons.

4.1.2 Quantitative Discussion

Let us now consider the situation more quantitatively. If the guiding center of an electron follows a magnetic field line, then

$$\frac{1}{v_z} \frac{dr}{dt} = \frac{B_r}{B_z}. \quad (4.1)$$

The radial magnetic field is from the expression for the quadrupole field in polar coordinates,

$$\vec{B}_{\text{Quadrupole}} = \beta r [\cos(2\theta)\hat{r} - \sin(2\theta)\hat{\theta}]. \quad (4.2)$$

Substituting the expression for B_r into equation 4.1 we obtain,

$$\frac{dr}{dt} = v_z \frac{\beta r \cos(2\theta(t))}{B_z}. \quad (4.3)$$

We integrate this expression to solve for $\ln r$.

$$\ln r = \frac{v_z \beta}{B_z} \int \cos(2\theta(t)) dt. \quad (4.4)$$

Exponentiating gives,

$$r = R \exp \left[\frac{v_z \beta}{B_z} \int_0^t \cos(2\theta(t')) dt' \right], \quad (4.5)$$

where R is the electron's initial radius and $\theta(t) = \theta_o + \omega_E t$. Hereafter, we drop the subscript E from ω_E because we wish to give ω other subscripts.

For the N^{th} order resonance, $\omega = (N\pi/2)(v_z/L)$. We denote these resonant frequencies by ω_N , and define the departure from resonance, $\Delta\omega_N$, for those electrons that do not exactly meet the resonance condition via,

$$\theta(t) = \theta_o + (\omega_N + \Delta\omega_N)t. \quad (4.6)$$

Then,

$$r = R \exp \left[\frac{v_z \beta}{B_z} \int_0^t \cos(2\theta_o + 2(\omega_N + \Delta\omega_N)t') dt' \right]. \quad (4.7)$$

We assume that $\Delta\omega_N \ll \omega_N$ and average over the fast oscillation of frequency ω_N . Although it is not obvious, this averaging removes the complication associated with v_z changing sign after an electron bounces from the end of the trap. Let $I(t) = \int_0^t \cos(2\theta_o + 2(\omega_N + \Delta\omega_N)t') dt'$. Then note that $\omega_N t$ is ϕ_N , the angle of rotation for the N^{th} resonance. So,

$$\begin{aligned} \langle I(t) \rangle &= \frac{2}{N\pi} \int_0^t \int_0^{\frac{N\pi}{2}} \cos(2\theta_o + 2\phi_N + 2\Delta\omega_N t') d\phi_N dt' \\ &= \frac{1}{N\pi} \int_0^t [\sin(2\theta_o + 2\Delta\omega_N t' + N\pi) - \sin(2\theta_o + 2\Delta\omega_N t')] dt' \\ &= \frac{1}{N\pi} \int_0^t -2 \sin(2\theta_o + 2\Delta\omega_N t') dt', \end{aligned} \quad (4.8)$$

where N is odd. Evaluating the t' integral yields,

$$\langle I(t) \rangle = \frac{1}{N\pi\Delta\omega_N} \left[\cos(2\theta_o + 2\Delta\omega_N t) - \cos(2\theta_o) \right]. \quad (4.9)$$

Using this in equation 4.7 gives,

$$r = R \exp \left[\frac{|v_z|\beta}{B_z N \pi} \frac{\cos(2\theta_o + 2\Delta\omega_N t) - \cos(2\theta_o)}{\Delta\omega_N} \right]. \quad (4.10)$$

As argued above, the electron with the largest radial excursion is the one with $\theta_o = -\pi/4$. We set $\theta_o = -\pi/4$ and assume that the quadrupole field is weak enough so that the argument of the exponential is small and we expand the exponential to find the step size, λ_N .

$$\lambda_N = R \left[\frac{|v_z|\beta}{B_z N \pi} \frac{\sin(2\Delta\omega_N t)}{\Delta\omega_N} \right] \quad (4.11)$$

The electron follows this trajectory until it suffers a collision, so we substitute $1/\nu$ for t . As long as $\Delta\omega_N t \ll 1$, then

$$\lambda_N = \frac{2R|v_z|\beta}{B_z N \pi \nu}. \quad (4.12)$$

Below, we estimate ν^{-1} to be approximately $15 \mu\text{s}$. If we choose typical parameters such as $R = 1 \text{ cm}$, $v_z = 4.2 \times 10^7 \text{ cm/s}$, $\beta = 0.02 \text{ G/cm}$ and $B_z = 100 \text{ G}$, then $\lambda_1 = 0.04 \text{ cm}$.

To determine the width of the resonance, $\Delta\omega_N$, in ω space we note that equation 4.10 is an oscillatory function as in Figure 4.2. We choose $\Delta\omega_N$ such that $t = 1/\nu$ corresponds to the first maximum of this function. That is, choose $\Delta\omega_N$ so that

$$\Delta\omega_N = \frac{\pi\nu}{4}. \quad (4.13)$$

This expression means that the extra angle of rotation, $\Delta\phi_N = \Delta\omega_N/\nu$, before a collision should be no greater than $\pi/4$. Figure 4.2 shows that this choice of $\Delta\omega_N$ selects trajectories that have similar radial excursions to the resonant electron. If we use $\nu^{-1} = 15 \mu\text{s}$, then $\Delta\omega_1 = 5.2 \times 10^4 \text{ rad s}^{-1}$.

We construct the diffusion coefficient by writing, $D_N = \lambda_N^2 \nu f$, where the fraction of electrons participating in the diffusion is

$$f = \sqrt{\frac{m}{2\pi kT}} \exp \left(\frac{-v_z^2}{2v_{\text{th}}^2} \right) \Delta v_z, \quad (4.14)$$

where $v_{\text{th}} = \sqrt{kT/m}$ and Δv_z is the width of the resonance in velocity space. Since $\omega_N = (N\pi/2)(v_z/L)$, we can write $\Delta\omega_N/\omega_N = \Delta v_z/v_z$, or $\Delta v_z = L\nu/2N$. If we use

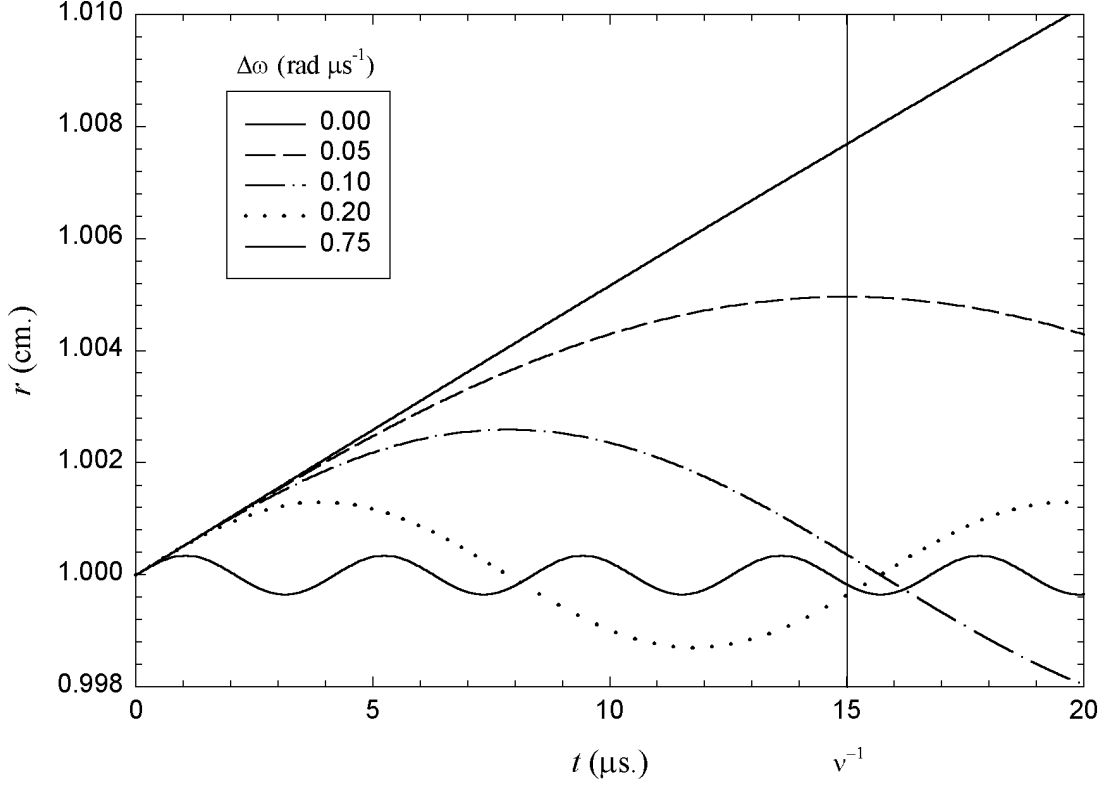


Figure 4.2: A plot of equation 4.10. An electron exactly in resonance has an exponential trajectory. As the electron is further off resonance, the radial oscillations become smaller in magnitude and increased in frequency. We choose $\Delta\omega_N$ such that trajectory reaches its first maximum at $1/\nu$. In this Figure, $\beta = 0.02$ G/cm, $B_z = 200$ G, $L = 28$ cm, $\omega = 4.5 \times 10^5$ rad s^{-1} .

$v_z = v_{th} = 4.2 \times 10^7$ cm/s, $L = 28$ cm and $\nu^{-1} = 15$ μs , then $\Delta v_z = 9.3 \times 10^5$ cm/s and $f = 5.4 \times 10^{-3}$.

Up until this point, we have considered an electron with a given velocity, v_z , and determined the resonant angular frequency ω_N in terms of v_z . In our experiment, we calculate ω from $n(r)$ and we only have knowledge of the average velocity v_{th} . Therefore, it is more natural to write $v_N = 2\omega L/N\pi$ and substitute this formula for v_N for $|v_z|$ to write diffusion as a function of ω . Putting this all together gives,

$$D_N = \left(\frac{4R\omega L\beta}{B_z N^2 \pi^2 \nu} \right)^2 \nu \sqrt{\frac{m}{2\pi kT}} \exp\left(-\frac{\omega^2}{2\omega_{th}^2}\right) \frac{L\nu}{2N}$$

$$= \frac{8R^2\omega^2L^3\beta^2}{B_z^2N^5\pi^4} \sqrt{\frac{m}{2\pi kT}} \exp\left(-\frac{\omega^2}{2\omega_{\text{th}}^2}\right), \quad (4.15)$$

where $\omega_{\text{th}} \equiv N\pi v_{\text{th}}/2L$.

We plot $D_1(\omega)$ in Figure 4.3. We may describe the resonant behavior of $D(\omega)$ qualitatively. At large ω , the plasma is rotating relatively quickly, and so for an electron to be resonant it must have a relatively large v_z . But the Maxwellian distribution ensures that there are few electrons moving very fast. The diffusion is suppressed. At small ω , there are plenty of resonant electrons in the thermal distribution, but now the step size is small. Again, diffusion is suppressed. Summing over odd N gives the total diffusion we expect

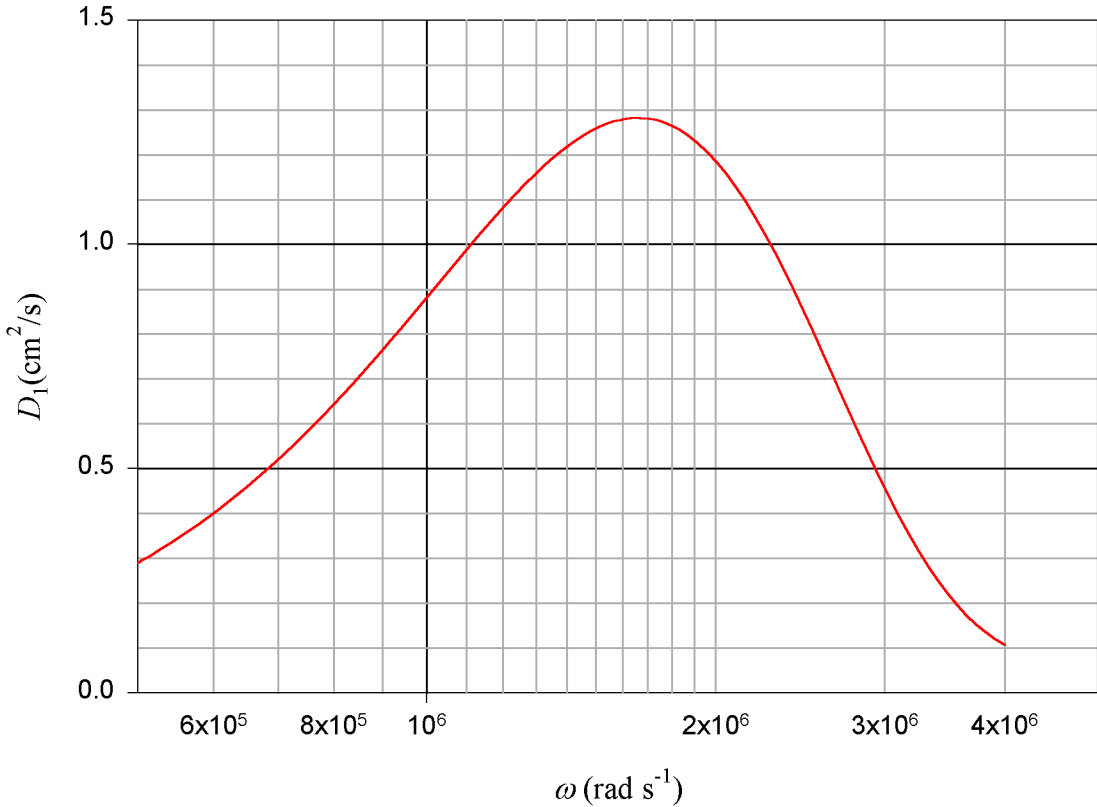


Figure 4.3: The resonance is clearly shown in this graph of $D_1(\omega)$. Here, $B_z = 100$ G, $L = 28.2$ cm, $r = 0.95$ cm, $\beta = 0.02$ G/cm, and $kT = 0.25$ eV.

from this model. Several features are noteworthy.

That the collision frequency, ν , canceled out of our calculation is characteristic of diffusion in the so called “plateau” regime. In this regime, there are frequent collisions and diffusion typically scales like δ^2 , where δ is the perturbation strength. In the so called

“banana” regime, there are infrequent collisions and diffusion scales like $\delta^{1/2}\nu$ where the collision frequency appears explicitly. The 90° collision time, ν_{90}^{-1} , is approximately 3 ms in our system if we use the Spitzer formula for ν_{90} . But using ν_{90} grossly underestimates ν because a change in angle of much less than 90° will knock an electron off of resonance. The ratio $\Delta v_{90}/v \approx 1$ for a 90° collision, but $\Delta v/v = \pi\nu/4\omega$ defines a collision in our case. Collisions are a random walk process, so the mean squared excursion in velocity space is proportional to time, thus $\Delta v_{90}^2/\Delta v^2 = \nu/\nu_{90}$. Solving for ν , yields $\nu = (16\omega^2\nu_{90}/\pi^2)^{1/3}$. For $\omega = 10^6$ rad s $^{-1}$, $\nu^{-1} \approx 15$ μ s, which is short enough to ensure that we are in a collisional regime for all axial fields accessible in our experiment. It is appropriate to work in the plateau regime.

Because of the N^{-5} dependence, D is well approximated by D_1 . The function $D_1(\omega)$ has a maximum at $\omega_{\text{res}} = \sqrt{2}\omega_{\text{th}}$. Therefore, the height of the peak scales like $\omega^2 \exp(-\omega^2/2\omega_{\text{th}}^2)|_{\sqrt{2}\omega_{\text{res}}} \propto \omega_{\text{th}}^2$. This makes the overall L scaling of the peak $L^3\omega_{\text{th}}^2 \propto L$, and the overall kT scaling $\omega_{\text{th}}^2/\sqrt{kT} \propto \sqrt{kT}$.

Let us further consider the scalings predicted by the expression for D . When the argument of the exponential is small, the exponential term is close to unity. The argument will be small if $\omega/\omega_{\text{th}} \ll 1$ and the plasma is below resonance. In this regime, $D \propto (\beta R\omega/B_z)^2 L^3$. To compare this scaling to the scalings of other models, we imagine two circumstances. First, imagine that only B_z and L may vary; the electric field is fixed and $\omega \propto 1/B_z$ and D scales like L^3/B_z^4 , in contrast to the usual L^2/B_z^2 that is attributed to resonant particle transport [15]. Second, imagine further that β/B_z is constant as well, as would be the case if the quadrupole field perturbation came from asymmetries in the solenoidal magnet; the scaling is L^3/B_z^2 , which is also different than the usual L^2/B_z^2 scaling.

The L^2/B_z^2 scaling comes from considering the diffusion to be a bounce resonant effect. We expect that for a bounce resonant effect ω_E and t_b should enter in the combination $\omega_E t_b \propto L/B_z$ and since $[D] = \text{m}^2/\text{s}$ it must be L^2/B_z^2 . However, this argument makes no reference to any specific mechanism. In our model, the extra power of L that makes the overall dependence L^3 comes from f (see equation 4.14), since $\Delta v_z \propto L$.

There are many simplifying assumptions in our model. Assumptions that we can justify are the constancy of v_z and the neglect of the quadrupole field’s contribution to ω . Conservation of energy dictates that $v_z = dz/dt$ varies with radius. Also, the equation for $d\theta/dt$ contains a term from the azimuthal component of the quadrupole field. For a

constant density plasma, the full set of equations for r , θ and z is,

$$\begin{aligned}\frac{dr}{dt} &= \sqrt{\frac{2E}{m} + \frac{\omega_p^2}{2}r^2} \frac{\beta r \cos(2\theta(t))}{B_z} \\ \frac{d\theta}{dt} &= \omega_E - \sqrt{\frac{2E}{m} + \frac{\omega_p^2}{2}r^2} \frac{\beta \sin(2\theta(t))}{B_z} \\ \frac{dz}{dt} &= \sqrt{\frac{2E}{m} + \frac{\omega_p^2}{2}r^2},\end{aligned}\tag{4.16}$$

where $E = \frac{1}{2}mv_z^2 - e\phi$ and $\phi = m\omega_p^2 r^2/4e$ is the potential of a constant density plasma. This set of coupled differential equations describes the motion of the electron's guiding center if we include a change in sign for the square roots each time the electron reaches the end of the plasma. We find, numerically, that $\theta(t)$ is not greatly modified from $\theta(t) = \theta_o + \omega_E t$ by the quadrupole field.

In our qualitative picture of resonant particles, the resonant electrons are lost to the wall quickly. By adding energy conservation, the resonant electrons become nonresonant as they move radially outwards. The result is that the electron undergoes a radial oscillation. We solve the set of coupled differential equations numerically and create a Poincaré section at the end of the plasma. We keep the parameters E , ω_p , β and B_z fixed and only vary the initial conditions $r(0)$ and $\theta(0)$.

The Poincaré section in Figure 4.4 shows the three different types of particle orbits: above resonance, resonant, and below resonance. By keeping E fixed, the electrons at small radii have small v_z , implying that $\omega_E t_b \gg 1$. At large radii, the electrons have a large v_z , implying that $\omega_E t_b \ll 1$. The shape of the orbits at small radii are nearly circular while the orbits at large radii are elliptical. For intermediate radii, where the electrons have axial velocities such that $\omega_E t_b \approx \pi/2$ the trajectories become banana shaped islands.

Figure 4.5 compares equation 4.10 with a numerical solution of equation 4.7 and the full set of coupled differential equations in equation 4.16 for a set of realistic parameters. We find that the averaging over the fast oscillations is valid. Moreover, for times less than $\sim \nu^{-1}$, our model is a fair approximation of the full set of coupled differential equations. The latter conclusion is somewhat weaker at larger β/B_z , $r(0)$ or n , where our model might only be a fair approximation of the full set of differential equations for times less than $\sim \frac{1}{3}\nu^{-1}$.

Aside from assuming that v_z and ω are constant, what are other limitations of our model? The axial and radial variations of the plasma density and temperature complicate

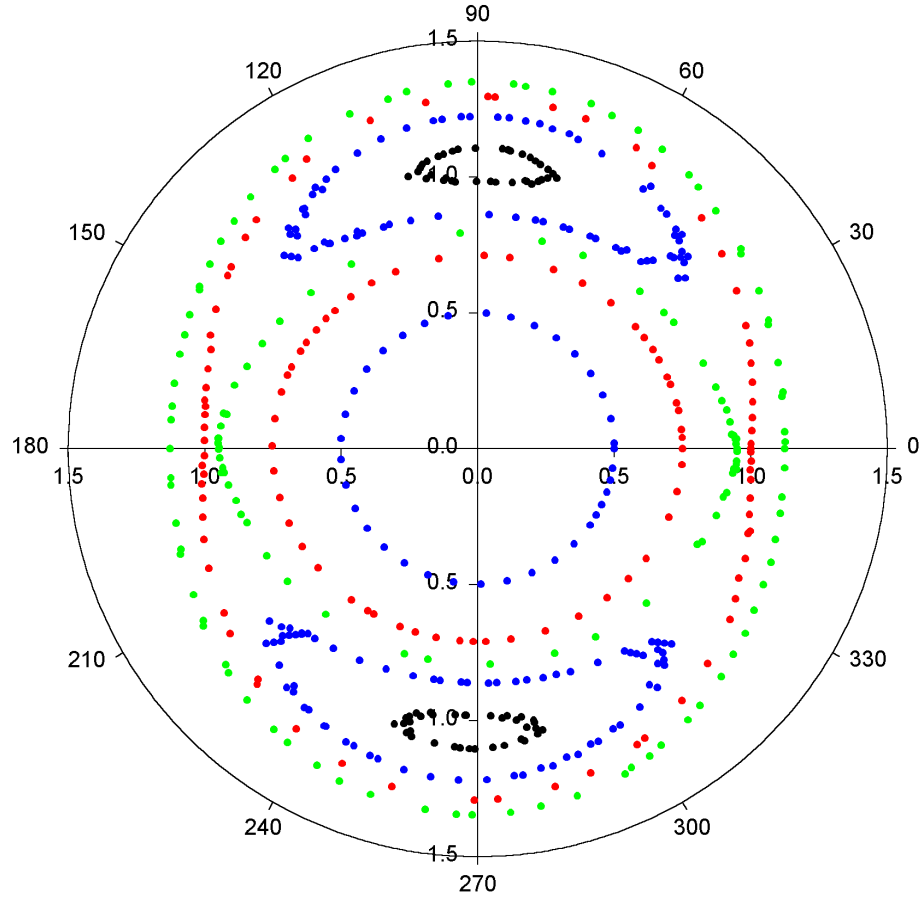


Figure 4.4: Poincaré sections showing electrons with constant E . $B_z = 40$ G, $\beta = 0.1$ G/cm, $L = 28$ cm, and $n = 10^6$ cm $^{-3}$ here. At small radii, we have $\omega_E t_b \gg 1$ and the orbits are nearly circular. At large radii, we have $\omega_E t_b \ll 1$ and the orbits are elliptical. For $\omega_E t_b \approx \pi/2$ we have the islands. Not visible are smaller islands corresponding to the higher order resonances at still smaller radii.

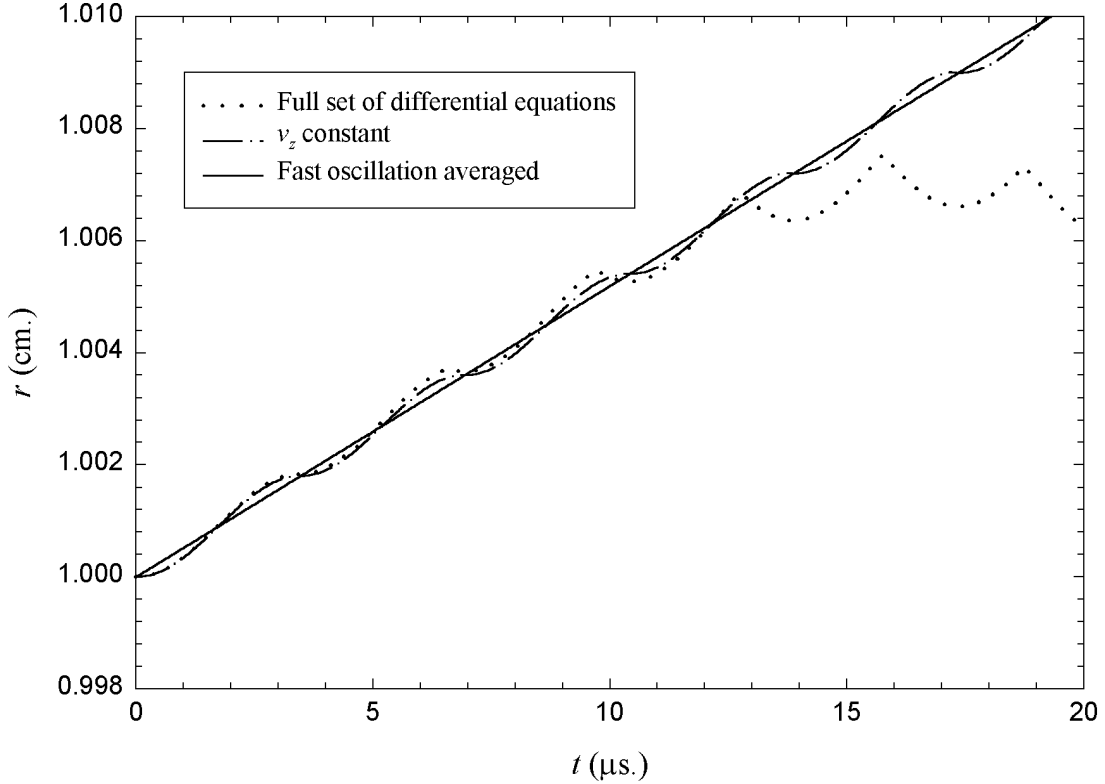


Figure 4.5: A comparison of the numerical solution and the averaged, analytic, solution for $\theta_o = -45^\circ$ shows that averaging is effective. $B_z = 200$ G, $\beta = 0.02$ G/cm, $L = 28$ cm, $n = 10^6$ cm $^{-3}$ and v_z is such that this is a resonant electron.

things. A plasma with nonuniform density will not have a constant ω_E . If there is a temperature gradient, then t_b will vary. Moreover, the effective length of the plasma changes with temperature and density. If we are not in a collisional regime, then we are in a banana regime and the derivation of D we present here is no longer valid. There are other transport processes present that try to flatten out the density distribution once the quadrupole field creates density gradients and it may be that the interaction of the two effects produces transport that is different from what we predict. Mobility or other nondiffusive processes which would interfere with diffusion measurements could be present.

4.2 Experiment

4.2.1 Measuring Diffusion

Our tool for measuring D is the CCD camera. For the small β used in the diffusion experiments, even below resonance plasmas are nearly cylindrical. Imaging these plasmas gives $n(r, \theta, t)$ where there is practically no θ dependence. Therefore, we average over θ in the subsequent analysis and treat the camera images as measurements of $n(r, t)$.

To measure D from $n(r, t)$, we begin by considering the continuity equation,

$$\frac{\partial n}{\partial t} = -\vec{\nabla} \cdot \vec{\Gamma}, \quad (4.17)$$

where $\vec{\Gamma}$ is the flux of electrons. We multiply both sides of equation 4.17 by $2\pi r$ and integrate from $r = 0$ to some arbitrary radius $r = R$ and make the identification

$$N(t) = \int_0^R n(r, t) 2\pi r dr \quad (4.18)$$

as the number per unit length within the radius R . We get,

$$\frac{dN}{dt} = -2\pi R \Gamma_r(R). \quad (4.19)$$

Thus,

$$\Gamma_r = -\frac{dN/dt}{2\pi R}. \quad (4.20)$$

To measure D , we must make some assumption about the form of Γ . The simplest assumption is Fick's Law, where $\vec{\Gamma} = -D\vec{\nabla}n$. This gives

$$D = \frac{dN/dt}{2\pi R dn/dr|_{r=R}}. \quad (4.21)$$

We created LabVIEW routines to automate the data collection process. The outline of the data acquisition process is as follows:

1. Choose R . We find that setting $R = 120$ pixels = 0.952 cm is a good choice for all data sets as dn/dr is appreciable at this radius. If dn/dr is too small, division by dn/dr becomes problematic.
2. Set an axial field, B_z .
3. Determine the maximum hold time t_{\max} for $N(t)$. We wish to capture enough of the evolution of $N(t)$ to accurately measure dN/dt . Since we find that most plasmas are similar initially, regardless of B_z , we search for t_{\max} where $n(R) = 2.5 \times 10^6 \text{ cm}^{-3}$. We find that this works well.

4. Scan \vec{B}_\perp to set the optimal \vec{B}_\perp . As detailed below in Section 4.2.2, we choose \vec{B}_\perp to maximize the total charge in the plasma, Q , at some late time.
5. Scan quadrupole field to find neighborhood in β_1 - β_2 space (see equation 2.8) in which to take data. We vary β_1 and β_2 to maximize Q at some late time.
6. Set β and θ_o and image plasmas held for 36 times between $4 \mu\text{s}$ and t_{max} . 36 images is a compromise between wanting accurate dN/dt measurements and wanting experiments of manageable duration.
7. Repeat step 6 for as many β and θ_o as necessary to cover a neighborhood near the optimal quadrupole field.
8. Repeat steps 2-7 for as many B_z as necessary.

4.2.2 Optimal \vec{B}_\perp , β and θ_o

Before we can measure the effect of the quadrupole field, we must first make sure there is no dipole effect and no naturally occurring quadrupole effect. Since the dipole and quadrupole magnets can have both dipole and quadrupole components, tuning is an iterative process, but one that converges rapidly. Let us begin by assuming there is no quadrupole field and focus on the dipole field.

There are many techniques for determining the correct \vec{B}_\perp to apply to cancel the perpendicular component of the Earth's field and any dipole field from the misalignment of the machine with the solenoid. The three techniques that we used were: minimizing RMS radius growth, minimizing diffusion, and maximizing total charge remaining at some fixed late time.

Minimizing RMS radius growth seemed like a good method, but it turns out that at small B_z the plasma radius decreases with time as charge is lost to the wall. The plasma is eaten away from the outside.

Since we are ultimately measuring diffusion, it makes sense to tune \vec{B}_\perp so that we minimize diffusion. This technique is time consuming, however. Moreover, the optimal \vec{B}_\perp was not always well defined in \vec{B}_\perp space.

The total charge technique involves holding the plasma for a fixed time (until there is approximately half of the total charge left) and varying \vec{B}_\perp until this charge is maximized. This technique depends on there being little variation in the total charge at

$t = 0$ as a function of \vec{B}_\perp , and we find that this is true. This technique agrees with the diffusion technique in the range where they can both be used, but is much faster. This gives us confidence that the total charge technique is valid for all B_z . Figure 4.6 is a contour plot showing the total charge remaining as a function of B_x and B_y . We can clearly identify the optimal \vec{B}_\perp from these data to within 10 mG.

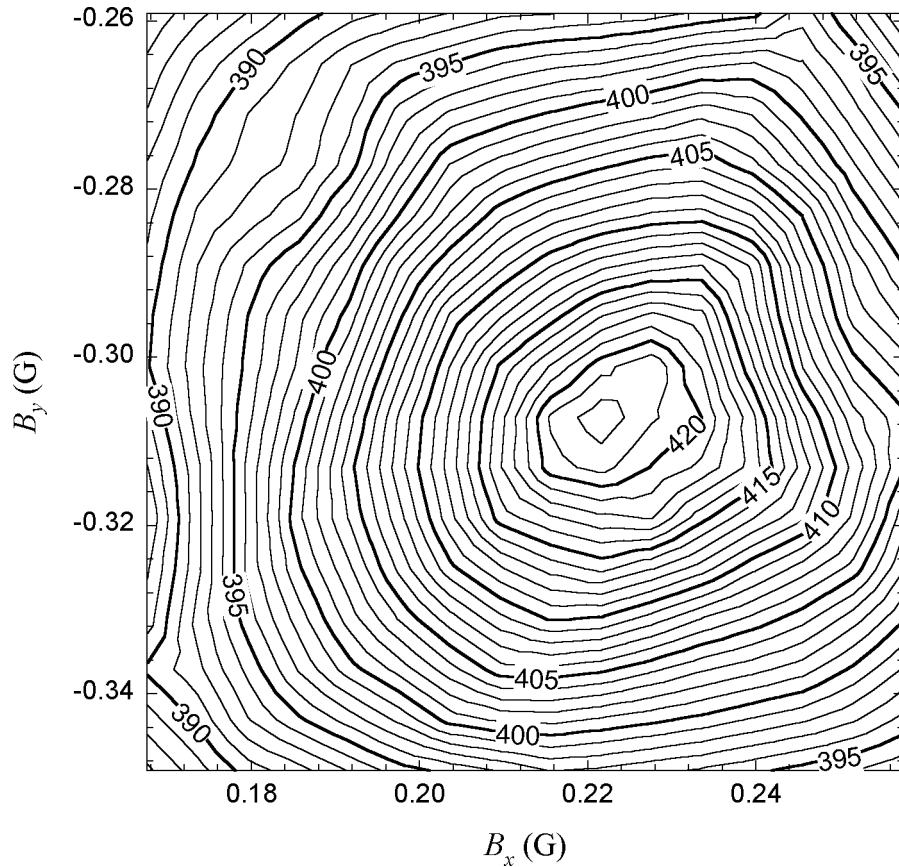


Figure 4.6: We choose B_\perp by maximizing the total charge, Q , remaining at some late time as a function of the perpendicular magnetic field. The contour labels refer to millions of electrons. Here, $B_z = 100$ G.

Figure 4.7 shows the optimal values of \vec{B}_\perp as a function of B_z for the values of B_z used in the subsequent transport measurements. Extrapolating to $B_z = 0$, \vec{B}_\perp is the perpendicular component of the Earth's magnetic field. The steering fields are linear in B_z since they correct for the fields from the main magnet. Because \vec{B}_\perp may compensate for some mechanical misalignments aside from the magnetic field, these data may change

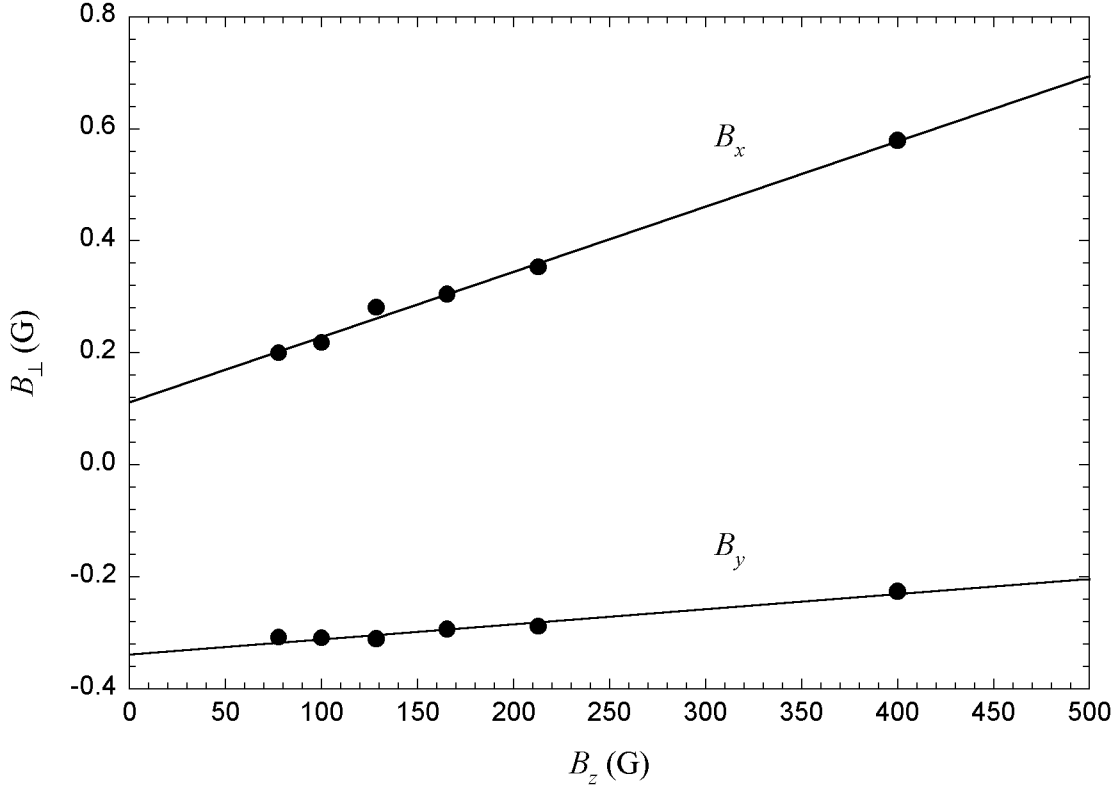


Figure 4.7: The optimal B_{\perp} is linear in the applied axial field and the values at $B_z = 0$ give the Earth's magnetic field.

depending on the temperature of the system as thermal expansion changes the alignment of the gates.

Once we have established \vec{B}_{\perp} , we then use the same technique with β_1 and β_2 to determine the optimal quadrupole field to apply to cancel out any naturally quadrupole field. Since an off center quadrupole field creates a dipole field, we repeat the process for dipole tuning. We find that quadrupole fields less than 0.1 G/cm create dipole fields of less than ~ 30 mG.

4.3 Data and Analysis

To measure transport as a function of ω_{Et_b} , we must vary ω_{Et_b} . To vary ω_E we can look at a different radius if ω_E is not constant, change the density, or change B_z . To

vary t_b , we can change kT or L . I discussed the methods of and difficulties with these techniques in Section 2.1.

We analyze the data as follows:

1. We convert the image of the plasma from cartesian coordinates to polar coordinates and average over θ to find $n(r, t)$.
2. A Poisson solver uses the radial profile to find the potential, $\phi(r, t)$, the corresponding electric field, $E_r(r, t) = -\partial\phi(r, t)/\partial r$, and rotation frequency, $\omega_E(r, t) = E_r(r, t)/B_z r$.
3. We compute $N(R, t)$ from $n(r, t)$.
4. We calculate dN/dt and dn/dr .
5. We choose ω and find the corresponding t from $\omega_E(t)$. We interpolate dn/dr and dN/dt to find these quantities at t .
6. We calculate D as in equation 4.21 for each quadrupole field applied.
7. We find the minimum of the resulting “diffusion bowl” in β_1 - β_2 space and compute the average diffusion at some distance from this minimum since we assume that the effect of the quadrupole field is independent of θ_o .

4.3.1 Diffusion Measurement Example

We begin with an axial field of 100 G and a plasma confined between gates separated by $L = 34.02$ cm. The measured temperature is about 1.6 eV. We choose a radius of 0.95 cm so that we are in the region of $n(r)$ where the slope is appreciable. The initial rotation frequency, $\omega(r = 0.95, t = 0)$ is about 4.0×10^6 rad s⁻¹. After 400 ms, the total amount of plasma has decreased significantly, and $\omega(r = 0.95, t = 400) = 8.0 \times 10^5$ rad s⁻¹. We accumulate $n(r, t)$ for a series of perturbations.

We measure the slope dn/dr from a single image, $n(r, t_0)$ at $R = 0.95$ cm by fitting a parabola to a small portion of $n(r)$. For the radial profile in Figure 4.8, the slope is $-1.744 \pm 0.009 \times 10^6$ cm⁻⁴ at $R = 0.95$ cm, where the error is from the uncertainty in the coefficients of the fit. We calculate $N(R, t)$ and then we compute dN/dt by fitting a parabola to a local region of $N(t)$. For the data in Figure 4.9, the slope at $t = 195$ ms (the time that Figure 4.8 corresponds to) is $2.029 \pm 0.006 \times 10^7$ cm⁻¹s⁻¹. The choice of t at

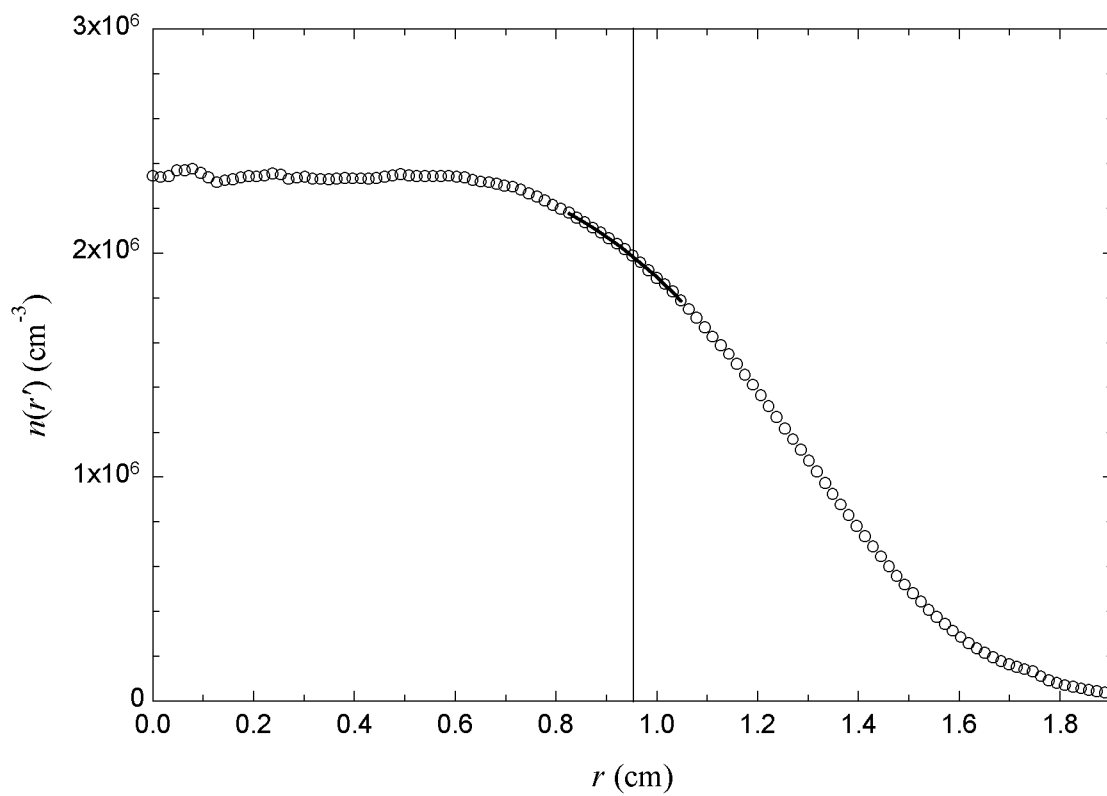


Figure 4.8: We use the azimuthally averaged radial profile to calculate the slope dn/dr . The plasma extends to the wall at $r = 1.905$ cm. We fit a parabola to a region that is 0.22 cm wide in order to capture as many points as possible while ensuring that a parabola is a good approximation of $n(r)$.

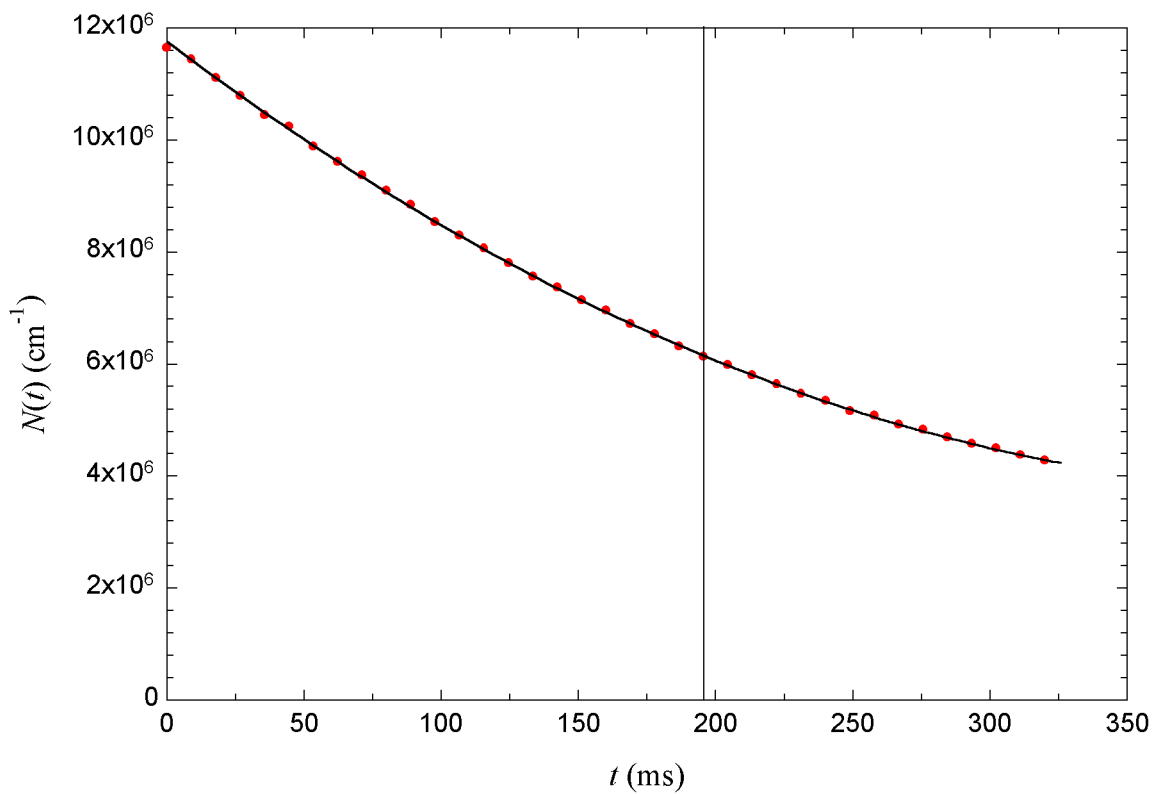


Figure 4.9: The charge per unit length within a radius $r = R$ decreases as a function of time because of transport processes occurring within the plasma. We use these data to measure dN/dt . We fit a parabola to the largest number of data points possible such that the total mean squared error is less than a threshold value. In this Figure, all data, except the point at $t = 0$, are included in the fit.

which to measure D is arbitrary since we do not expect transport to have an explicit time dependence. We choose t by some auxiliary condition, for example to have $n(R)$ or $\omega(R)$ be constant across a data set. The choice $t = 195$ ms here corresponds to $\omega = 2.0 \times 10^6$ rad s⁻¹. Then we calculate D ; for the data in Figures 4.8 and 4.9, $D = 1.95 \pm 0.02$ cm²s⁻¹. Note that this technique requires axial and azimuthal invariance because we assume the camera images give $n(r, t)$, without θ or z dependencies.

Figure 4.10 shows the diffusion as a function of quadrupole field at $\omega = 2.0 \times 10^6$ rad s⁻¹. Notice that the minimum diffusion does not occur at zero perturbation. This is evidence that we are correcting for naturally occurring field errors by applying a quadrupole field. For the same data set, the minimum changes as a function of ω . The minimum changes by ~ 0.010 G/cm over the range of useful ω . This is not understood. Perhaps the quadrupole field not only compensates for inherent quadrupole perturbations, but also compensates for confinement gate effects. As the plasma density decreases over time, the plasma extends less into the inject and dump gate regions. In any event, we find values of D relative to the minimum of the diffusion surface at constant ω .

4.3.2 Background Diffusion Processes

For some value of the quadrupole field, $D(\beta_1, \beta_2)$ has a minimum. But D is not zero at this minimum because there are other diffusion processes occurring in the plasma in addition the diffusion caused by the quadrupole field. To extract the effect of the quadrupole field from the total diffusion, we subtract the diffusion at the minimum from the average diffusion at some distance from the minimum. We justify this subtraction by noting that diffusion coefficients are proportional to the square of the step size, and since uncorrelated random steps add in quadrature, diffusion coefficients add linearly. We must therefore assume that the background diffusion processes are uncorrelated to the quadrupole field effect.

The vacuum pressure is low enough that we do not expect collisions with neutral atoms to contribute to diffusion. If there are mechanical misalignments or magnet coil imperfections, then electrostatic and magnetic field errors will cause transport. Unintentionally excited plasma modes may lead to diffusion. Similarly, rotational pumping may cause transport. Collisions between electrons cause transport to help to drive the plasma towards thermal equilibrium.

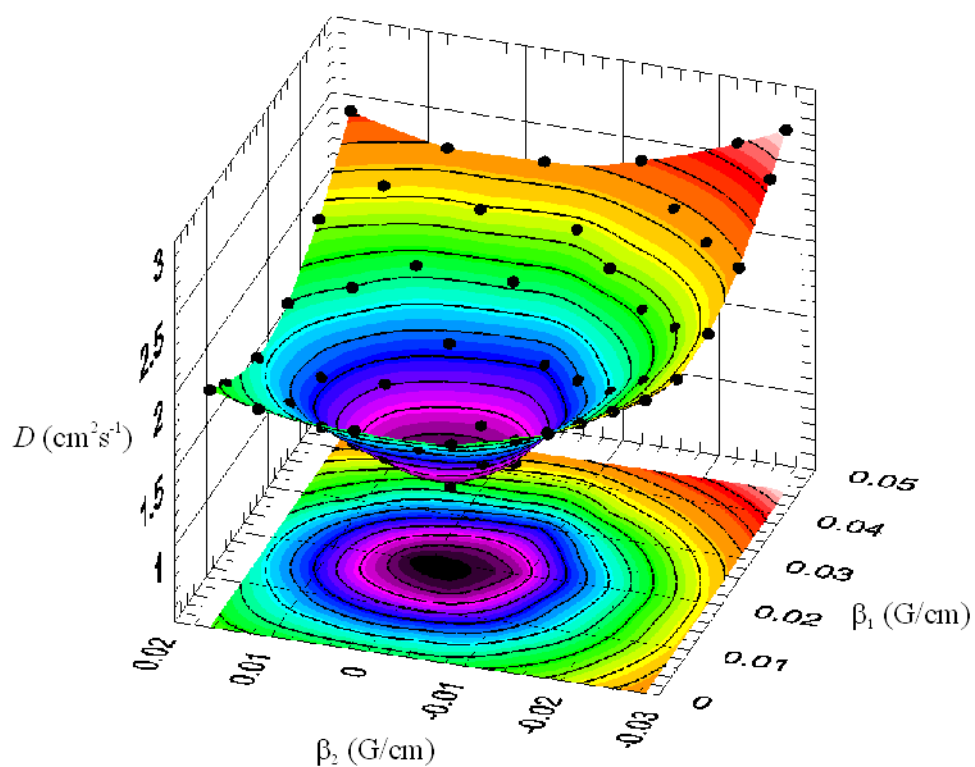


Figure 4.10: Diffusion from the application of a quadrupole field. This data is taken at $B_z = 100 \text{ G}$ and $\omega = 2.0 \times 10^6 \text{ rad s}^{-1}$. We choose values of β_1 and β_2 in a checkerboard pattern and the data (solid dots) show that there is an optimal quadrupole field and that diffusion increases away from this optimal value.

4.3.3 β Dependence

Data like those in Figure 4.10 allow us to verify the β^2 scaling predicted by the model. We measure D relative to the minimum of the diffusion surface and Figure 4.11 shows that, over a wide range of parameters, D does scale like β^2 for small perturbations. One difference between diffusion in the plateau regime and the banana regime is the scaling with the perturbation strength. For plateau diffusion, the scaling is β^2 , whereas for banana diffusion the scaling is $\beta^{1/2}$. So our data is consistent with diffusion in the plateau regime.

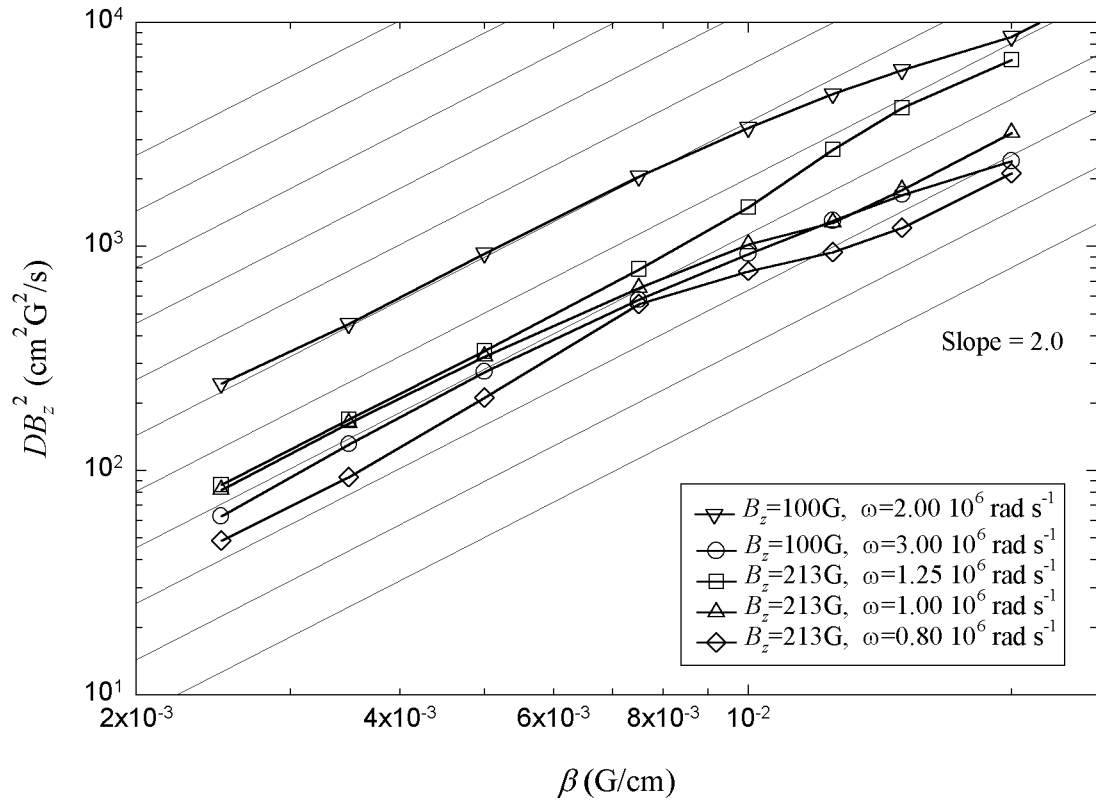


Figure 4.11: At several B_z and ω , the diffusion is seen to be proportional to β^2 as expected, consistent with plateau diffusion.

4.3.4 ω and B_z Dependencies

Next, we investigate the ω dependence of the phenomenon. After choosing B_z , the easiest way to vary ω is simply to wait, since n naturally decreases as a function of time. For example, for the plasma we considered in Section 4.3.1, ω decreased from

$4 \times 10^6 \text{ rad s}^{-1}$ to $8.0 \times 10^5 \text{ rad s}^{-1}$ in 400 ms. Therefore, we can repeat the measurement of the “diffusion bowl” at several values of ω for one B_z . We choose a perturbation strength, $\beta = 0.020 \text{ G/cm}$ here. We average diffusion at a distance of 0.020 G/cm from the minimum diffusion over many angles of the quadrupole field. We estimate the uncertainty from the standard deviation of these data to be approximately 7%. This uncertainty dominates over the uncertainty in any one individual measurement of D . Figure 4.12 shows the results.

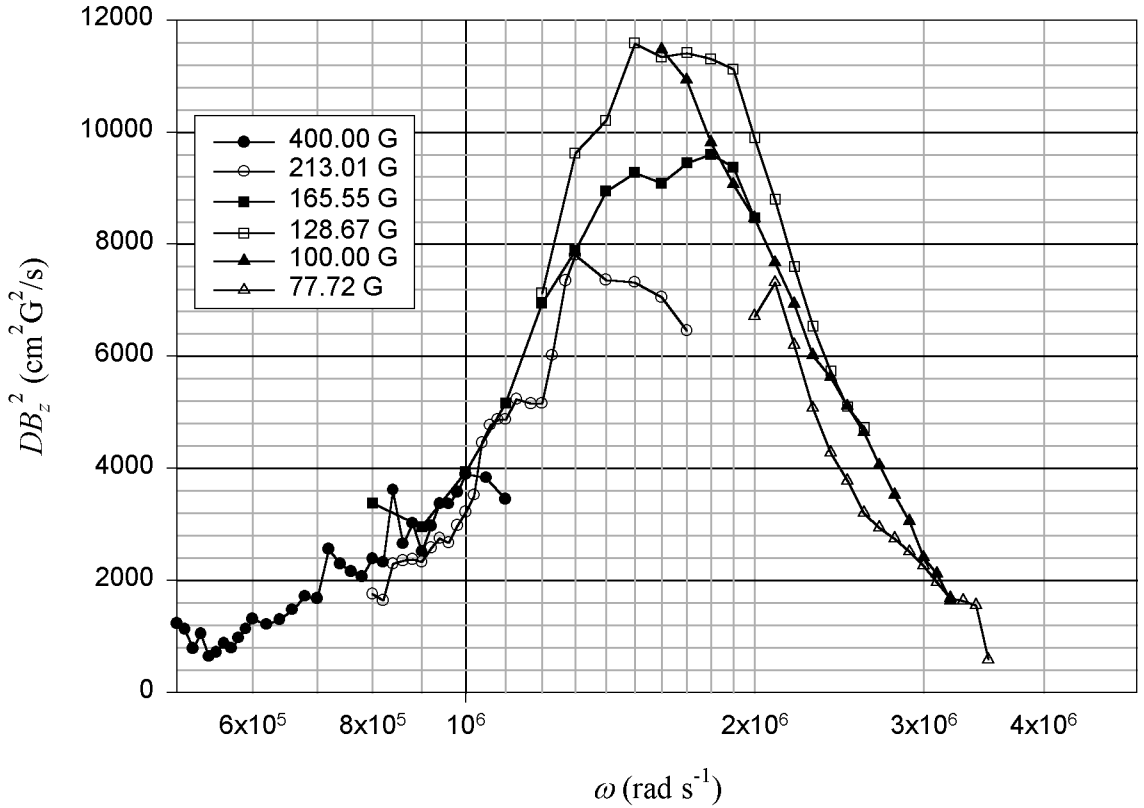


Figure 4.12: Since ω decreases as a function of time, we can measure $D(\omega)$ over a range of ω at fixed B_z . There is significant overlap of ω ranges for similar B_z . The diffusion data show a scaling with B_z^2 and a resonant behavior. Here, $\beta = 0.020 \text{ G/cm}$.

The data show that the quadrupole field enhances diffusion resonantly in ω . This is the most important feature of the data. As ω increases from 10^5 rad s^{-1} the diffusion grows. But above $\omega \approx 2 \times 10^6 \text{ rad s}^{-1}$ the diffusion decreases again. Another observation is that it is DB_z^2 that we plot on the vertical axis and not simply D . The model has an explicit B_z^{-2} scaling, and so DB_z^2 is independent of B_z . Since the data for various B_z in Figure 4.12 overlap, this suggests that this B_z scaling is correct.

Our formula for D scales like ω^2 at small ω when the exponential term is near unity. We test this scaling at small ω by replotting Figure 4.12 on log-log axes in Figure 4.13. The least squares fit line to the data with $\omega < 1.3 \times 10^6 \text{ rad s}^{-1}$ gives a slope of 2.05 ± 0.09 .

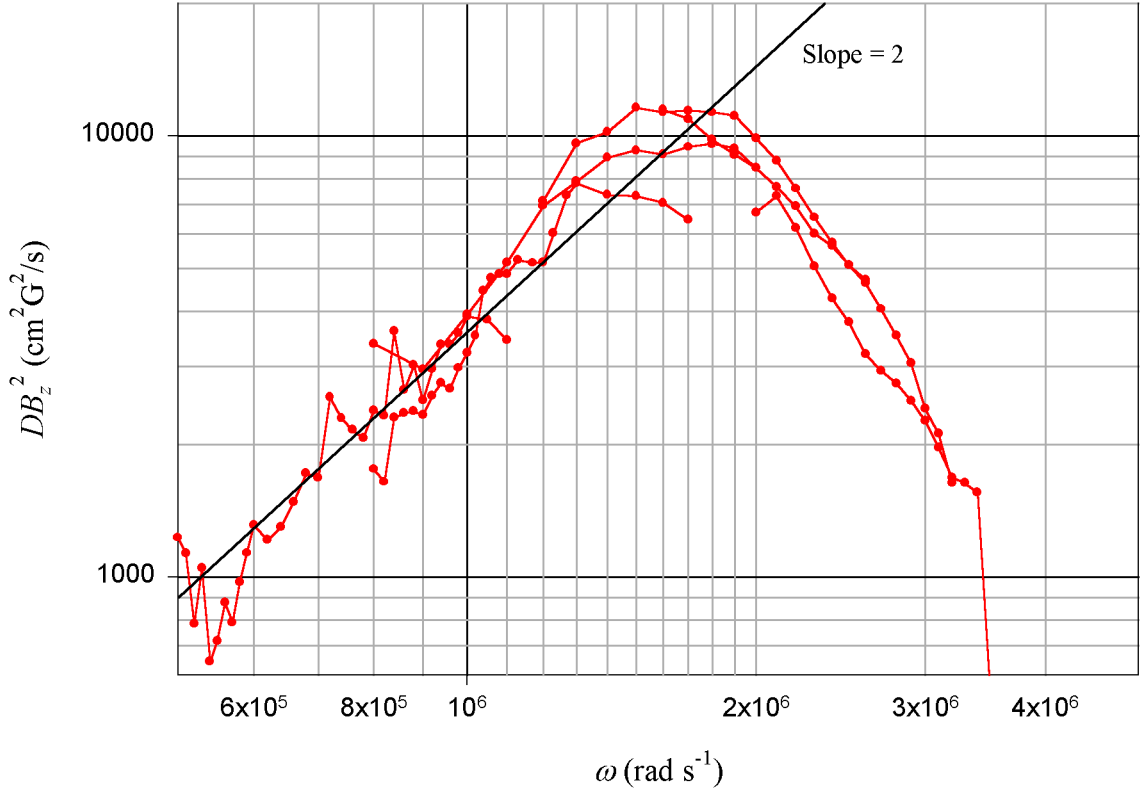


Figure 4.13: The same data in Figure 4.12 plotted on log-log axes show that for $\omega < 1.3 \times 10^6 \text{ rad s}^{-1}$, the diffusion scales like ω^2 . We no longer distinguish between the different B_z used to accumulate the data.

4.3.5 L Dependence

We repeated these measurements for different L . As discussed above, $D_{\max} \propto L$ and $\omega_{\text{res}} \propto L^{-1}$. Figure 4.14 shows the raw data where, for each L , we used several B_z . We extract ω_{res} and D_{\max} from Figure 4.14 and show the results in Figures 4.15 and 4.16. The trends are in the right direction, although the exact dependencies are difficult to obtain from these data. The D_{\max} scaling is consistent with L and the ω_{res} scaling is consistent with L^{-1} .

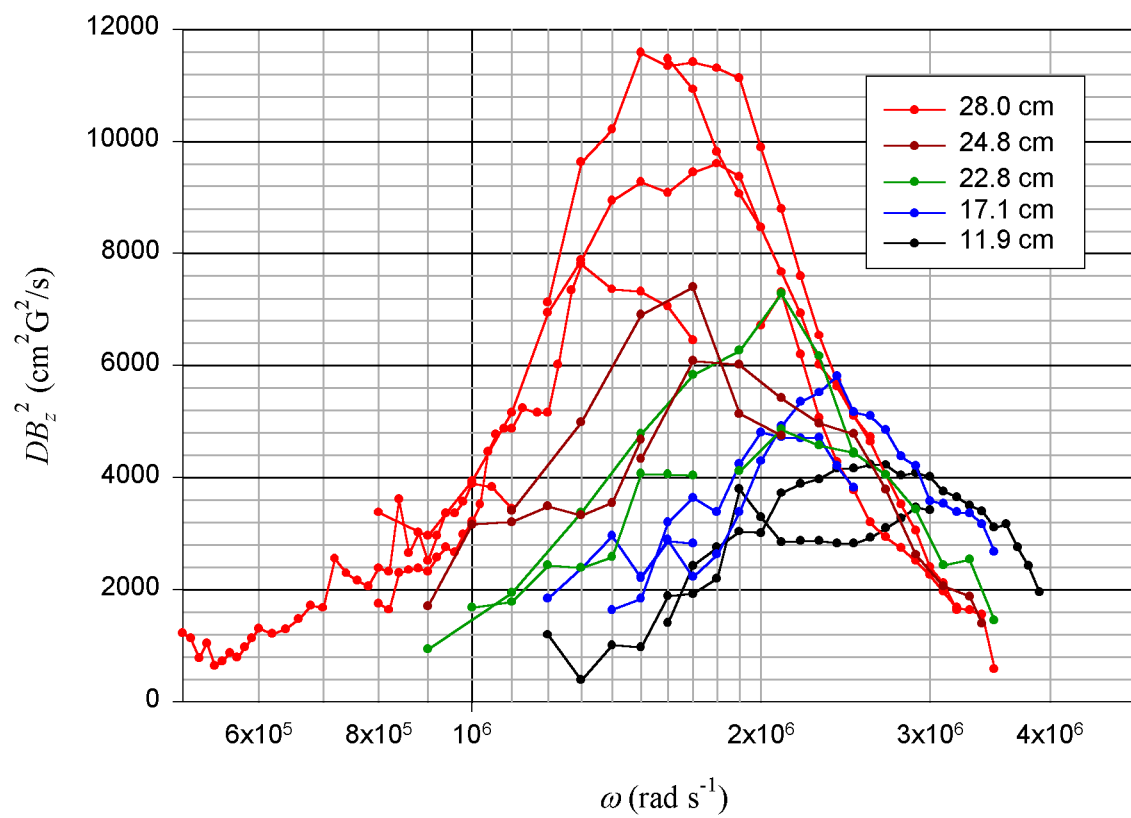


Figure 4.14: As we decrease the length, the peak moves to higher ω and the maximum diffusion decreases. The different curves for each L correspond to different B_z .

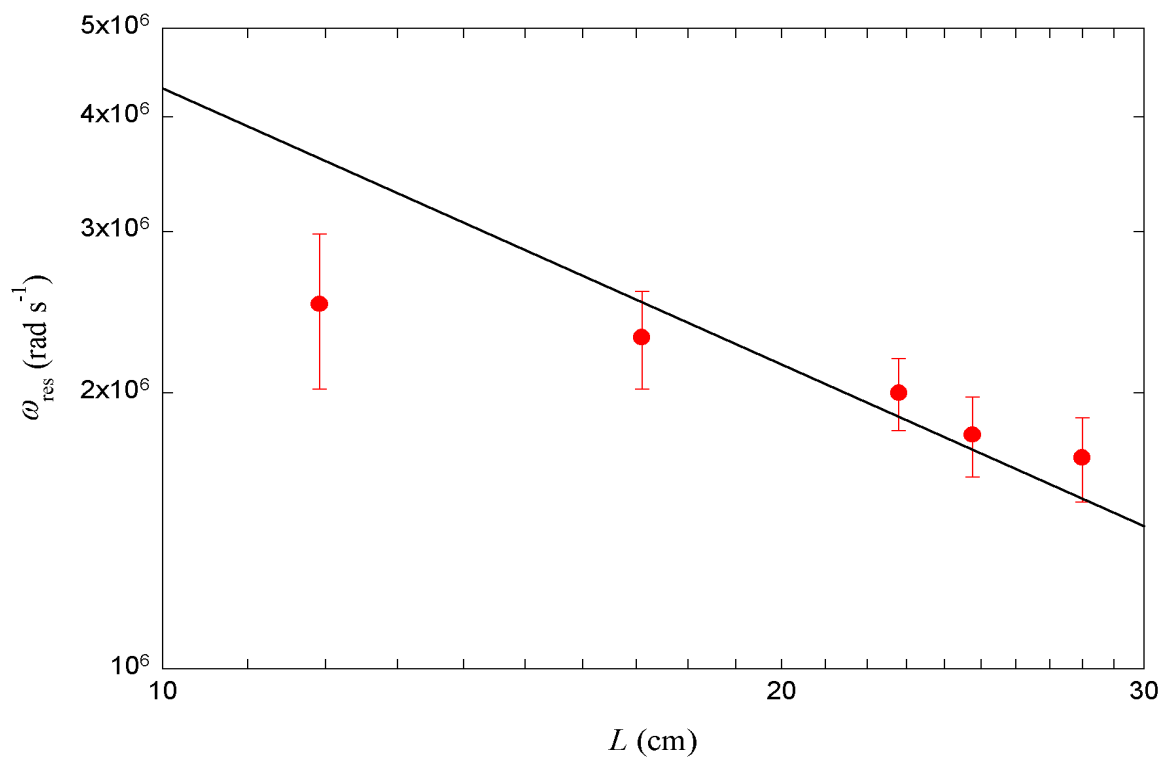


Figure 4.15: The value of ω_{res} decreases as L increases. Excluding the shortest plasma, the data are marginally consistent with a line with slope -1 (solid line).

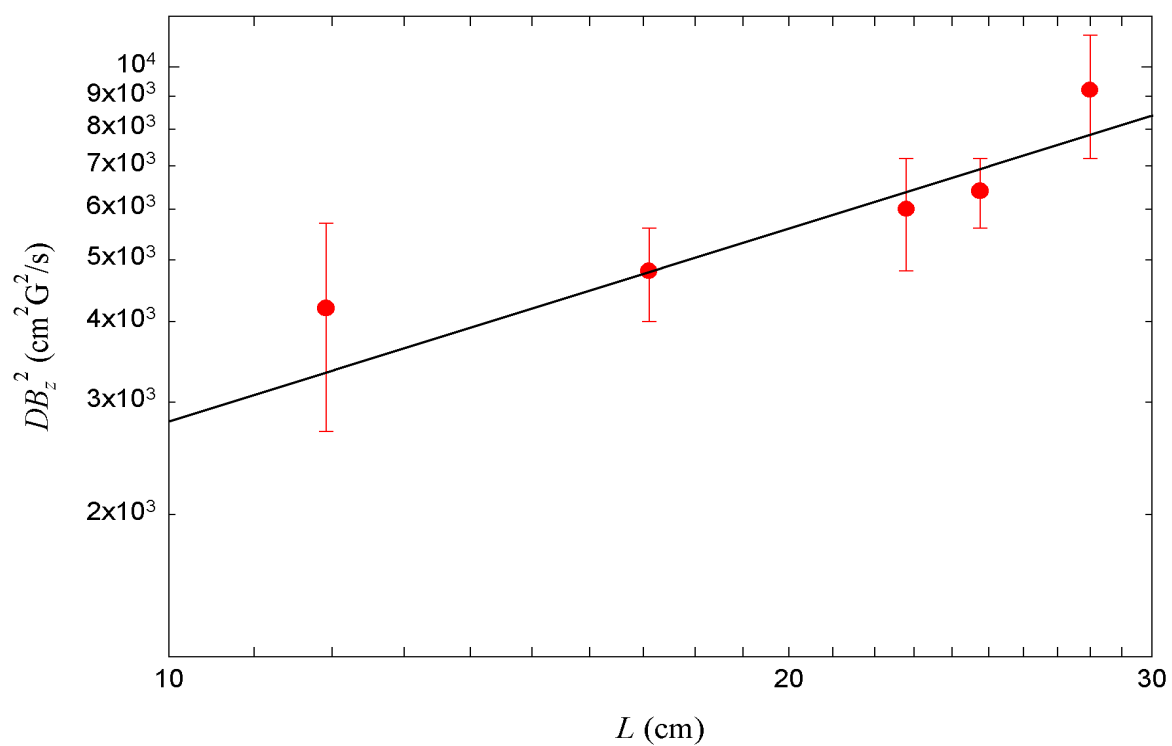


Figure 4.16: As L increases, the maximum diffusion increases and is consistent with a line with slope 1 (solid line).

4.3.6 kT Dependence and Theory Fit

To test the temperature dependence of the quadrupole induced diffusion, we heated the plasma for 1 ms by applying noise signals to the wall of the trap after injecting the plasma. We obtained temperatures of up to 6.5 eV in this fashion. As discussed above $D_{\max} \propto kT$, and $\omega_{\text{res}} \propto \sqrt{kT}$. So D_{\max} should grow and the peak should move to larger ω as we heat the plasma. Figure 4.17 shows that although the resonance moves in the correct direction, the maximum diffusion decreases as the plasma temperature increases. This stands in contrast to the predictions of our model.

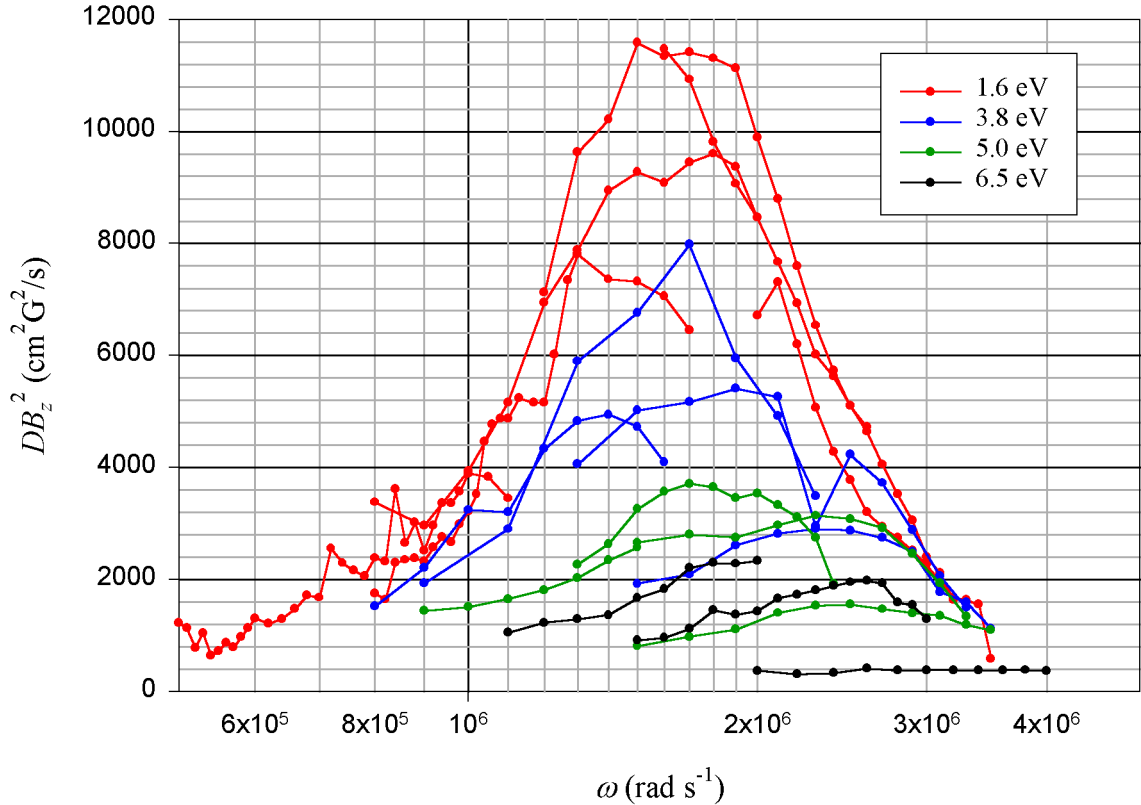


Figure 4.17: As we heat the plasma, the peak shifts to larger ω while the overall diffusion decreases. The different curves for each kT correspond to different B_z .

Returning to the data shown in Figure 4.12, we now add a curve representing our model in Figure 4.18. In principle, there are no free parameters in the model; we either set or measure β , B_z , R , L , kT , and ω . Nevertheless, to achieve even moderate agreement with the model, we must use an overall multiplicative factor of about 0.3, and set kT to

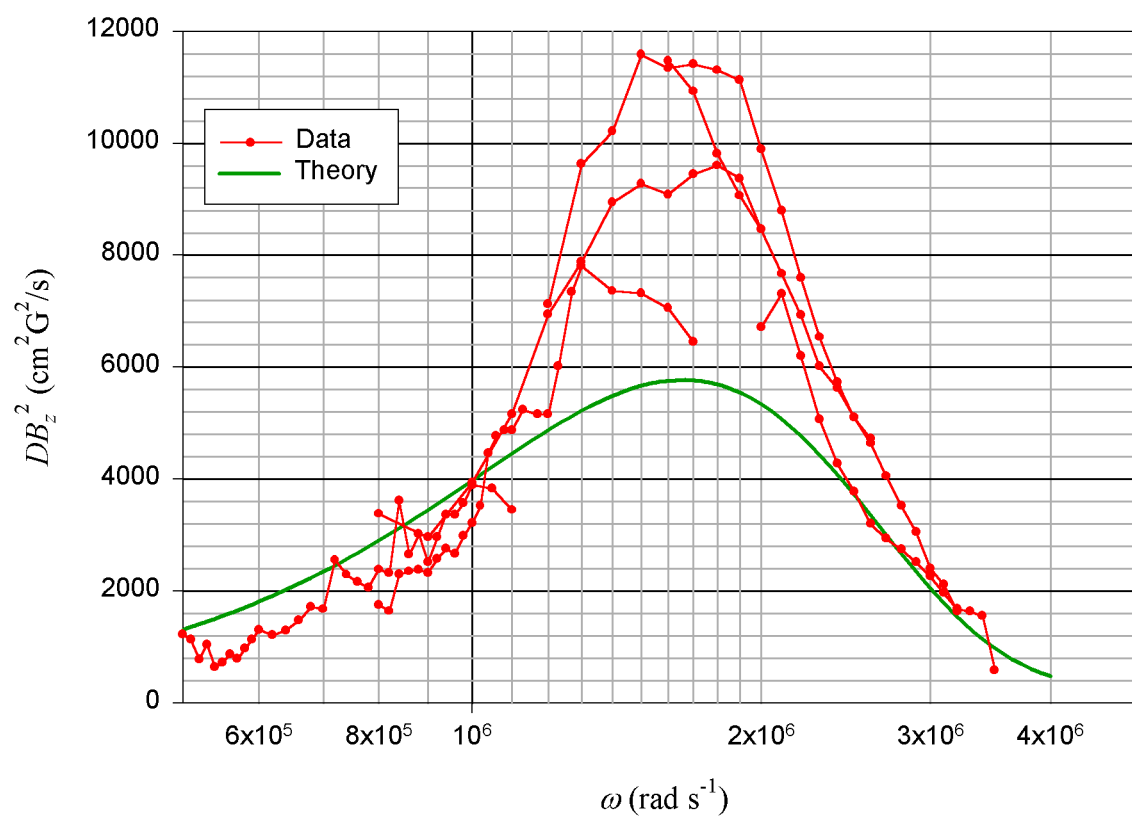


Figure 4.18: In principle, there are no free parameters in our model. However, a theory curve fits the data reasonably well only if we use an artificially low temperature of 0.34 eV. An independent measurement shows the temperature is 1.6 eV.

be 0.34 eV, in contrast to the measured value of 1.6 ± 0.1 eV. Given the crude nature of our model, we might expect multiplicative factors of order unity. The curve showing the fit of the theory to the data contains terms up to $N = 10$. Adding more terms does not change the appearance of the curve. This problem with kT is a serious shortcoming of our model. It might be that off resonance electrons dominate the transport, that the effect of the quadrupole field is not a purely diffusive process, or that because λ is small there are finite Larmor radius effects.

4.3.7 r Dependence

We find that is difficult to test the radial dependence of the transport. It seems as though clean measurements are possible only in a small neighborhood near $r \approx 1$ cm. This trouble comes from the noise in the measurements of dn/dr at extreme radii and the measurements of dN/dt at large radii. At large and small radii, $dn/dr \approx 0$ and is therefore more sensitive to noise. In fact, for $\beta > 0.1$ G/cm, we occasionally observe slightly hollow radial profiles where $dn/dr > 0$ at small r . Purely diffusive transport cannot create hollow radial profiles. Small dn/dr causes problems since we must divide by dn/dr to compute D . At large radii, $dN/dt \approx 0$. In either case, $D \propto (dN/dt)/(dn/dr)$ is poorly behaved.

4.3.8 Dipole Diffusion

To be certain that we are really testing the effect of quadrupole fields and not just the effect of the dipole component of the quadrupole magnets, we repeat some measurements but with a dipole perturbation rather than a quadrupole perturbation. We choose $B_{\perp} = 0.020$ G to correspond to the quadrupole field, $\beta = 0.020$ G/cm. The results in Figure 4.19 show that the dipole field has relatively little effect. Not only does this assure us that we are actually measuring the effect of the quadrupole field, but it also tells us that residual dipole fields remaining from imperfect tuning are unlikely to greatly affect our measurements.

4.3.9 Flux

It is possible that the discrepancies between our model and our data are due to our interpretation of the data in terms of diffusion. We do not directly measure D , rather we measure dN/dt and dn/dr . To calculate D from our data, we assumed that $\vec{\Gamma} = -D\vec{\nabla}n$. We neglect any contribution to the flux from a mobility term, $-\mu n\vec{E}$. If we use the Einstein

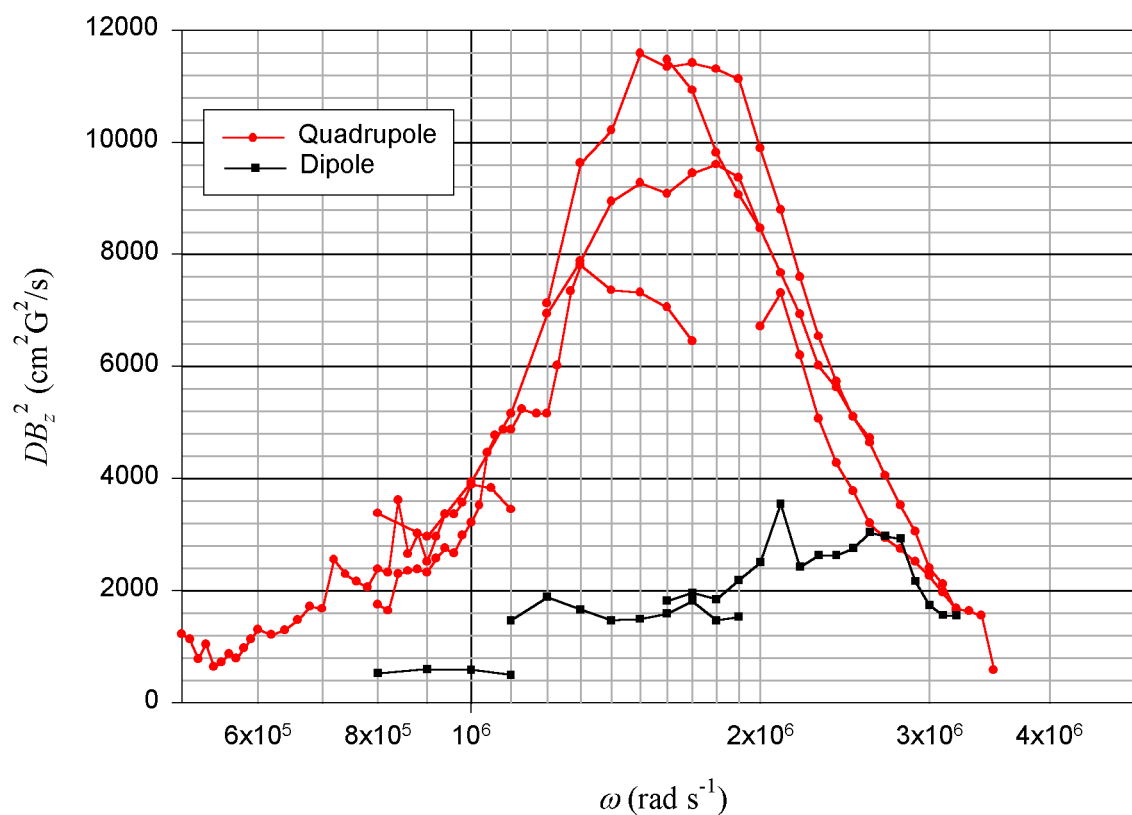


Figure 4.19: We apply a dipole error field of 20 mG which is comparable to the quadrupole field of 20 mG/cm and we see that the diffusion is small. We are confident that when we apply a quadrupole field we are not simply seeing the effect of a dipole component of the quadrupole magnets. The different curves for both the quadrupole and dipole perturbations correspond to different B_z .

relation, $\mu = De/kT$, and we use $\omega = E/Br$, we can write the mobility contribution to the flux as $Dne\omega Br/kT$. The diffusion coefficient is now

$$D = \frac{1}{2\pi R} \frac{dN}{dt} \left(\frac{dn}{dr} + \frac{ne\omega BR}{kT} \right)^{-1}. \quad (4.22)$$

If we include the mobility term in our analysis of the data and try temperatures between 0.25 eV and 2 eV, we find that D is reduced by about an order of magnitude while ω_{res} does not change. Therefore, it is not an omitted mobility term that is the root of our problem with the temperature dependence of our model. It may be that the flux cannot be simply written as a diffusive term and a mobility term proportional to \vec{E} .

Since Γ is closer than D to what we actually measure in our experiment, let us consider Γ . We measure R and dN/dt , and the flux is $(dN/dt)/2\pi R$. We need not make any further assumptions. Figure 4.20 shows Γ versus ω for the same parameters as in

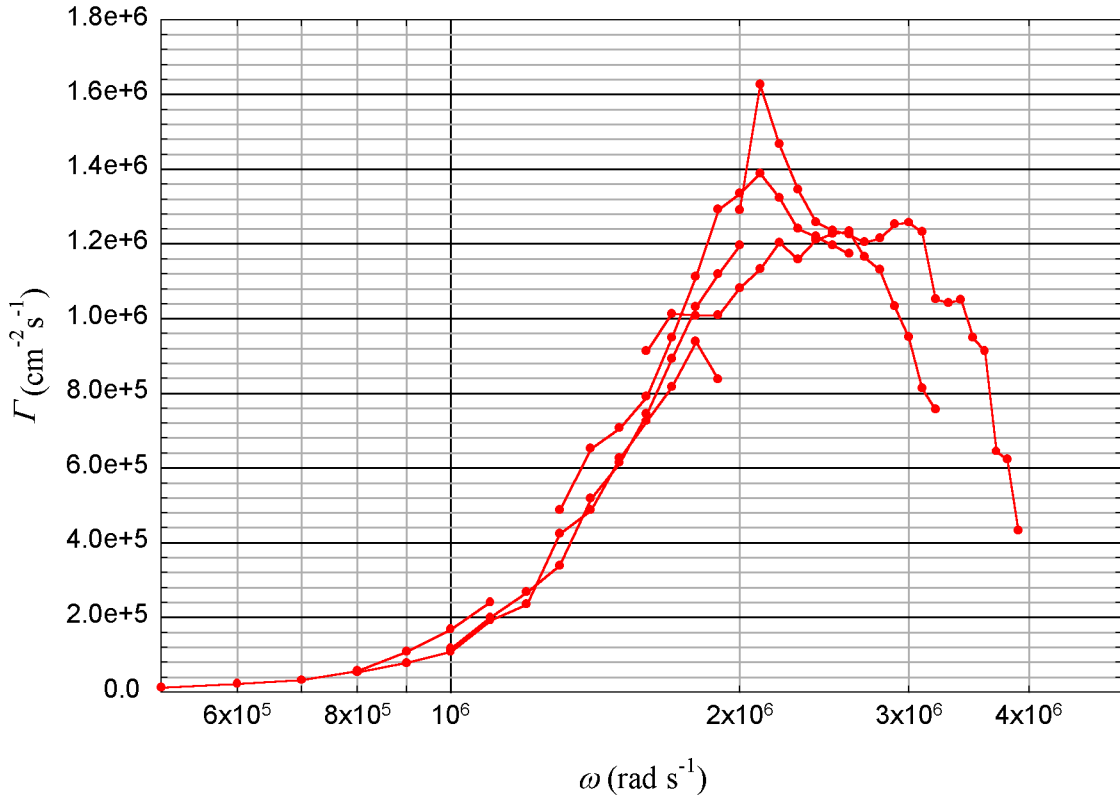


Figure 4.20: Γ vs. ω shows the same resonant behavior as D vs. ω . However, unlike D , Γ has no explicit B_z dependence. The different curves correspond to different B_z . $L = 28$ cm.

Figure 4.12. Just as there is a resonant peak in $D(\omega)$, there is a resonant peak in $\Gamma(\omega)$.

Notice that flux does not seem to exhibit an explicit B_z dependence like diffusion does, as the data from different B_z appear to coincide in Figure 4.20. The flux increases by $\sim 30\%$ above the background level near resonance.

Figures 4.21, 4.22 and 4.23 show $\Gamma(\omega)$ for shorter plasmas. These data show that ω_{res} increases as L decreases, as we expect for a bounce resonant effect. Indeed, ω_{res} is beyond the reach of our machine in Figure 4.23. For the shorter plasmas, there now appears to be an explicit B_z dependence because the data sets for different B_z do not coincide with one another.

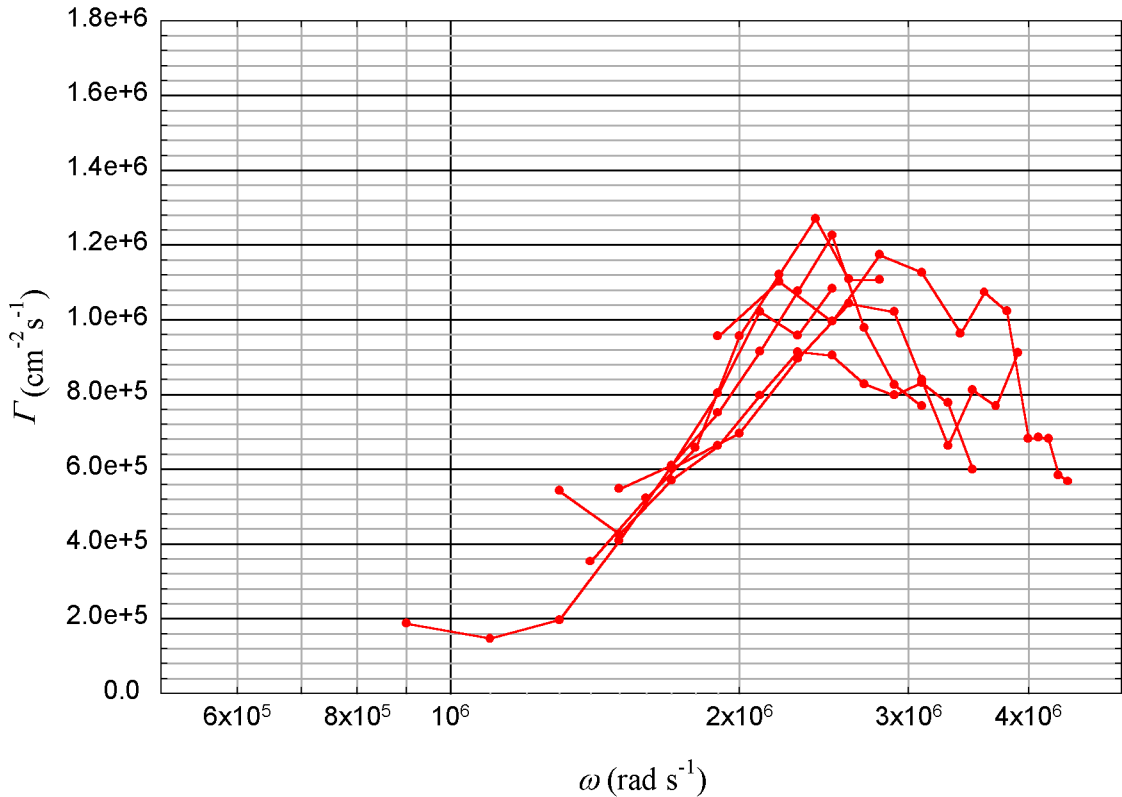


Figure 4.21: Γ vs. ω shows the same resonant behavior as D vs. ω . However, unlike D , Γ has no explicit B_z dependence. The different curves correspond to different B_z . $L = 24.8$ cm.

A simple model of the flux [40] better predicts the location of the maximum flux, but exhibits an explicit B_z dependence. The model considers the trajectories given by equation 4.10 expanded to second order in the argument of the exponential. The model gives the net radial velocity as the ratio of the θ_o averaged radial step after two bounces to twice the bounce time. This radial velocity is then averaged over the thermal distribution.

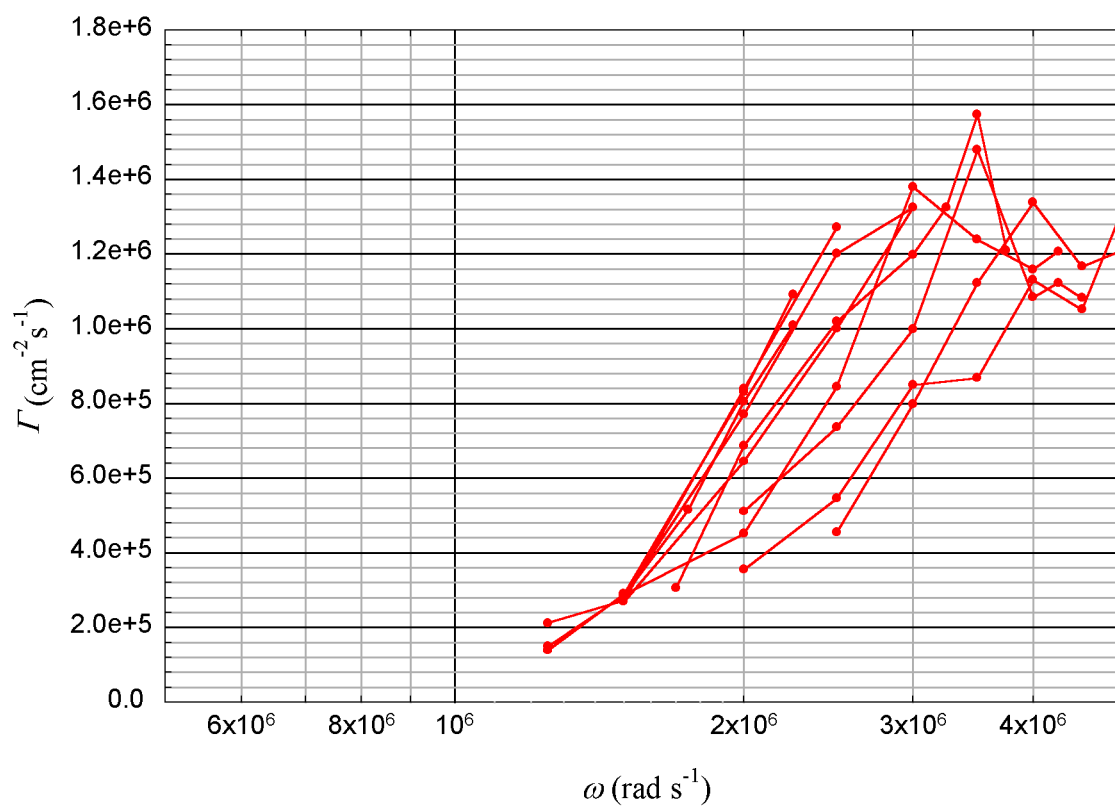


Figure 4.22: Γ vs. ω shows the same resonant behavior as D vs. ω . The different curves correspond to different B_z . Unlike Figures 4.20 and 4.21, the data for different B_z do not coincide and this suggests an explicit B_z dependence. $L = 17.1$ cm.

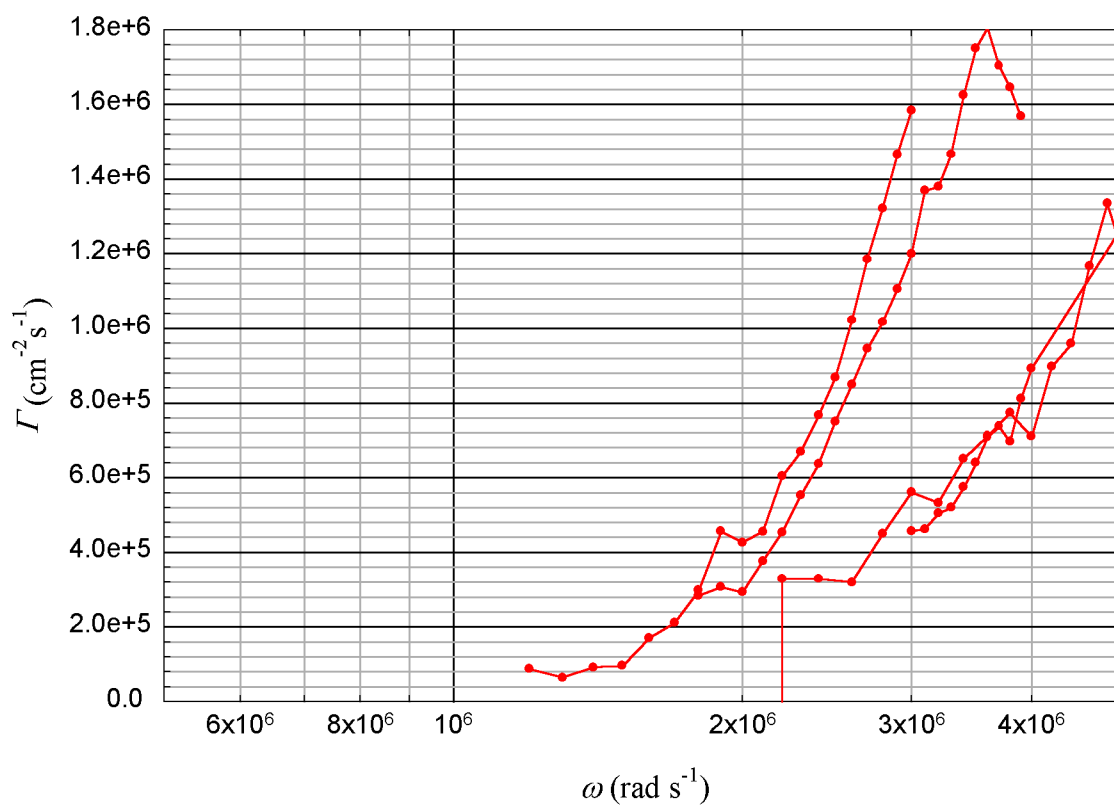


Figure 4.23: Γ vs. ω shows only increasing flux with ω . We cannot reach ω_{res} for a plasma this short. As with the 17.1 cm plasma in Figure 4.22, Γ appears to have an explicit B_z dependence. The different curves correspond to different B_z . The leftmost curve is for $B_z = 158.11$ G. The next curve is for $B_z = 100.00$ G. The two curves on the right are for 63.23 G and 40.00 G. $L = 11.9$ cm.

Multiplying by the density gives the flux.

In a variation of this model, we find the electrons' time averaged radial displacement as given by the exact solution of equation 4.10. We divide by the collision time to find the radial velocity. Multiplying by the density gives the flux. The flux given by this model is orders of magnitude too small to account for the measured values.

4.4 Summary

We have shown that a quadrupole field applied to a plasma confined in a Malmberg-Penning trap resonantly enhances transport. Even a small quadrupole field (0.020 G/cm compared to an axial field of 100 G) doubles the diffusion in the system; this is a strong effect, likely to be important even when the plasma is off resonance.

The diffusion scales like β^2 , suggesting that we are in the plateau regime of transport in which there are frequent collisions. The scaling of ω_{res} with L and kT is what one expects if diffusion from the quadrupole field is a bounce resonant effect. The resonance condition is $\omega_E t_b = \omega_E L (kT/m)^{-1/2} = \pi/2$ and so by decreasing L or increasing kT , ω_{res} increases. We also find that the diffusion has an explicit B_z^{-2} dependence.

The β and B_z scalings agree with our simple model of the effect, while the L scaling is consistent with our model. The kT scaling of ω_{res} is consistent with our model, but the scaling of D_{max} with temperature that we observe does not agree with the model. We observe that D_{max} decreases as kT increases, while our model predicts the opposite. Moreover, the magnitude of kT that we must use in our model to obtain even moderate agreement with the data is significantly smaller than the measured temperature. The model best fits the data when we use $kT = 0.34$ eV while the actual temperature is 1.6 eV. These difficulties with kT remain unexplained and suggest that we need a better model of quadrupole induced transport.

The r dependence proves difficult to test. In principle, we can analyze the camera images at any r . However, the radial profiles are quite flat at small r and so the numerical difficulty associated with dividing small numbers limits us to a narrow range in the neighborhood of $r \approx 1$ cm. The range is too narrow to allow us to draw any conclusions about the r dependence of D .

Chapter 5

Conclusions

5.1 Summary

We have applied an axially invariant, transverse quadrupole field to a pure electron plasma confined in a Malmberg-Penning trap and observed the effects the quadrupole field has on the shape of the plasma and on transport within the plasma. The quadrupole field distorts the parallel magnetic field lines into flux tubes with elliptical cross sections. Whether the $\vec{E} \times \vec{B}$ rotation is faster or slower than the bounce time determines the properties of both the plasma shape and the transport.

If the plasma rotates quickly, we observe the plasma to smear out into a cylinder as all radial oscillations average out. If the plasma rotates slowly, we observe that the plasma has the shape of a flux tube, circular in the center and elliptical on each end but with the ellipses rotated by 90° with respect to one another. The ellipticity is proportional to both the quadrupole field and to the length of the plasma. The angle of orientation of the plasma follows the angle of the applied quadrupole field.

The transport created in the plasma by the quadrupole field exhibits a strong resonance in ω . The resonance has the proper scalings for a bounce resonant effect where $\omega_E t_b = \pi/2$. As L decreases or kT increases, ω_{res} increases. We find that the diffusion coefficient, $D(\omega)$, has an explicit B_z dependence and scales like β^2 . This scaling with the perturbation strength is consistent with diffusion in the so called plateau regime. The peak diffusion, D_{max} , increases with L , whereas D_{max} decreases with kT .

We measure diffusion coefficients of order $1 \text{ cm}^2/\text{s}$ at resonance for a perturbation of only 0.020 G/cm . The perturbation is small compared to the typical axial field of

100 G. In antihydrogen experiments, quadrupole fields whose strengths are comparable to the axial fields strength will be used. Therefore, we expect these experiments to have trouble confining antiprotons and positrons because of the proportionately larger quadrupole fields. Typical experiment parameters will be $B_z = 2$ T, $n = 10^8 \text{cm}^{-3}$, $L = 1$ cm and $T = 4$ K. We estimate that $\omega_E t_b \approx 0.6$. This places them near the resonance where quadrupole induced transport is greatest. Even if operating off resonance, the magnitude of the quadrupole field will be strong enough to severely limit confinement times.

The results I report in this thesis provide a clear demonstration of a bounce resonant effect in a plasma system. A simple model of the diffusion does not predict the observed dependencies on kT , but agrees with the β , L , and explicit B_z dependencies. Clearly, we need a more detailed model. Our model only treats resonant electrons while it may be that off resonance electrons dominate the transport. Perhaps the transport is not purely diffusive, and so it might be more appropriate to formulate a model of the radial flux to compare with our experimental observations. Regardless, experiments planned by the ATHENA and ATRAP collaborations will face difficulty trying to confine antiprotons and positrons while preparing to make antihydrogen because of the strong transport induced by quadrupole magnetic fields.

5.2 The Future

To study this phenomenon further, one may want to build a special purpose apparatus which would be better suited for applying quadrupole fields. The Malmberg-Penning trap we used was not designed with quadrupole field experiments in mind. While it is a useful machine that is well suited for a variety of plasma experiments, there are several changes that one might make.

In our machine, the quadrupole is on during the injection, holding, and dumping of the plasma. This is because the timescale for the magnetic field to diffuse into the trap, τ , is longer than the timescale for some experiments. If we want to apply the quadrupole field only after we inject the plasma, we must reduce τ . We could place magnet coils inside the vacuum chamber, much closer to the trap walls. Further, we could modify the walls of the trap to reduce τ .

Making the trap walls thinner would decrease τ . If the trap walls were made of stainless steel, they could be made very thin. We measured the diffusion of magnetic fields

through 3.5" diameter stainless steel cylinders with wall radii of 0.016", 0.035", 0.060" and 0.190". We wrapped copper wires in the shape of the box coils around the cylinders and applied an oscillating voltage to the wires to produce an oscillating magnetic field. We placed a small pickup coil inside the cylinder and measured the response of the coil to the oscillating magnetic field as a function of frequency.

Figure 5.1 shows the fraction of the signal that is transmitted through the cylinder wall as compared to the signal we receive in the absence of a stainless steel cylinder. If the shortest hold time for a plasma is around 100 ms, then perhaps we would want the quadrupole field to turn on in 1 ms. Figure 5.1 shows that there is near unity transmission at 1 kHz.

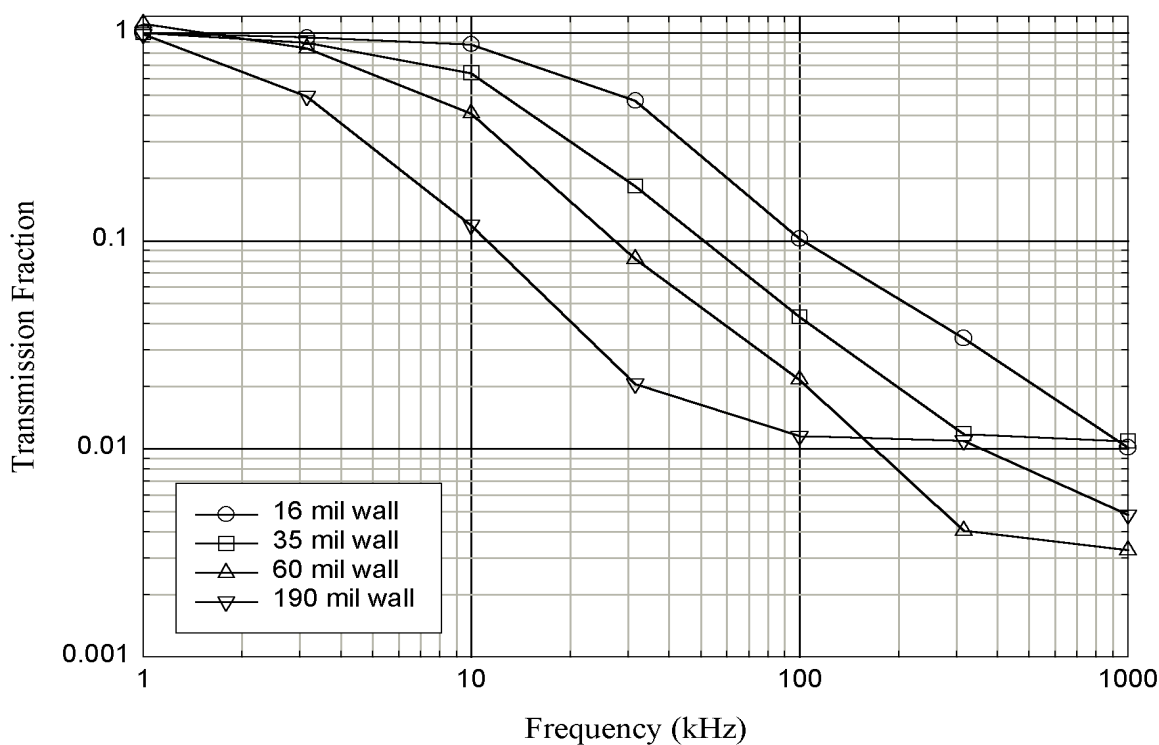


Figure 5.1: We create an oscillating magnetic field outside of stainless steel cylinders of several wall radii. The transmission fraction is defined as the ratio of the signal received on the pickup coil when placed inside a cylinder as compared to the signal received when no cylinder is present.

If we are concerned about the magnetic properties of stainless steel, we could con-

sider the alternative design in Figure 5.2. In this design, the trap walls could be constructed from copper rods machined to fit together so that the trap wall is circular and so that there are gaps between adjacent rods. The gaps would reduce τ . Reducing τ allows us to turn on

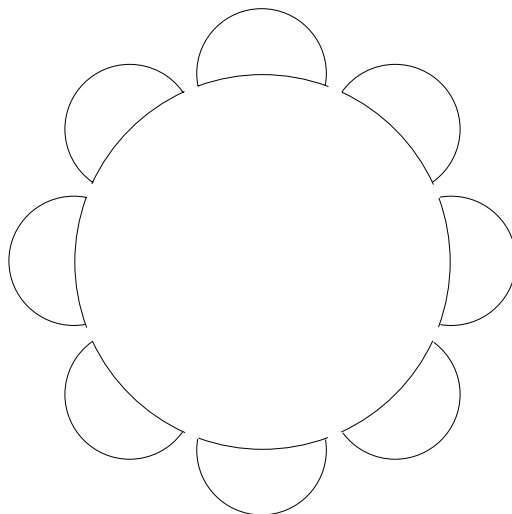


Figure 5.2: An alternate trap design might consist of walls that are made from copper rods machined to form a circular trap. The gaps between adjacent rods would reduce the magnetic field diffusion time.

the perturbation after we inject the plasma and turn it off before we dump the plasma. This would make the initial plasmas more similar to one another and perhaps help disentangle the properties of the plasma from the effects of the quadrupole field during imaging.

One could add extra coils for the application of higher order multipole fields. We could make the imaging electric field more uniform in order to reduce the image rotation and compression at low B_z . For example, adding conducting annular plates around the phosphor and the last gate would help to keep the electric field lines straight. To help explore the region $\omega_E t_b \gg 1$, we could make the confinement region longer. Or, we could increase t_b by allowing a gas into the vacuum chamber for the plasma to collisionally cool against.

There is clearly room for more refined measurements of the effects of a quadrupole field on transport in a Malmberg-Penning trap, and these measurements would benefit from a deeper theoretical understanding of the physics involved.

Appendix A

Imaging System

The most important modification of the machine was the installation of a new CCD camera system. The new system gives us faster data rates, better resolution and an improved signal to background ratio. This appendix describes the details of the camera system and instructions for its use.

A.1 First Camera System

The original camera was a Fairchild Weston Schlumberger model 3000F CCD camera connected to a PC via a Data Translation frame grabber card. The image acquisition times were slow and the camera had a resolution of 334×470 pixels. The optics were such that the phosphor covered a grid of 200×300 pixels; the pixels were not square. The largest problem, however, was signal to background ratio. As mentioned in Chapter 2, the filament glows white hot and steps were taken to reduce this light. Even with the aluminization of the phosphor and the use of the optical filter, the background light was approximately a factor of two brighter than light from the plasma on a per pixel basis. The maximum signal per pixel from a plasma was about 500 units, which is an underutilization of the dynamic range of the CCD array.

A.2 Second Camera System

The first fix for these problems was to use a Princeton Instruments liquid nitrogen cooled CCD camera with a mechanical shutter. The CCD array itself (TEK-1024) was more

sensitive. The resolution was improved as the phosphor now covered a grid of 400×400 pixels. Maximum pixels brightnesses from a plasma were improved to approximately 1500 units. The mechanical shutter was capable of opening and closing within 10 ms and could be driven pneumatically or electrically. When driven pneumatically, we included a small gas reservoir to maintain air pressure during the shutter operation. This produced shorter exposures. Using this system, the signal to background was still less than unity.

The liquid nitrogen dewar needed filling every 12 hours. This made long data runs difficult because runs would be interrupted by the need to fill the dewar. The mechanical shutter caused vibrations that would misalign the camera over time, requiring that more frequent background images be taken. Over time, the shutter leafs began to fail and would frequently jam. Perhaps most importantly, this camera was a shared resource in the lab, leading to schedule conflicts.

A.3 Current Camera System

Finally, we moved to an intensified CCD camera system, a Princeton Instruments ICCD-MAX. With the most current technology, we have the fastest data rates yet. The intensifier can be gated for exposure times down to the nanosecond range. As the light from a plasma is present for less than 3 ms (see Figure A.1), we do not need nanosecond shutter speeds, but we can tailor the exposure time to match the phosphor characteristics. Also, we can optimize the intensifier gain to take advantage of the full dynamic range of the CCD array. The per pixel brightness of the background is reduced to about 1000 units by shuttering, while the brightest pixels of a plasma image are about 10,000 units. The pinhole defects shown in Figure 2.3 are as bright as 5000 units. There are no moving parts in this camera so that there are fewer misalignment necessitated background image acquisitions. This camera uses thermoelectric cooling and not liquid Nitrogen to cool the CCD array, and so no user intervention is required during data acquisition. Software integration is smoother as well. Compared to earlier systems, it is easy to import camera data into analysis software.

There is one drawback that this camera system does not overcome, thermal fluctuations. After using the camera system during the day and at night, on cold days and on hot days, with the lab doors and windows opened and closed, it became apparent that the brightness of the camera images was proportional to the ambient temperature. This was true regardless of the temperature regulation of the CCD array itself to better than 0.01°C .

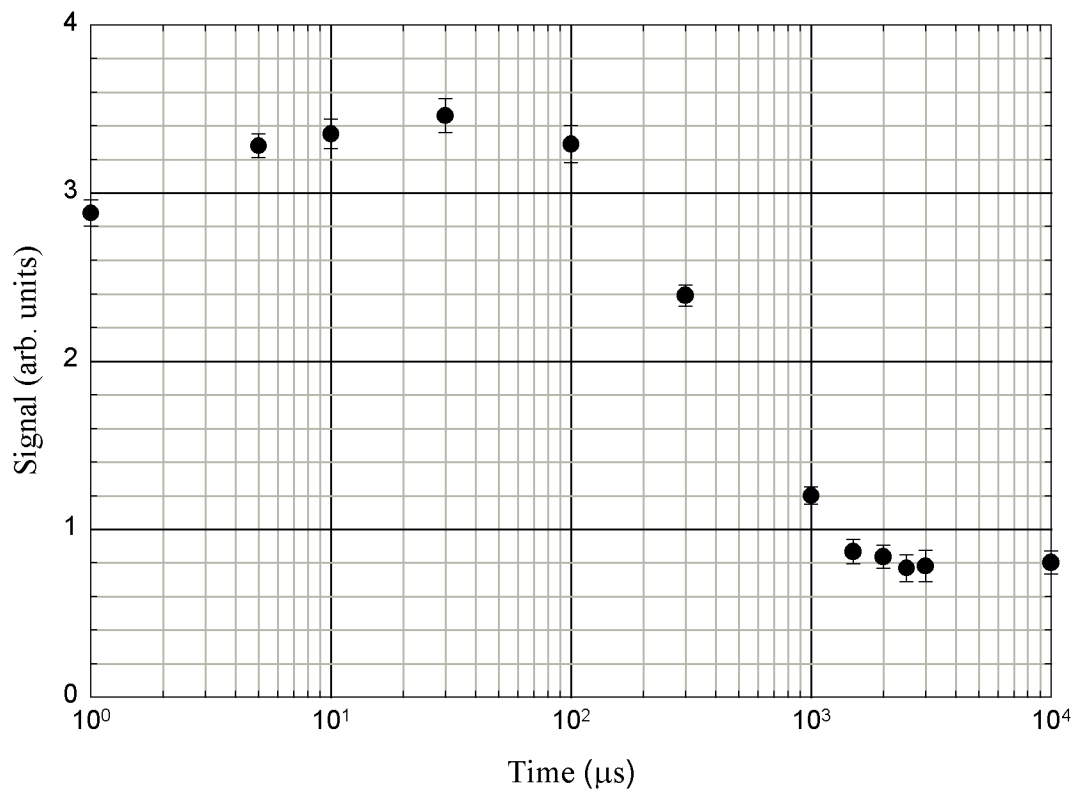


Figure A.1: The brightness of the phosphor as a function of time without background subtraction. The shutter is open for only $1 \mu\text{s}$. During the first $10 \mu\text{s}$, the signal increases as more electrons leave the trap and strike the phosphor. The data show that after approximately 1.5 ms , the phosphor is dark again, therefore camera shutter need only be open for these 1.5 ms . Note that the background light is at a level of 0.8 in these arbitrary units, smaller than the signal from the plasma.

Some other part of the camera is sensitive to the ambient temperature.

To correct for this, we constructed a temperature regulation system. We addressed the trivial problems first. Keeping the doors and windows to the lab closed helps to reduce rapid temperature changes during data runs. Further, we placed the camera inside a padded aluminum box to isolate it from the air in the room. The box has a fan on top to blow room temperature air onto the camera. There are several exhaust holes near the bottom of the box. We placed a temperature probe (AD 590) inside the box by the exhaust of the camera body. By trial and error, we determined that the camera exhaust served as the most accurate measure for the temperature sensitive elements of the system. Because we are restricting the air flowing to the camera against manufacturer recommendation, we connected a thermal switch to the AC power and attached it to the neck of the image intensifier. If the system becomes too hot, the power turns off and the system cools.

The temperature probe and fan work as parts of a feedback system controlled by an OMEGA CN77000 PID Process Control unit. We built the circuitry shown in Figure A.2 (PP-25) to interface both the temperature probe and the fan to the OMEGA unit.

R1 ($k\Omega$)	T_o ($^{\circ}C$)	R2 ($k\Omega$)	ΔT ($^{\circ}C$)
2.10	20	68.0	5
1.68	25	34.0	10
1.40	30	22.6	15
1.20	35	17.0	20
1.05	40	13.6	25

Table A.1: The values of R1 and R2 determine the temperature range that the OMEGA PID 10 V input range corresponds to.

The primary source of heat is the heat generated by the camera. The fan provides the cooling and the air temperature of the lab and the speed of the fan control the amount of cooling. The optimal temperature for operation is $36^{\circ}C$, and the system is regulated to within $\pm 0.03^{\circ}C$. Only on the hottest days of summer was the temperature control system unable to maintain this temperature. Temperatures much closer to $40^{\circ}C$ are not healthy for the camera.

A secondary issue with the camera system is the timing. We need to know when to trigger the camera so that we capture all of the light from the plasma. We also need to know how long the camera takes to read out the image to the PC so that we know when to prepare the next plasma. We find that sending the trigger pulse to the camera $1 \mu s$

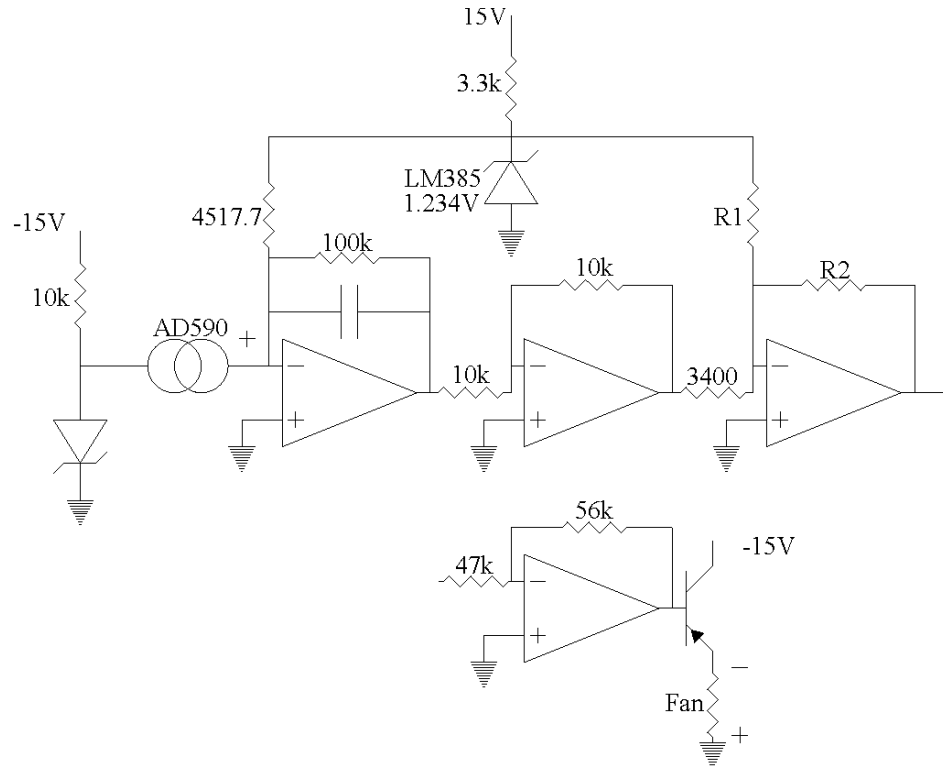


Figure A.2: PP-25 schematic. The top circuit takes the temperature reading from the AD590 (a current in μA equal to the absolute temperature in K) and converts it into a voltage in mV equal to the temperature in $^{\circ}\text{C}$ and then into a voltage between 0 and 10 V for use by the OMEGA PID controller. This 0-10 V signal corresponds to a temperature range between T_o and $T_o + \Delta T$, where R1 and R2 determine T_o and ΔT as shown in table A.1. The bottom circuit allows the OMEGA PID controller to drive the fan. The OMEGA PID controller outputs a voltage between 0 V and 10 V, but with little current. The fan requires a voltage between 4 V and 12 V to operate over its full range.

before we send the signal to the dump gate is sufficient to capture all of the light from the phosphor.

The overall repetition rate of our experiments is limited by the readout time of the camera controller unit. Measurements show that it requires at least 385 ms to read out an image. This is the lower bound on the cycle time. We observe that, for whatever reason, the controller takes more time to read out the occasional image. To prevent image from being taken while the CCD array is reading out and leading to a double exposure, we pass the trigger pulse to the camera through an AND gate with the $\overline{\text{SCAN}}$ TTL pulse from the camera. The $\overline{\text{SCAN}}$ indicates whether the camera is ready for the next image or is still reading out data. Unfortunately, this $\overline{\text{SCAN}}$ pulse is not either high or low, but rather high, or spiky. We remove the spikes with a low pass RC filter before we send the signal to the AND gate. Figure A.3 shows the timing diagram for triggering the camera.

The WinView software has numerous settings, most of which are automatically stored by the software. Table A.2 shows these settings. The reader may find details regarding these settings in *WinView User's Manual* and *ST-133 Controller Operation Manual*. The two settings that must be reset by the user each time the software is run are: Detector Temperature and LOGIC OUT Output.

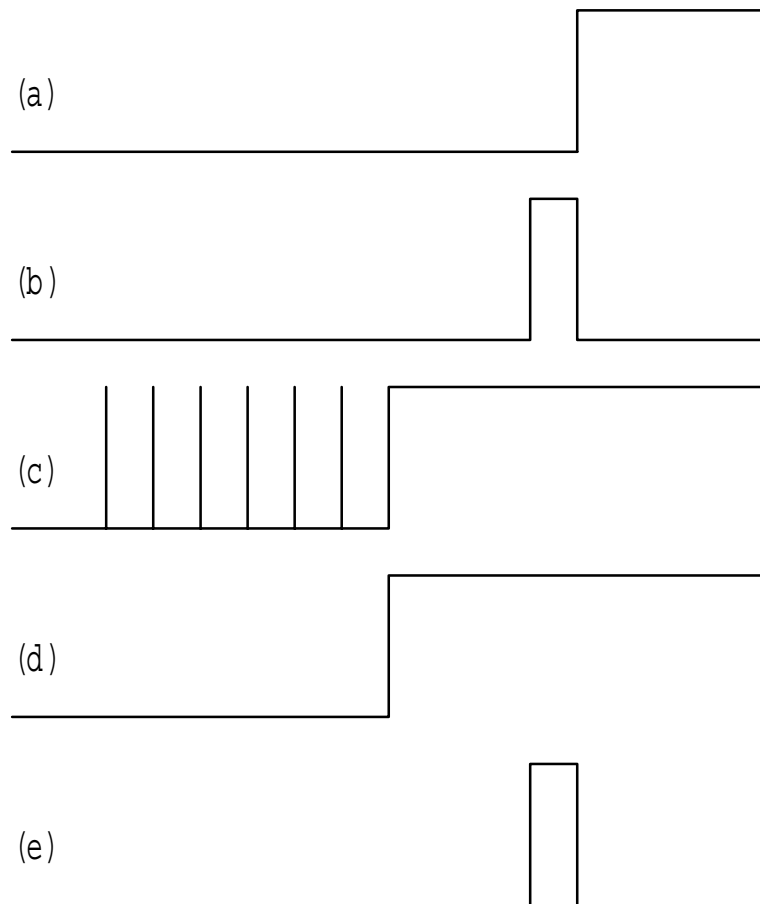


Figure A.3: (a) The dump pulse signals the release of the plasma. (b) The camera trigger pulse from the SN100 is $1 \mu\text{s}$ wide and must precede the dump pulse by $1 \mu\text{s}$. (c) The $\overline{\text{SCAN}}$ pulse goes high when the camera is ready to record an image. Before that time, there are extraneous spikes. The spikes are approximately $0.2 \mu\text{s}$ wide and 4 ms apart. (d) We remove the spikes with a low pass RC filter ($R = 20 \Omega$, $C = 50 \text{ nF}$). (e) The camera must not be triggered while it is reading out the CCD array and so we send the trigger pulse and the filtered $\overline{\text{SCAN}}$ pulse through an AND gate.

Software Setting	Value
Detector Temperature	-20
Controller Type	ST133
Camera Type	THM 512x512
Shutter Type	Electronic
LOGIC OUT Output	Not Scan
Interface Type	High Speed PCI
Number of Cleans	1
Strips per Clean	512
Minimum Block Size	2
Number of Blocks	5
Exposure Time	0
Accumulations	5
Gain	150
Intensifier	Gate Mode
ADC Type	Fast
Timing Mode	External Sync
Shutter Control	Normal
Safe Mode (async)	selected
Edge Trigger	+ edge

Table A.2: Software settings for WinView/32 2.4.2.4 are shown here. Details regarding these settings may be found in the WinView documentation. All settings but two are recorded by the software. Detector Temperature and LOGIC OUT Output must be reset by the user each time the software is run.

Appendix B

LabVIEW Programs

To aid in the acquisition and analysis of data, we used National Instruments' LabVIEW 6i software. This appendix is an attempt to document the programs we wrote for acquisition and analysis.

B.1 Hardware Control

LabVIEW comes with low level hardware routines that can control the AT-AO-6 DAQ card, the RS-232 port, and the USB GPIB bus. We wrote several programs that make use of these built-in routines to control hardware. Princeton instrument hardware and software controls the CCD camera system.

B.1.1 AT-AO-6

We use the AT-AO-6 DAQ board to interface the PC with the magnet power supplies, the filament bias control and the quadrupole field polarity switching relay.

- CONTROL MAG FIELDS.VI is a top level vi that controls the magnets' power supplies. This routine converts the requested magnetic field into the appropriate voltage to apply to the voltage programmed current mode power supplies. We calibrated the power supplies by measuring the output current as a function of programming voltage. We numerically simulated our magnet coils to obtain the calibration between coil current and magnetic field. To prevent ground path problems that had damaged the AT-AO-6, the analog signals from the AT-AO-6 pass through a series of op-amp

buffers (Job # PP-24).

- BOX COIL POLARITY.VI is a sub vi of CONTROL MAG FIELDS.VI that uses a digital output channel to energize a relay connected to the box shaped quadrupole field coils. We wired the relay as a DPDT switch that serves to control the polarity of the magnetic field.
- FILAMENT BIAS ON/OFF SWITCH.VI uses a digital output channel on the AT-AO-6 card to send a TTL signal to the Cathode Driver (Job # 98-38). This TTL signal selects either a filament bias of +10V or a front panel controlled negative voltage.

B.1.2 RS-232

We use the serial port to control the dedicated PC that operates the Rohatgi Electronics SN100 Sequencer.

- LOWLEVELCOMM.VI is called by all other vi's that wish to talk to the SN100. The command syntax is given in the SN100 users' manual.
- MONITOR COMM SN100.VI was originally designed to overcome problems with old versions of Microsoft Windows' DCOM software. With newer versions of DCOM, this vi may be unnecessary. However, in normal usage, this vi is set running and the beginning of each user session and is left running for the duration of the experiment.

B.1.3 USB GPIB

To free system resources that a PCI card would otherwise consume, we purchased a USB GPIB controller.

- AUTO SETUP ARB INJECT calculates the shape of the inject pulse based on the requested field, B_z , and uses LabVIEW's GPIB commands to address the Tektronix AFG 5101 Arbitrary/Function Generator directly.
- TEMPERATURE.LLB contains routines that acquire traces from the Tektronix TDS-420A oscilloscope. This library also contains routines that calculate kT from these traces.

B.1.4 Image Acquisition

The WinView software from Princeton Instruments is responsible for acquiring images from the ST-133 camera controller via the custom serial interface provided by the manufacturer. There are a number of ways to import the image data into LabVIEW for analysis. Unfortunately, none of these methods are as direct as we might like. The following methods are workarounds.

One method is to write a program that creates a WinView object and repeatedly acquires images when the camera is ready. LabVIEW is not capable of this and so we used Visual Basic. We set the instance of WinView to write these images to a storage directory with sequential filenames. LabVIEW routines then search the directory for current images and read these files. This method has two problems; hard drive access times are nonnegligible and this method is asynchronous.

VB ACTIVEX.EXE TO GET SPE DATA.VI opens an ActiveX automation reference to an ActiveX object that we wrote in Visual Basic. This object acquires an image from WinView and outputs the data to LabVIEW as an array of numbers. There is no time consuming hard disk access. This method is both faster and synchronous.

B.2 General Experiment Operation

There are many routines we use for general operation of the experiment. LOAD TYPICAL ROUTINES.VI opens the front panels of some of the most useful vi's for general machine operation.

- MONITOR COMM SN100.VI
- FILAMENT BIAS ON/OFF SWITCH.VI
- COMPLETE SETUP initializes B_z , \vec{B}_\perp , β , θ_o , the inject gate pulse, the hold time and the total cycle time.
- GET BACKGROUND DATA.VI biases the filament to +10V to stop plasma injection and takes pictures of the background light. Then, it searches the image and makes a map of the pinholes seen in Figure 2.3. The software uses this map to replace these pixels in the final image with a suitable average of nearest neighbors.

- GET PLASMA PICTURE.VI ensures that the filament is biased, obtains the raw image, subtracts the background, fixes the pinholes, and expands the image to compensate for the compression from the imaging electric fields.

B.3 Analysis

Some of these analysis programs are used as subroutines in programs like GET PLASMA PICTURE.VI, while some stand alone.

- ARRAY SMOOTHER.VI applies a mask to the image to smooth the image.
- THRESHOLD AND CLIP.VI sets all pixels beyond a given radius to zero and sets all pixels below a threshold value to zero.
- RADIAL EXPANSION.VI stretches the image according the formula, $r \rightarrow m(B_z)r$, where $m \approx [200/B_z(G)]^{0.28}$ for $B_z \leq 200$ G.
- CALCULATE BASIC PARAMETERS takes a camera image and finds the total image brightness, the brightest pixel, the mean values of x , y , x^2 , y^2 , $(x - \bar{x})^2$, and $(y - \bar{y})^2$, the RMS radius and the angular momentum.
- CALCULATE ELLIPTICITY.VI computes ϵ and θ_p according to the formulae in Chapter 3.
- RONSON'S POISSON SOLVER.VI takes the cartesian image data, converts it to polar coordinates, finds the potential $\phi(r, \theta)$ and finds the electric field, $-\vec{\nabla}_{\perp}\phi(r, \theta)$ under the assumption that the image corresponds to an axially invariant charge distribution. This program is an implementation of the algorithm used by Chu [41].
- HUGHES RZ POISSON SOLVER.VI is a LabVIEW implementation of the r - z Poisson solver in [34]. This routine is useful for finding an estimate of L . It finds L by calculating the turning points for an electron with v_{th} .
- RZPOISSON.VI is a multigrid relaxer we use to simulate the electric field produced by the high voltage on the phosphor.

B.4 Transport Experiment

These vi's break into two groups: automated acquisition/analysis routines and nonautomated analysis.

- QUADRUPOLE TRANSPORT EXPERIMENT.VI is a top level program we wrote to automatically accumulate and analyze data for the transport experiment. This program uses many of the routines described in the earlier sections of this appendix. The program applies a magnetic field perturbation, collects $n(r, t)$ data, computes dN/dt , ω , and dn/dr , and calculates fluxes and diffusion coefficients.
 - FIND PROPER HOLD TIME.VI finds the longest hold time to use by increasing the hold time until $n(R)$ decays to some arbitrary value. We find that choosing $n = 2.5 \times 10^6 \text{ cm}^{-3}$ works well for all B_z to allow us to both reliably calculate dN/dt and have a wide range of ω .
 - TOTAL VS BX AND BY-2D.VI and TOTAL VS BETA AND THETA-2D.VI next apply various dipole and quadrupole perturbations at the longest hold time in order to find the optimal tuning. Both routines use the total charge technique described in Section 4.2.2. We use these optimal values as the centers about which we apply perturbations. An important subroutine is HARDY 2D SPLINE.VI, which uses a Hardy Multiquartics spline [42] to interpolate the data.
 - TIME HISTORY.VI applies a magnetic field perturbation and measures $n(r, t)$ for 36 times between $4\mu\text{s}$ and the longest hold time.
 - NEW ANALYZE DATA.VI takes the data acquired by from TIME HISTORY.VI, passes it to RONSON'S POISSON SOLVER.VI, and then calculates $N(R)$ and dn/dr . To compute dn/dr , we discretize $n(r)$ into 120 bins and fit a parabola to a ± 7 bin wide region centered on R .
 - WRITE B BX BY DT DNDR N D OMEGA N TI POINTSUSED.VI takes the results of NEW ANALYZE DATA.VI and calculates dN/dt , ω and D . To compute dN/dt , we fit a parabola to $N(t)$.

The final output of QUADRUPOLE TRANSPORT EXPERIMENT.VIS is a record of B_z , \vec{B}_\perp , β_1 , β_2 , R , n , ω , dn/dr , dN/dt , Γ and D for all 36 times and for all 120 radii.

- PROCESS DATA.VI finds D or Γ as function of either (B_x, B_y) or (β_1, β_2) at constant ω . We again use the HARDY 2D SPLINE.VI routine to interpolate the data. Figure 4.10 is an example of $D(\beta_1, \beta_2)$. The program finds the extrema of these functions and finds the average value of the function over 100 points on a circle centered on the extrema.

Bibliography

- [1] M. H. Holzscheiter et al. Antihydrogen production and precision experiments. *Hyperfine Interactions*, 109:1997, 1997.
- [2] G. Gabrielse and L. Haarsma S.L. Rolston. Antihydrogen production using trapped plasmas. *Phys. Lett. A*, 129:38, 1988.
- [3] R. G. Greaves and C. M. Surko. Antimatter plasmas and antihydrogen. *Phys. Plasmas*, 4:1528, 1997.
- [4] G. Gabrielse et al. The ingredients of cold antihydrogen: Simultaneous confinement of antiprotons and positrons at 4K. *Phys. Lett. B*, 455:311, 1999.
- [5] G. Baur et al. Production of antihydrogen. *Phys. Lett. B*, 368:251, 1996.
- [6] J. Schwinger. The theory of quantized fields 1. *Phys. Rev.*, 82:914, 1951.
- [7] G. Luders and B. Zumino. Some consequences of tcp-invariance. *Phys. Rev.*, 106:385, 1957.
- [8] S. Weinberg. *Principles and Applications of The General Theory of Relativity*. John Wiley & Sons, New York, 1972.
- [9] T. M. O'Neil. A confinement theorem for nonneutral plasmas. *Phys. Fluids*, 23:2216, 1980.
- [10] J. H. Malmberg and C. F. Driscoll. Long-time containment of a pure electron plasma. *Phys. Rev. Lett.*, 44:654, 1980.
- [11] D. L. Eggleston. Experimental test of the resonant particle theory of asymmetry-induced transport. In J. J. Bollinger, R. L. Spencer, and R. C. Davidson, editors, *Non-*

- Neutral Plasma Physics III*, volume AIP 498, page 241, New York, 1999. American Institute of Physics.
- [12] J. Kriesel. *Experiments on Viscous and Asymmetry-Induced Transport in Magnetized, Pure Electron Plasmas*. PhD thesis, University of California, San Diego, 1999.
- [13] J.M. Kriesel and C.F. Driscoll. Two regimes of asymmetry-induced transport in non-neutral plasmas. *Phys. Rev. Lett.*, 85:2510, 2000.
- [14] R. Keinigs. The effect of magnetic field errors on low frequency waves in a pure electron plasma. *Phys. Fluids*, 24:1447, 1981.
- [15] C. F. Driscoll and J. H. Malmberg. Length-dependent containment of a pure electron plasma. *Phys. Rev. Lett.*, 50:167, 1983.
- [16] R. Keinigs. Field-error induced transport in a pure electron column. *Phys. Fluids*, 27:206, 1984.
- [17] J. H. Malmberg, C. F. Driscoll, B. Beck, D. L. Eggleston, J. Fajans, K. Fine, X. P. Huang, and A. W. Hyatt. Experiments with pure electron plasmas. In C.W. Roberson and C.F. Driscoll, editors, *Nonneutral Plasma Physics*, volume AIP 175, page 28, New York, 1988. American Institute of Physics.
- [18] D. L. Eggleston and T. M. O'Neil. Theory of asymmetry-induced transport in a non-neutral plasma. *Phys. Plasmas*, 6:2699, 1999.
- [19] B.P. Cluggish, J.R. Danielson, and C.F. Driscoll. Resonant particle heating of an electron plasma by oscillating sheaths. *Phys. Rev. Lett.*, 81:353, 1998.
- [20] D.D. Ryutov and G.V. Stupakov. Neoclassical transport in ambipolar confinement systems. *Sov. J. Plasma Phys.*, 4:278, 1978.
- [21] D.D. Ryutov and G.V. Stupakov. Diffusion of resonance particles in ambipolar plasma traps. *Sov. Phys. Dokl.*, 23:412, 1978.
- [22] R.H. Cohen. Analytic approximation to resonant plateau transport coefficients for tandem mirrors. *Nuclear Fusion*, 19:1579, 1979.
- [23] R.H. Cohen, W.M. Nevins, and G.V. Stupakov. Collisional limits of resonant and neoclassical transport in tandem mirrors. *Nuclear Fusion*, 23:611, 1982.

- [24] B.V. Chirikov. Homogeneous model for resonant particle diffusion in an open magnetic confinement system. *Sov. J. Plasma Phys.*, 5:492, 1979.
- [25] E. Gilson, A. Reimann, and J. Fajans. Double well neutral plasma traps. *Bull. Am. Phys. Soc.*, 42:1959, 1997.
- [26] C. A. Ordonez. Time-dependent nested-well plasma trap. *IEEE Trans. Plasma Sci.*, 24:1378, 1996.
- [27] D. S. Hall and G. Gabrielse. Electron cooling of protons in a nesting penning trap. *Phys. Rev. Lett.*, 77:1962, 1996.
- [28] R. C. Davidson. *Physics of Nonneutral Plasmas*. Addison-Wesley, Redwood City, 1990.
- [29] J. A. Notte. *The Effect of Asymmetries on Nonneutral Plasmas*. PhD thesis, University of California, Berkeley, 1993.
- [30] W. D. White, J. H. Malmberg, and C. F. Driscoll. Resistive wall destabilization of diocotron waves. *Phys. Rev. Lett.*, 49:1822, 1982.
- [31] K. S. Fine. *Experiments with the $l=1$ Diocotron Mode*. PhD thesis, University of California, San Diego, 1988.
- [32] J. Fajans, E. Gilson, and L. Friedland. Autoresonant (nonstationary) excitation of the diocotron mode in non-neutral plasmas. *Phys. Rev. Lett.*, 82:4444, 1999.
- [33] K. S. Fine and C. F. Driscoll. The finite length diocotron mode. *Phys. Plasmas*, 5:601, 1998.
- [34] M. H. Hughes. Solution of poisson's equation in cylindrical coordinates. *Comput. Phys. Commun.*, 2:157, 1971.
- [35] A. J. Peurrung and J. Fajans. Non-neutral plasma shapes and edge profiles. *Phys. Fluids B*, 2:693, 1990.
- [36] D. L. Eggleston, C. F. Driscoll, B. R. Beck, A. W. Hyatt, and T. H. Malmberg. Parallel energy analyzer for pure electron plasma devices. *Phys. Fluids B*, 4:3432, 1992.
- [37] A. J. Peurrung. *Imaging of Instabilities in a Pure Electron Plasma*. PhD thesis, University of California, Berkeley, 1992.

- [38] C. Hansen. *A re-evaluation of plasma shielding*. PhD thesis, University of California, Berkeley, 1996.
- [39] A. B. Reimann. *Shielding in collisionless plasmas*. PhD thesis, University of California, Berkeley, 1998.
- [40] D. Durkin. Private communications.
- [41] R. Chu. *Theoretical Studies of Pure Electron Plasmas in Asymmetric Traps*. PhD thesis, Massachusetts Institute of Technology, 1993.
- [42] H. Spath. *Two Dimensional Spline Interpolation Algorithms*. A. K. Peters, Wellesley, MA, 1995.